Forschungszentrum Karlsruhe
in der Helmholtz-Gemeinschaft

Wissenschaftliche Berichte
FZKA 6889

Finite Volume-based Volume-of-Fluid Method for the Simulation of Two-Phase Flows in Small Rectangular Channels

B. E. Ghidersa

Institut für Reaktorsicherheit
Programm Mikrosystemtechnik

Mai 2004

Forschungszentrum Karlsruhe

in der Helmholtz-Gemeinschaft

Wissenschaftliche Berichte

FZKA 6889

Finite Volume-based Volume-of-Fluid Method for the Simulation of Two-Phase Flows in Small Rectangular Channels*

Brăduț Eugen Ghidersa

Institut für Reaktorsicherheit

Programm Mikrosystemtechnik

*Von der Fakultät für Maschinenbau

der Universität Karlsruhe (TH)

genehmigte Dissertation

Forschungszentrum Karlsruhe GmbH, Karlsruhe

2004

Impressum der Print-Ausgabe:

Als Manuskript gedruckt

Forschungszentrum Karlsruhe GmbH
Postfach 3640, 76021 Karlsruhe

Mitglied der Hermann von Helmholtz-Gemeinschaft
Deutscher Forschungszentren (HGF)

ISSN 0947-8620

urn:nbn:de:0005-068894

Eine Finite-Volumen Volume-of-Fluid Methode zur Simulation von Zweiphasenströmungen in kleinen rechteckigen Kanälen

ZUSAMMENFASSUNG

Das Thema der vorliegenden Arbeit ist die direkte numerische Simulation der gas-flüssig Zweiphasenströmung mit Wärmeübertragung in einem rechteckigen Kanal mit hydraulischem Durchmesser im Bereich von 1 mm. Es wird eine neue, auf Volumenmittelung basierende Formulierung der Enthalpiegleichung entwickelt. Diese wird im Rechenprogramm TURBIT-VOF eingeführt, wobei vorausgesetzt wird, dass beide Flüssigkeiten inkompressibel sind. Die numerische Approximation dieser Gleichung verwendet eine genaue Rekonstruktion der konvektiven und konduktiven Wärmeflüsse und verringert so Oszillationen, die auf Diskontinuitäten an der Phasengrenzfläche zurückzuführen sind.

Es wird ein neues Konzept für die Modellierung der konvektiven Wärmeübertragung einer räumlich periodischen Zweiphasenströmungen in einem Kanal vorgeschlagen, dessen Länge sehr viel größer als der hydraulische Durchmesser ist. Das als periodisch voll entwickelte Strömung und Wärmeübertragung bezeichnete Konzept nutzt aus, dass bereits in einer Entfernung von nur wenigen hydraulischen Durchmessern vom Einlass die Strömung frei von Einlass-Effekten ist. Für diese Region kann wegen der räumlichen Periodizität der sich axial wiederholenden Strömungsverhältnisse die Analyse der Geschwindigkeits- und Temperaturverteilung auf ein einzelnes ”Einheits-Modul” beschränkt werden. Als typisches Beispiel für eine räumlich periodische gas-flüssig Zweiphasenströmung wird in dieser Arbeit die Schwallströmung in einem kleinen Kanal herangezogen. Es wird numerisch die Strömung einer regelmäßigen Folge von gleichmäßig entlang eines Kanal mit quadratischem Querschnitt verteilten großen Luftblasen untersucht. Simulationen werden für zwei unterschiedliche Werte der Kapillar-Kennzahl durchgeführt. Die Blasenform, die Geschwindigkeitsverteilung innerhalb der Blase und im flüssigen Schwall werden analysiert. Der Durchmesser der Blase sowie deren absolute und relative Geschwindigkeit werden mit

experimentellen Daten aus der Literatur verglichen und zeigen eine gute Übereinstimmung. Des weiteren werden der konvektive und konduktive Wärmetransport der Zweiphasenströmung für den Fall einer vorgegebenen konstanten, gleichförmigen Wärmestromdichte an der Kanalwand numerisch untersucht. Dabei werden insbesondere die durch das Vorhandensein der Blase hervorgerufenen Änderungen im Temperaturfeld analysiert.

ABSTRACT

The topic of the present thesis is the direct numerical simulation of gas-liquid two-phase flow in rectangular channels with hydraulic diameter of the order of 1 mm with heat transfer. A new volume-averaged equation for enthalpy is derived and implemented in the finite volume code `TURBIT-VoF` for the case when both fluids are considered as incompressible. The numerical approximation of this equation reduces the oscillations associated with the discontinuities at the interface using an accurate reconstruction of the convective and conductive heat fluxes.

To model convective heat transfer for a spatially periodic two-phase flow in a channel with large length-to-hydraulic diameter ratio, a new concept, called *periodic fully developed flow and heat transfer*, is proposed. After a few hydraulic diameter away from the channel inlet the flow characteristics are free from entrance effects. For this region, the identification of the periodicity characteristics of the flow enables to restrict the analysis of the flow field and temperature distribution to a single isolated module. As typical example of periodic gas-liquid two-phase flow, the slug flow in small channels is considered. The flow of a train of large bubbles uniformly distributed along a channel with square cross-section is simulated. The bubble shape, the flow structure inside the bubble and in the liquid slug are analyzed. The bubble diameter, bubble velocity and relative bubble velocity for two different Capillary numbers are computed and compared with the experimental data from the literature showing good agreement. The convection and conduction of heat inside the channel due to a uniform, both axially and perimetrically, heat flux is also considered. The modification of the temperature field due to the presence of the bubble is analyzed.

CONTENTS

LIST OF TABLES

LIST OF FIGURES

NOTATION

Lower-case Roman

$\vec{\mathsf{b}}$	*body force per unit mass*
f	*liquid fraction volume*
g, $\vec{\mathsf{g}}$	*gravity*
h	*enthalpy per unit mass*
h	*convective conductance*
$\dot{m}_\varphi$	*local loss of fluid φ per unit area of S_i per unit time*
ℓ	*characteristic length*
$\vec{\mathsf{m}}_i^\sigma$	*traction associated with surface tension*
$\vec{\mathsf{n}}$	*unit normal to the interface pointing from fluid 1 to fluid 2*
$\vec{\mathsf{n}}_\varphi$	*unit normal to the interface pointing outside V_φ*
p	*pressure*
$\vec{\mathsf{q}}$	*heat flux*
r	*body source of internal energy per unit mass*
s	*the entropy*
t	*time*
u	*internal energy per unit mass, velocity component in x-direction*
u_i	*surface internal energy density*
$\vec{\mathsf{v}}$	*fluid velocity*
$\vec{\mathsf{v}}_i$	*interface velocity*
v	*velocity component in y-direction*
w	*velocity component in z-direction*
$\vec{\mathsf{x}}$	*coordinates vector*

Upper-case Roman

C_p	*specific heat*
$\mathbf{I}$	*unity tensor*
J	*superficial velocity*
$\mathbf{T}$	*stress tensor*
S_i	*part of the interface contained in V*
T	*temperature*
T_i	*interface temperature*
V	*control volume*
V_φ	*the volume inside V occupied by the fluid φ*
X_φ	*characteristic function for phase φ*

Lower-case Greek

α	*volume fraction*
β	*pressure drop, coefficient of volumetric expansion in Boussinesq approximation*
γ	*phase convective heat transfer coefficient*
κ	*mean curvature of the interface*
λ	*heat conductivity*
ρ	*density*
σ	*surface tension*
θ	*linear temperature coefficient (see Eq. 4.26b)*
$\boldsymbol{\tau}$	*viscous stress tensor*

Upper-case Greek

Δ_i	*entropy production at the interface*
Θ	*reduced temperature*
Υ	*convective heat transfer coefficient*

Mathematical Operators

$\overline{\psi}^{\varphi}$	*Favré average of the variable ψ over the volume V_φ*
$\langle\psi\rangle_{\varphi}$	*average of the variable ψ over the volume V*
$\delta_{\varphi}\psi$	*deviation of the local value of ψ from $\overline{\psi}^{\varphi}$*

Dimensionless numbers

$\mathtt{Re}$	*Reynolds number:* $\dfrac{\rho^*\mathtt{v}^*\ell^*}{\mu^*}$
$\mathtt{Eo}$	*Eötvös number:* $(\rho_1-\rho_2)\dfrac{g(\ell^*)^2}{\sigma^*}$
$\mathtt{Fr}$	*Froude number:* $\dfrac{\ell^* g}{(\mathtt{v}^*)^2}$
$\mathtt{Gr}$	*Grashof number:* $\mathtt{Ra}/\mathtt{Pr}$
$\mathtt{Pr}$	*Prandtl number:* $\dfrac{C_p^*\mu^*}{\lambda^*}$
$\mathtt{Pe}$	*Peclet number:* $\dfrac{\rho^* C_p^*\mathtt{v}^*\ell^*}{\lambda^*}$
$\mathtt{Ra}$	*Rayleigh number:* $g\beta^*\Delta T^*(\ell^*)^3\dfrac{(\rho^*)^2 C_p^*}{\mu^*\lambda^*}$
$\mathtt{We}$	*Weber number:* $\dfrac{\rho^*(\mathtt{v}^*)^2\ell}{\sigma^*}$

Subscripts

φ	*associated to phase ϕ*
φi	*value at the interface associated to phase φ*
m	*mean (mixture) value in the corresponding control volume*

Superscripts

$*$	*reference quantity*
0	*reference quantity related to reference temperature in Boussinesq approximation*

1. INTRODUCTION

Microfabrication techniques developed within last decades made possible the building of miniaturized devices with high mixing and heat transfer characteristics [7, 41]. Consisting of large number of nominally identical flow channels with hydraulic diameter of order of 1 mm or smaller, these devices are increasingly used in different fields of chemistry due to their capabilities that are exceeding those of conventional macroscopic systems [21]. Compact heat exchangers with enhanced heat transfer rates and micro-reactors with increased specific interfacial areas, compared with classical devices, are only two examples of industrial applications, where such kind of systems are intended to replace the existing technologies in order to increase the efficiency. The micro-bubble column reactor [7] for example can provide for extraordinary high interfacial area per unit volume [15] and thus allows for high mass transfer rates. Another example is the segmented flow tubular reactor [22] developed within the bubble tube project that utilizes the intense mixing of the two-phase flow for production of high-quality powder. The ability to integrate sensors for flow, temperature, and chemical composition with microfluidic reaction and control components allow reactions to be performed under more aggressive conditions and with higher yields than can be achieved with conventional reactors. Also, for future fusion power plants, small (1 mm wide) rectangular channels are intended to be used for the cooling of the fusion blankets. These channels form a network with high surface-to-volume ratio capable to remove efficiently the heat obtained by converting the neutrons energy.

The advantages from increased heat and mass transfer in small dimensions have been demonstrated with model gas, liquid, and multiphase systems [7, 21]. While for single phase flows[1]the term "small" is defined based on the diffusive mixing length, which ranges from about 20 μm up to a few hundreds microns, for gas-liquid flows it is customary to call *micro-channels* those channels having the hydraulic diameter (D_h) smaller or equal to the Laplace length $\lambda = \sqrt{\sigma/(g\Delta\rho)}$, to distinguish them from *large channels*. This

[1] Inhere, *single phase flows* refers to fluid flows for which the components are miscible fluids (there is

characteristic length gives the order of magnitude of the wavelength of the interfacial wave in Taylor instability. The latter type of instability is known to govern important hydrodynamic processes such as bubble or droplet breakup in pool boiling or large channel flows. When $D_h \leq \lambda$ the flow confinement makes some of the Taylor instability-driven processes to be entirely irrelevant. Thus, the surface tension effects become more important than buoyancy, which leads to insensitivity of two-phase hydrodynamics to channel orientation, and in non-stratified two-phase flow patterns [11, 52]. For many gas-liquid flows of practical interest (e.g. air-water flows) the Laplace length is of the order of 1 mm. Since buoyancy is no longer dominating the dynamics of the two-phase system, the experimental data obtained for micro-channels show poor agrement with the relevant flow regime transition models which were deduced for large channels [11, 52]. This is the motivation for an increasing number of analytical [29, 30, 56] and experimental studies devoted to the two-phase flow in single narrow tubes [43, 51, 52] and in channels with triangular [51, 52] or rectangular [48, 49] cross-section.

When the hydraulic diameter of the channel is very small, measurement techniques that are well established in macro-channels encounter serious difficulties. In micro-channels only non-intrusive measurement techniques can be used and the results are usually limited to visualization of the bubble shape and measurement of integral data such as the flow rates of both phases and the axial pressure drop. This is along the main objectives of many experimental studies, namely to develop engineering correlations for pressure-drop [51] and heat transfer. However, there is currently no measurement method available that can provide full information on the three-dimensional local velocity field of both phases in the entire micro-channel.

A numerical treatment of this kind of problems may allow a better knowledge of local phenomena since the complete 3D velocity or temperature field is available (in the limit of grid resolution). In the literature there are several numerical approaches concerning heat and mass transfer problems in two-phase systems. The solidification of melting has been simulated by Knoll, Kothe and Lally [28]. Impact and solidification of thin droplets on a flat stainless steel plate has been studied by Psandideh–Fard *et al.* [34]. Wohak [57] and Wohak and Beer [58] simulated the direct–contact evaporation of a drop rising in a hot liquid using algorithms with poor interface reconstruction. The motion of single and multiple gas

no interface), while *two-phase flows* denotes the flow of two immiscible fluids which are separated by a distinct interface.

bubbles in an otherwise stationary liquid contained in a closed right vertical cylinder is investigated by Chen *et al.* [2] using a Volume-of-Fluid (VOF) method which incorporates the surface tension stresses. The fluids are incompressible and immiscible. The effects of mass and heat transfer are taken in account when evaporation is considered. Recently, Davidson and Rudman [4] developed a new VOF-based method for calculating heat transfer or mass transfer of species within and between fluids with deforming interfaces. All these numerical methods have been designed for large systems where the flow is buoyancy-driven. For two–phase flows in small channels there are no specific numerical methods up to now, most of the data being obtained from experimental work.

The objective of this study is to define a method that enables the direct numerical simulation (DNS) of 3D gas-liquid flows in rectangular small channels when heat or mass transfer are considered. In our approach, it is assumed that the heat/mass transfer across the interface is only due to conduction or diffusion, and no phase change occurs. This is an oversimplification of the complex phenomena characterizing the heat transfer in a compact heat exchanger where bubbles are usually generated due to vaporization of the liquid. This process, in small channels, is strongly influenced by the confinement of the flow and it is not well understood up to now [26], therefore, we concentrate our attention only on the modifications of the heat transfer characteristics due to the presence of bubbles in the liquid flow. This type of problem is also relevant for chemical processing where the mixing of different species determines the efficiency of the chemical reactor. This includes applications like micro bubble column [7, 15] and the monolith froth reactor [27]. Since in this cases the mass transfer is the relevant process, one can use the formal analogy between heat and mass transfer to simulate this. This analogy is valid under the conditions of no dissipation, low mass/heat flux and constant fluids properties [3]. Here, only microchannels with diameters of the order of 1 mm and with long length-to-hydraulic diameter ratios are considered. Throughout this dissertation it is referred to this category of microchannels as *small channels* to differentiate them from those channels with diameters of order of microns. Since the characteristic dimension is much larger than the molecular mean free path, for small channels, the equations of the continuum model can be used.

For simulating heat transfer, the implementation of an energy equation into an existing code (`TURBIT-VoF`) is considered. This code was developed by Sabisch [38] for isothermal flows with incompressible phases. Single bubble simulations were performed for a wide variety of regimes from spherical to ellipsoidal up to wobbling bubbles. Also, bubble swarm

flow were simulated using five ellipsoidal bubbles. All these simulations were performed for flow parameters corresponding to large channels, i.e. buoyancy was the main force accelerating the bubbles. The code is using a VOF method for tracking the interface. The main advantage of this method compared with other methods (level set, front tracking) is mass conservation.

This dissertation is structured as follows: in the next chapter the governing equations for mass, momentum and energy are deduced. The formulation is as general as possible. The simplified equations for incompressible fluids will be discussed. In chapter 3 the numerical method for the energy equation will be described. In chapter 4 a new concept of *periodic fully developed two-phase flow* will be introduced to describe the flow and heat transfer of a steady periodic two-phase flow in a channel with large length-to-hydraulic diameter ratio. The application of this concept for slug flow in a square channel is presented. Both adiabatic and convective heat transfer flows are simulated. Chapter 5 summarizes and concludes this work by highlighting possible directions for future research.

2. GOVERNING EQUATIONS FOR A MULTI-PHASE SYSTEM

In the literature, several models are currently used to describe the thermodynamics of a multi-phase system. Kataoka [24] has used characteristic functions of each phase in order to define the physical variables of two–phase flow as field quantities. In addition, the source terms at the interface are defined in terms of local instant interfacial area concentration. Based on these field quantities, the local instant field equations of mass, momentum and total energy conservation of two–phase flow has been derived. This local instant formulation form the basis for different formulations using various types of averaging. Unverdi and Tryggvason [54, 55] have used this kind of formulation in order to describe the fluids dynamics for two–phase flows in conjunction with an interface tracking method. This single field representation is equivalent to the local instant formulation of Ishii [20] and Delhaye [5]. The latter deduced the local instant equations for each fluid and the local instant jump conditions at the interface starting from the balance laws for mass momentum and energy. Sabisch [38] and Wörner *et al.* [60] derived a new volume-averaged formulation for the mass and momentum equations. These equations, called the VA-VOF equations, are suitable for numerical simulations of dynamic interface evolutions with the Volume-of-Fluid (VOF) method, where the boundary layer at the interface is not fully resolved by the grid.

In this chapter, the same procedure as in Sabisch [38] and Wörner *et al.* [60] it is used to derive the volume-averaged energy equation. First, a volume-averaged set of equations for each fluid φ is deduced. Then, these equations and the local instant jump conditions are used to write a single set of equations for the volume averaged values of the variables. For an easy reference the mass and momentum equations are also presented.

2.1 Volume-averaged equations

Let us consider two Newtonian and homogenous fluids, each fluid residing in a distinct domain Ω_φ, $\varphi = 1, 2$ such that the control volume $\Omega = \Omega_1(t) \cup \Omega_2(t)$ is fix and has a

rigid boundary ($\partial\Omega$). We assume that the size of Ω is large enough so that the interface separating the two fluids can be considered as thin and massless.

2.1.1 Phase volume averaged equations

In the bulk region of each component, the local mass, momentum and energy governing equations are:

continuity equation

$$\frac{\partial \rho_\varphi}{\partial t} + \nabla \cdot (\rho_\varphi \vec{\mathsf{v}}_\varphi) = 0 \tag{2.1a}$$

momentum equation

$$\frac{\partial \rho_\varphi \vec{\mathsf{v}}_\varphi}{\partial t} + \nabla \cdot (\rho_\varphi \vec{\mathsf{v}}_\varphi \vec{\mathsf{v}}_\varphi) = -\nabla p_\varphi + \rho_\varphi \vec{\mathsf{b}}_\varphi + \nabla \cdot \boldsymbol{\tau}_\varphi \tag{2.1b}$$

energy equation

$$\frac{\partial \rho_\varphi h_\varphi}{\partial t} + \nabla \cdot \rho_\varphi h_\varphi \vec{\mathsf{v}}_\varphi = -\nabla \cdot \vec{\mathsf{q}}_\varphi + \left(\frac{\partial p_\varphi}{\partial t} + \vec{\mathsf{v}}_\varphi \cdot \nabla p_\varphi \right) + \boldsymbol{\tau}_\varphi : \nabla \vec{\mathsf{v}}_\varphi + \rho r_\varphi. \tag{2.1c}$$

For the energy equation the enthalpy formulation is used because the convection of enthalpy, and not internal energy, is balanced by the heat conduction and viscous dissipation [33, 9].

Since the physical quantities are not defined over the entire control volume, in order to write the volume-averaged equations corresponding to each phase, one has to define a set of field quantities. This can be done by defining a characteristic function for each phase φ:

$$X_\varphi(\vec{\mathsf{x}}, t) = \begin{cases} 1\ , & \vec{\mathsf{x}} \in \Omega_\varphi(t), \\ 0\ , & \text{otherwise.} \end{cases} \tag{2.2}$$

One then multiplies the physical quantities (generically noted as Ψ) with the characteristic function of each phase. The new set of variables $X_\varphi \Psi$ can be regarded as field quantities [24]. The phase volume averaging operator for a general scalar or vector quantity, Ψ, over

the domain Ω is defined as

$$\langle \Psi \rangle_\varphi = \frac{1}{V} \int_\Omega \Psi X_\varphi(\vec{\mathsf{x}}, t)\, dV \tag{2.3}$$

where, V is the volume of Ω. Since Ω is not deformable V is constant in time. Applying this averaging operator to the equations for mass, momentum and energy (enthalpy), and using the Gauss and Leibnitz rules [6], one has:

$$\frac{\partial}{\partial t}\langle \rho \rangle_\varphi + \nabla \cdot \langle \rho \vec{\mathsf{v}} \rangle_\varphi = -\frac{1}{V} \int_{S_i(\vec{\mathsf{x}},t)} \dot{m}_\varphi\, dS \tag{2.4a}$$

for the mass conservation, where, $S_i(\vec{\mathsf{x}}, t)$ is the interface in Ω, $\dot{m}_\varphi = \vec{\mathsf{n}}_\varphi \cdot (\vec{\mathsf{v}}_{\varphi i} - \vec{\mathsf{v}}_i)\rho_{\varphi i}$ is the local loss of fluid φ per unit area of S_i and per unit time, and $\vec{\mathsf{v}}_i$ and $\vec{\mathsf{v}}_{\varphi i}$ are the velocity of the interface and the velocity of the fluid φ at the interface, respectively; the unit normal vector ($\vec{\mathsf{n}}_\varphi$) at the interface S_i is taken to point outside the volume Ω_φ. The volume averaged momentum equation for the phase φ is

$$\frac{\partial}{\partial t}\langle \rho \vec{\mathsf{v}} \rangle_\varphi + \nabla \cdot \langle \rho \vec{\mathsf{v}}\vec{\mathsf{v}} \rangle_\varphi = -\nabla \langle p \rangle_\varphi + \langle \rho \vec{\mathsf{b}} \rangle_\varphi + \nabla \cdot \langle \boldsymbol{\tau} \rangle_\varphi - \frac{1}{V} \int_{S_i(\vec{\mathsf{x}},t)} \left[\dot{m}_\varphi \vec{\mathsf{v}}_{\varphi i} - \vec{\mathsf{n}}_\varphi \cdot \mathbf{T}_{\varphi i} \right] dS \tag{2.4b}$$

where $\mathbf{T}_{\varphi i} = -p_{\varphi i}\mathbf{I} + \boldsymbol{\tau}_{\varphi i}$ is the stress tensor of the phase φ at the interface, and

$$\frac{\partial}{\partial t}\langle \rho h \rangle_\varphi + \nabla \cdot \langle \rho h \vec{\mathsf{v}} \rangle_\varphi = -\nabla \cdot \langle \mathbf{q} \rangle_\varphi + \left(\frac{\partial}{\partial t}\langle p \rangle_\varphi + \langle \vec{\mathsf{v}} \cdot \nabla p \rangle_\varphi \right) + \langle \boldsymbol{\tau} : \nabla \vec{\mathsf{v}} \rangle_\varphi + \langle \rho r \rangle_\varphi - \frac{1}{V} \int_{S_i(\vec{\mathsf{x}},t)} \left[\dot{m}_\varphi h_{\varphi i} + \vec{\mathsf{n}}_\varphi \cdot \vec{\mathsf{v}}_i p_{\varphi i} + \vec{\mathsf{n}}_\varphi \cdot \vec{\mathsf{q}}_{\varphi i} \right] dS. \tag{2.4c}$$

is the volume-averaged enthalpy equation, respectively.

2.1.2 Local jump conditions

In order to evaluate the source terms which give the influence of the interface on the bulk flow of each component, one should introduce the jump conditions at the interface. Since the interface is considered as a massless thin surface separating two fluids, the local instant jump conditions at the interface are [5, 20, 24, 6, 10]:

Mass:

$$\sum_{\varphi=1,2} \vec{\mathsf{n}}_\varphi \cdot (\vec{\mathsf{v}}_{\varphi i} - \vec{\mathsf{v}}_i)\rho_{\varphi i} = \dot{m}_1 + \dot{m}_2 = 0 \tag{2.5a}$$

Momentum:

$$\sum_{\varphi=1,2} \{\dot{m}_\varphi \vec{\mathsf{v}}_{\varphi i} - \mathbf{T}_{\varphi i} \cdot \vec{\mathsf{n}}_\varphi\} + \vec{\mathsf{m}}_i^\sigma = 0 \tag{2.5b}$$

where

$$\vec{\mathsf{m}}_i^\sigma = \sigma\kappa\vec{\mathsf{n}} + \nabla_i\sigma \tag{2.5c}$$

is the traction associated with interfacial surface tension, σ is the surface tension coefficient, κ is twice the mean curvature of the interface, $\vec{\mathsf{n}}$ is the normal unit vector to S_i pointing from fluid 1 to fluid 2, and ∇_i is the gradient in the surface coordinates. It is also useful to project this relation on normal and tangential directions to the interface:

$$\dot{m}_1(\vec{\mathsf{v}}_{1i} - \vec{\mathsf{v}}_{2i}) \cdot \vec{\mathsf{n}} - (\boldsymbol{\tau}_{1i} - \boldsymbol{\tau}_{2i}) : \vec{\mathsf{n}}\vec{\mathsf{n}} + (p_{1i} - p_{2i}) = -\sigma\kappa \tag{2.5d}$$

$$\dot{m}_1(\vec{\mathsf{v}}_{1i} - \vec{\mathsf{v}}_{2i}) \cdot \vec{\mathsf{t}} - (\boldsymbol{\tau}_{1i} - \boldsymbol{\tau}_{2i}) : \vec{\mathsf{n}}\vec{\mathsf{t}} = -\nabla_i\sigma \cdot \vec{\mathsf{t}} \tag{2.5e}$$

where, $\vec{\mathsf{t}}$ is an unit vector tangent to S_i.

For the enthalpy the jump condition [5, 10] is:

$$\frac{d_i u_i}{dt} + u_i \nabla_i \cdot \vec{\mathsf{v}}_i = \sum_{\varphi=1,2} \left\{ \dot{m}_\varphi \left(h_{\varphi i} + \frac{1}{2}\mathsf{v}_{\varphi i}^2 - \vec{\mathsf{v}}_{\varphi i} \cdot \vec{\mathsf{v}}_i \right) - (\boldsymbol{\tau}_{\varphi i} \cdot \vec{\mathsf{n}}_\varphi) \cdot (\vec{\mathsf{v}}_{\varphi i} - \vec{\mathsf{v}}_i) + \vec{\mathsf{n}}_\varphi \cdot \vec{\mathsf{q}}_{\varphi i} \right\} \tag{2.5f}$$

$$= \sum_{\varphi=1,2} \left\{ \dot{m}_\varphi (h_{\varphi i} + \frac{1}{2}\mathsf{v}_{\varphi i}^2) - (\vec{\mathsf{n}}_\varphi \cdot \boldsymbol{\tau}_{\varphi i}) \cdot \vec{\mathsf{v}}_{\varphi i} + p_{\varphi i}\vec{\mathsf{v}}_i \cdot \vec{\mathsf{n}}_\varphi + \vec{\mathsf{n}}_\varphi \cdot \vec{\mathsf{q}}_{\varphi i} \right\} + \vec{\mathsf{m}}_i^\sigma \cdot \vec{\mathsf{v}}_i.$$

where u_i is the interfacial internal energy density, d_i/dt is the material derivative in the interface, $h_{\varphi i}$ is the enthalpy of the fluid φ and $\vec{\mathsf{q}}_{\varphi i}$ is the heat flux at the interface S_i. The l.h.s. of (2.5f) represents the increasing rate of interfacial energy per unit interfacial area. On the other hand, the r.h.s. represents the total energy flux by convection, heat flux into the interface and the work exerted on the interface by pressure, stress and interfacial force.

2.1.3 Volume-averaged single-field equations

The equations (2.4a), (2.4b), (2.4c) represent two sets of equations coupled via jump conditions (2.5a), (2.5b), (2.5f) describing the thermodynamics of the two phases. In order to obtain only one set of equations for the whole volume Ω one should sum up these sets of equations and use the jump conditions to evaluate the terms at the interface. Applying this technique one gets:

Mass balance equation:

$$\frac{\partial}{\partial t}\sum_{\varphi=1,2}\langle\rho\rangle_\varphi + \nabla\cdot\sum_{\varphi=1,2}\langle\rho\vec{\mathsf{v}}\rangle_\varphi = 0 \tag{2.6a}$$

Momentum balance equation:

$$\begin{aligned}\frac{\partial}{\partial t}\sum_{\varphi=1,2}\langle\rho\vec{\mathsf{v}}\rangle_\varphi + \nabla\cdot\sum_{\varphi=1,2}\langle\rho\vec{\mathsf{v}}\vec{\mathsf{v}}\rangle_\varphi = -\nabla\sum_{\varphi=1,2}\langle p\rangle_\varphi + \nabla\cdot\sum_{\varphi=1,2}\langle\boldsymbol{\tau}\rangle_\varphi + \sum_{\varphi=1,2}\langle\rho\vec{\mathsf{b}}\rangle_\varphi \\ + \frac{1}{V}\int\limits_{S_i(\vec{\mathsf{x}},t)}(\sigma\kappa\vec{\mathsf{n}} + \nabla_i\sigma)\ dS\end{aligned} \tag{2.6b}$$

Enthalpy equation:

$$\begin{aligned}\frac{\partial}{\partial t}\sum_{\varphi=1,2}\langle\rho h\rangle_\varphi + \nabla\cdot\sum_{\varphi=1,2}\langle\rho h\vec{\mathsf{v}}\rangle_\varphi = -\nabla\cdot\sum_{\varphi=1,2}\langle\vec{\mathsf{q}}\rangle_\varphi + \left(\frac{\partial}{\partial t}\sum_{\varphi=1,2}\langle p\rangle_\varphi + \sum_{\varphi=1,2}\langle\vec{\mathsf{v}}\cdot\nabla p\rangle_\varphi\right) \\ + \sum_{\varphi=1,2}\langle\boldsymbol{\tau}:\nabla\vec{\mathsf{v}}\rangle_\varphi + \sum_{\varphi=1,2}\langle\rho r\rangle_\varphi + \frac{1}{V}\int\limits_{S_i(\vec{\mathsf{x}},t)}\sum_{\varphi=1,2}\left[\frac{1}{2}\dot{m}_\varphi v_{\varphi i}^2 - \vec{\mathsf{v}}_{\varphi i}\cdot\boldsymbol{\tau}_{\varphi i}\cdot\vec{\mathsf{n}}_\varphi\right]\ dS \\ -\frac{1}{V}\int\limits_{S_i(\vec{\mathsf{x}},t)}\left[\frac{d_i u_i}{dt} + u_i\nabla_s\cdot\vec{\mathsf{v}}_i - (\sigma\kappa\vec{\mathsf{n}} + \nabla_i\sigma)\cdot\vec{\mathsf{v}}_i\right]\ dS\end{aligned} \tag{2.6c}$$

The contributions to the energy equation from the interface stretching are usually small compared with the latent heat and have been neglected [20, 23].

At this point it is useful to introduce so called "conserved" variables (see Drew & Passman [6]) to characterize each phase, and the mean quantities to characterize the properties

of the mixture in the volume Ω, respectively. If one defines the volume fraction of the phase φ as

$$\alpha_\varphi = \frac{1}{V}\int_V X_\varphi(\vec{\mathsf{x}}, t)\, dv = \frac{V_\varphi}{V} \tag{2.7}$$

then, the "conserved" variables for each phase φ, and the corresponding mean values, are defined as:

density

$$\overline{\rho}^\varphi = \frac{\langle\rho\rangle_\varphi}{\alpha_\varphi}; \qquad \rho_m(\vec{\mathsf{x}}_C, t) = \sum_{\varphi=1,2}\langle\rho\rangle_\varphi = \sum_{\varphi=1,2}\alpha_\varphi\overline{\rho}^\varphi \tag{2.8a}$$

velocity

$$\overline{\vec{\mathsf{v}}}^\varphi = \frac{\langle\rho\vec{\mathsf{v}}\rangle_\varphi}{\alpha_\varphi\overline{\rho}^\varphi}; \quad \vec{\mathsf{v}}_m(\vec{\mathsf{x}}_C, t) = \frac{\sum\limits_{\varphi=1,2}\langle\rho\vec{\mathsf{v}}\rangle_\varphi}{\sum\limits_{\varphi=1,2}\langle\rho\rangle_\varphi} \tag{2.8b}$$

enthalpy

$$\overline{h}^\varphi = \frac{\langle\rho h\rangle_\varphi}{\alpha_\varphi\overline{\rho}^\varphi}; \quad h_m(\vec{\mathsf{x}}_C, t) = \frac{\sum\limits_{\varphi=1}^{2}\langle\rho h\rangle_\varphi}{\sum\limits_{\varphi=1,2}\langle\rho\rangle_\varphi} \tag{2.8c}$$

Note that for the velocity and enthalpy the mass–averages (or Favré averages) are used instead of component–weighted averages. This type of averaging is useful when compressibility effects are important.

The variables representing the averaged effects of the molecular fluxes are the **stress**

$$\overline{\mathbf{T}}^\varphi = \frac{\langle\mathbf{T}\rangle_\varphi}{\alpha_\varphi}; \quad \mathbf{T}_m(\vec{\mathsf{x}}_C, t) = \sum_{\varphi=1,2}\langle\mathbf{T}\rangle_\varphi \tag{2.8d}$$

or, in terms of pressure and viscous stress

$$\overline{p}^{\varphi} = \frac{\langle p \rangle_{\varphi}}{\alpha_{\varphi}}; \qquad p_m(\vec{\mathsf{x}}_C, t) = \sum_{\varphi=1,2} \langle p \rangle_{\varphi} = \sum_{\varphi=1,2} \alpha_{\varphi} \overline{p}^{\varphi}; \tag{2.8e}$$

$$\overline{\boldsymbol{\tau}}^{\varphi} = \frac{\langle \boldsymbol{\tau} \rangle_{\varphi}}{\alpha_{\varphi}}; \qquad \boldsymbol{\tau}_m(\vec{\mathsf{x}}_C, t) = \sum_{\varphi=1,2} \langle \boldsymbol{\tau} \rangle_{\varphi} = \sum_{\varphi=1,2} \alpha_k \overline{\boldsymbol{\tau}}^{\varphi} \tag{2.8f}$$

and the **heat flux**

$$\overline{\vec{\mathsf{q}}}^{\varphi} = \frac{\langle \vec{\mathsf{q}} \rangle_{\varphi}}{\alpha_{\varphi}}; \qquad \vec{\mathsf{q}}_m(\vec{\mathsf{x}}_C, t) = \sum_{\varphi=1,2} \alpha_{\varphi} \overline{\vec{\mathsf{q}}}^{\varphi}. \tag{2.8g}$$

where $\vec{\mathsf{x}}_C$ is a characteristic point of the volume Ω. The way in which the mean variables are defined suggests that $\vec{\mathsf{x}}_C$ is the position of the center of mass corresponding to the volume Ω. However, the center of mass moves in time due to the variation of the volume fractions. Usually the geometric center of the control volume V is taken to be a good approximation.

Using these notations the equations for the mean values are:

- **Continuity equation:**

$$\frac{\partial \rho_m}{\partial t} + \nabla \cdot \rho_m \vec{\mathsf{v}}_m = 0 \tag{2.9a}$$

- **Momentum equation:**

$$\frac{\partial \rho_m \vec{\mathsf{v}}_m}{\partial t} + \nabla \cdot \langle \rho \vec{\mathsf{v}} \vec{\mathsf{v}} \rangle = -\nabla p_m + \nabla \cdot \boldsymbol{\tau}_m + \rho_m \vec{\mathsf{b}} + \frac{1}{V} \int\limits_{S_i(\vec{\mathsf{x}},t} (\sigma \kappa \vec{\mathsf{n}} + \nabla_i \sigma) \; dS \tag{2.9b}$$

- **Enthalpy equation**

$$\frac{\partial}{\partial t} \rho_m h_m + \nabla \cdot \langle \rho h \vec{\mathsf{v}} \rangle = -\nabla \cdot \vec{\mathsf{q}}_m + \left(\frac{\partial p_m}{\partial t} + \langle \vec{\mathsf{v}} \cdot \nabla p \rangle \right) + \langle \boldsymbol{\tau} : \nabla \vec{\mathsf{v}} \rangle + \langle \rho r \rangle$$
$$+ \frac{1}{V} \int\limits_{S_i(\vec{\mathsf{x}},t)} (\sigma \kappa \vec{\mathsf{n}} + \nabla_i \sigma) \cdot \vec{\mathsf{v}}_i \; dS + \frac{1}{V} \int\limits_{S_i(\vec{\mathsf{x}},t)} \sum_{\varphi=1,2} \left[\frac{1}{2} \dot{m}_{\varphi} |\vec{\mathsf{v}}_{\varphi i}|^2 - \vec{\mathsf{v}}_{\varphi i} \cdot \boldsymbol{\tau}_{\varphi i} \cdot \vec{\mathsf{n}}_{\varphi} \right] \; dS \tag{2.9c}$$

where

$$\langle \Psi \rangle = \sum_{\varphi=1,2} \langle \Psi \rangle_{\varphi} \tag{2.10}$$

is the total averaging operator corresponding to the volume Ω. In [6] and [60] the convective terms are also written using the the mean values. This procedure generates supplemental terms in the momentum and enthalpy equation: "drift" terms which depend on the relative velocity of the center of mass of one phase to center of mass of the other ($\vec{\mathsf{v}}_r = \bar{\vec{\mathsf{v}}}^1 - \bar{\vec{\mathsf{v}}}^2$), and fluctuations terms which are related to phenomena that have characteristic scales smaller than the numerically resolved scale (see [38]). For now, we use the compact formulation because it allows us a simpler formulation. Further analysis will be done in the next chapter (3) when the numerical method will be discussed.

In the equations (2.9b) and (2.9c) one considers that the body forces $\vec{\mathsf{b}}$ are constant over the whole computational domain. This assumption is valid for most of gas-liquid two-phase flow applications where the gravity is the only body force.

2.1.4 Interface constitutive laws

Until this point we did not gave any relation for the entropy either made any assumption regarding the entropy production at the interface. Introducing the interface temperature T_i one could write an entropy inequality at the interface (Ishii [20]):

$$T_i \Delta_i \geq 0 \tag{2.11a}$$

$$T_i \Delta_i = \sum_{\varphi=1,2} \dot{m}_{\varphi} \left[u_{\varphi i} - s_{\varphi i} T_i + \frac{1}{2} |\vec{\mathsf{v}}_{\varphi i} - \vec{\mathsf{v}}_i|^2 + \frac{p_{\varphi i}}{\rho_{\varphi i}} \right] - \vec{\mathsf{n}}_{\varphi} \cdot \boldsymbol{\tau}_{\varphi i} \cdot (\vec{\mathsf{v}}_{\varphi i} - \vec{\mathsf{v}}_i) + \vec{\mathsf{n}}_{\varphi} \cdot \vec{\mathsf{q}}_{\varphi i} \left(1 - \frac{T_i}{T_{\varphi i}} \right) \tag{2.11b}$$

where Δ_i is the entropy production at the interface.

In general, the interfacial jump conditions from 2.1.2 do not constitute sufficient conditions to define the problem uniquely [20]. They should be supplemented by interfacial constitutive laws which satisfy the restriction imposed by the entropy inequality (2.11b). These relations will restrict the kinematical, dynamical and thermal behavior of the two phases.

For a two–phase system in which there is no entropy production at the interface (re-

versible transfer at the interface) Ishii [20] deduced the following conditions:

$$\begin{aligned}
\text{Thermal:} \quad & T_{1i} - T_{2i} = 0 \\
\text{Mechanical:} \quad & p_{1i} - p_{2i} = -\kappa\sigma - \dot{m}_1^2 \left(\frac{1}{\rho_{1i}} - \frac{1}{\rho_{2i}} \right) + (\tau_{nn,1i} - \tau_{nn,2i}) \\
\text{Phase change:} \quad & g_{1i} - g_{2i} = \frac{\dot{m}_1^2}{2} \left(\frac{1}{\rho_{1i}} - \frac{1}{\rho_{2i}} \right) + \left(\frac{\tau_{nn,1i}}{\rho_{1i}} - \frac{\tau_{nn,2i}}{\rho_{2i}} \right)
\end{aligned}$$

where, $g_{\varphi i}$, $\varphi = 1, 2$ are the Gibbs free energy at the interface and $\tau_{nn,\varphi i}$ is the normal component of the viscous stress tensor:

$$\tau_{nn,\varphi i} = \boldsymbol{\tau}_{\varphi i} : \vec{\mathsf{n}}\vec{\mathsf{n}}, \quad \varphi = 1, 2$$

The first condition represents the thermal equilibrium condition at the interface. This thermal boundary condition sets the energy level of the interface and is consistent with the assumption of the existence of the equation of state at the interface. In reality, the discontinuity of the temperature at the interface exists and can be estimated from the kinetic theories. However, its value is very small in comparison with the absolute temperature for most of the materials [20] (exception – liquid metals). In [18] a condition of thermodynamic equilibrium is used so that the saturation temperature is uniquely determined by the pressure through the Clapeyron relation. In this case the temperature will be discontinuous since the pressure of the gas and liquid are different. Huang and Joseph [17] used both the thermal and thermodynamic equilibrium conditions to study the instability of a liquid below its vapor. They have observed that the results of the stability analysis do not depend strongly on the choice of the conditions for the temperature at the interface in the case of water and water vapor.

The second condition is identical with (2.5d) and expresses the momentum jump condition in the normal direction under the condition of no–slip, that is the tangential velocity is continuous at the interface. This assumption is valid for most of the physical problems with two possible exceptions: flow of rarefied gases and motion of a contact line over a solid surface [16]. For a static interface this condition reduces to: $p_{2i} - p_{1i} = \kappa\sigma$. This condition, under standard conditions, can be simplified neglecting the normal stresses which are very small comparing with the pressure terms. The same argument can be applied to the third condition, since the order of magnitude of the term $\rho_{\varphi i} g_{\varphi i}$ is $p_{\varphi i}$.

Since in the field equations the Gibbs free energy does not appear explicitly, it is desirable to transform the variable $g_{\varphi i}$ into other variables using an equation of state. This equation of state is strongly related to each type problem that is simulated.

2.2 Volume fraction advection equation

In order to complete the set of equations we need an equation for the volume fraction. Generally, the advection of the volume fraction f is governed by:

$$\frac{\partial f}{\partial t} + \vec{\mathsf{v}}_\Sigma \cdot \nabla f = \int_{S_i} \vec{\mathsf{v}}_i \cdot \vec{\mathsf{n}}\, dS \tag{2.12}$$

where $\vec{\mathsf{v}}_\Sigma$ is a smooth velocity field that matches the interface velocity $\vec{\mathsf{v}}_i$ at the interface S_i. If there is no expansion at the interface and the fluids are incompressible, $\vec{\mathsf{v}}_\Sigma$ could be the fluid velocity (Tryggvason [53]). For the general case one should compute the interface velocity in order to advect the fraction of volume. From (2.5a) one has:

$$\vec{\mathsf{n}} \cdot \vec{\mathsf{v}}_i(\rho_{1i} - \rho_{2i}) = \vec{\mathsf{n}} \cdot (\rho_{1i}\vec{\mathsf{v}}_{1i} - \rho_{2i}\vec{\mathsf{v}}_{2i}) \tag{2.13}$$

Introducing the averaged values for velocity and density (2.8a), (2.8b) one has:

$$\begin{aligned}\vec{\mathsf{n}} \cdot \vec{\mathsf{v}}_i(\overline{\rho}^1 - \overline{\rho}^2) + \vec{\mathsf{n}} \cdot \vec{\mathsf{v}}_i(\delta_{1i}\rho - \delta_{2i}\rho) = \vec{\mathsf{n}} \cdot (\overline{\rho}^1\overline{\vec{\mathsf{v}}}^1 - \overline{\rho}^2\overline{\vec{\mathsf{v}}}^2) \\ + \vec{\mathsf{n}} \cdot (\overline{\rho}^1\delta_{1i}\vec{\mathsf{v}} - \overline{\rho}^2\delta_{2i}\vec{\mathsf{v}}) + \vec{\mathsf{n}} \cdot (\delta_{1i}\rho\overline{\vec{\mathsf{v}}}^1 - \delta_{2i}\rho\overline{\vec{\mathsf{v}}}^2) + \vec{\mathsf{n}} \cdot (\delta_{1i}\rho\delta_{1i}\vec{\mathsf{v}} - \delta_{2i}\rho\delta_{2i}\vec{\mathsf{v}})\end{aligned} \tag{2.14}$$

where, $\delta_{\varphi i}\rho$ and $\delta_{\varphi i}\vec{\mathsf{v}}$ with $\varphi = 1, 2$ are the deviations from the averaged values of the density and velocity at the interface. If the control volume V is small enough it is reasonable to suppose that these deviations are much smaller than the averaged values (at least one order of magnitude). Keeping only the first order terms one has:

$$\vec{\mathsf{n}} \cdot \vec{\mathsf{v}}_i(\overline{\rho}^1 - \overline{\rho}^2) = \vec{\mathsf{n}} \cdot (\overline{\rho}^1\overline{\vec{\mathsf{v}}}^1 - \overline{\rho}^2\overline{\vec{\mathsf{v}}}^2) \tag{2.15}$$

This equation gives a relation between the normal component of the interface velocity $\vec{\mathsf{v}}_i$ and the local momentum fluxes over the interface. The tangential component is still an unknown quantity. It only appears in the dissipation term of the entropy inequality and it is usually taken to be equal with the tangential component of the velocity in the no–slip

hypothesis introduced by Ishii [20]. Note that if the fluids have the same density ($\overline{\rho}^1 = \overline{\rho}^2$) the interface velocity can not be determined except for the case when there is no phase change at the interface. In this situation $\dot{m}_1 = \dot{m}_2 = 0$ and the interface moves with the same velocity as the two fluids. Hereafter we assume that $\overline{\rho}^1 \neq \overline{\rho}^2$ if not mentioned otherwise.

Equation (2.15) can be written using the mean velocity and mean density:

$$\vec{\mathsf{n}} \cdot \vec{\mathsf{v}}_i = \vec{\mathsf{n}} \cdot \vec{\mathsf{v}}_m + \frac{\overline{\rho}^1 \overline{\rho}^2}{\rho_m (\overline{\rho}^1 - \overline{\rho}^2)} \vec{\mathsf{n}} \cdot (\overline{\vec{\mathsf{v}}}^1 - \overline{\vec{\mathsf{v}}}^2) \tag{2.16}$$

2.3 Incompressible fluids: homogenous model

In most of the applications for two-phase flows with technical relevance the fluids can be considered as incompressible. This means that the averaged density, or viscosity, of phase φ over the domain Ω_φ is constant, i.e. $\overline{\rho}^\varphi = \rho_\varphi$. However, ρ_m depends on the volume fractions of each phase and it is not constant. Therefore, the momentum equation (2.9b) and the enthalpy equation (2.9c) can not be simplified as for the single phase equations.

To see what are the implications of this assumption on the continuity equation (2.9a) and on the advection equation of the volume fraction one has to rewrite these equations in a form similar to the single phase case using the fact that the densities of the fluids are constant. Thus, for each phase φ the velocity field is solenoidal, that is:

$$\nabla \cdot \vec{\mathsf{v}}_\varphi = 0. \tag{2.17}$$

If, we apply the same procedure as before ($\langle \vec{\mathsf{v}} \rangle_\varphi = \overline{\vec{\mathsf{v}}}^\varphi$ for the incompressible case) the continuity equation for the incompressible fluids becomes:

$$\nabla \cdot \left[f \overline{\vec{\mathsf{v}}}^1 + (1-f) \overline{\vec{\mathsf{v}}}^2 \right] = -\frac{1}{V} \int_{S_i} (\vec{\mathsf{v}}_{1i} - \vec{\mathsf{v}}_{2i}) \cdot \vec{\mathsf{n}} \, dS \, , \tag{2.18}$$

where the notation f is used instead of α_1 and $(1-f)$ instead of α_2. Starting from (2.4a)

two equations for volume fraction can be deduced:

$$\frac{\partial f}{\partial t} + \nabla \cdot (f\bar{\vec{\mathsf{v}}}^1) = \frac{\rho_2}{\rho_1 - \rho_2}\frac{1}{V}\int_{S_i} (\vec{\mathsf{v}}_{1i} - \vec{\mathsf{v}}_{2i}) \cdot \vec{\mathsf{n}}\, dS \tag{2.19a}$$

$$\frac{\partial f}{\partial t} - \nabla \cdot \left[(1-f)\bar{\vec{\mathsf{v}}}^2\right] = \frac{\rho_1}{\rho_1 - \rho_2}\frac{1}{V}\int_{S_i} (\vec{\mathsf{v}}_{1i} - \vec{\mathsf{v}}_{2i}) \cdot \vec{\mathsf{n}}\, dS \tag{2.19b}$$

Note that (2.18) can also be obtained by subtracting (2.19b) from (2.19a). Introducing the mixture velocity one has:

$$\nabla \cdot \vec{\mathsf{v}}_m = \nabla \cdot \left[f(1-f)\frac{\rho_1 - \rho_2}{\rho_m}(\bar{\vec{\mathsf{v}}}^1 - \bar{\vec{\mathsf{v}}}^2)\right] - \frac{1}{V}\int_{S_i} (\vec{\mathsf{v}}_{1i} - \vec{\mathsf{v}}_{2i}) \cdot \vec{\mathsf{n}}\, dS \tag{2.20}$$

from (2.18) and summing up (2.19a) and (2.19b)

$$\frac{\partial f}{\partial t} + \nabla \cdot (f\vec{\mathsf{v}}_m) = \frac{1}{2}\frac{\rho_1 + \rho_2}{\rho_1 - \rho_2}\frac{1}{V}\int_{S_i} (\vec{\mathsf{v}}_{1i} - \vec{\mathsf{v}}_{2i}) \cdot \vec{\mathsf{n}}\, dS + \frac{1}{2}\nabla \cdot \left[\vec{\mathsf{v}}_m - f(1-f)\frac{\rho_1 + \rho_2}{\rho_m}(\bar{\vec{\mathsf{v}}}^1 - \bar{\vec{\mathsf{v}}}^2)\right] \tag{2.21}$$

From (2.20) one can see that even when no phase change at the interface occurs the mean velocity field is not solenoidal. Also the volume fraction advection equation is more complicated as compared with standard VOF method [31, 28]. However, the supplemental term

$$\frac{1}{2}\nabla \cdot \left[\vec{\mathsf{v}}_m - f(1-f)\frac{\rho_1 + \rho_2}{\rho_m}(\bar{\vec{\mathsf{v}}}^1 - \bar{\vec{\mathsf{v}}}^2)\right]$$

becomes important only when the volume fraction f is of the same order of magnitude as $1/(1 + \rho_2/\rho_1)$.

For the case when there is no phase change at the interface, (2.20) can be written as:

$$\nabla \cdot \left[f(1-f)\frac{1}{\rho_m}(\bar{\vec{\mathsf{v}}}^1 - \bar{\vec{\mathsf{v}}}^2)\right] = \frac{1}{\rho_1 - \rho_2}\nabla \cdot \vec{\mathsf{v}}_m \tag{2.22}$$

Replacing in (2.21) the liquid volume fraction advection equation (2.21) is:

$$\frac{\partial f}{\partial t} + \nabla \cdot (f\vec{\mathsf{v}}_m) = -\frac{\Gamma_\rho}{1 - \Gamma_\rho}\nabla \cdot \vec{\mathsf{v}}_m \tag{2.23}$$

where, $\Gamma_\rho = \rho_2/\rho_1$. Thus, for incompressible flows without mass transfer choosing the advection equation for volume fraction to be:

$$\frac{\partial f}{\partial t} + \nabla \cdot (f\vec{\mathsf{v}}_m) = 0 \tag{2.24a}$$

is consistent with the approximation of a divergence–free mean velocity field

$$\nabla \cdot \vec{\mathsf{v}}_m = 0 \tag{2.24b}$$

The question is in which conditions the mean velocity field $\vec{\mathsf{v}}_m$ can be approximated as solenoidal. From (2.22) one can see that (2.24b) requires the averaged velocities $\bar{\vec{\mathsf{v}}}^1$ and $\bar{\vec{\mathsf{v}}}^2$ are equal. When there is no mass transfer due to phase change across the interface the velocity field is continuous and, if the control volume is very small the divergence of the mean velocity can be approximated to be zero. Thus, a divergence–free condition for the mean velocity field is recovered. In [60] this approximation is called *homogenous model*. Further on we suppose that the condition for a solenoidal velocity field are always met, if not specified otherwise.

2.4 Dimensionless equations

The equations (2.9a), (2.9b) and (2.9c) are considering the effects of all the mechanical and thermal phenomena disregarding the different orders of magnitude of the terms describing those phenomena. In order to emphasize the order of magnitude of different terms it is useful to consider the dimensionless form of the equations. Let ℓ^*, v^*, ρ^* and T^* be the characteristic values for the length, velocity, density and temperature, respectively. Since the temperature is variable we need to introduce characteristic values also for thermal conductivity (λ^*), viscosity (μ^*) and surface tension (σ^*). All these reference values are indicated using a star as superscript. With these values one can deduce further characteristic parameters:

- characteristic time scale (t^*): $t^* = \ell^*/\mathsf{v}^*$;
- characteristic pressure (p^*): for the liquid phase pressure $\rho^*(\mathsf{v}^*)^2$ is a reasonable choice for problems where the dynamic effects are more important then buoyancy effects.

At the interface the pressure in the gas phase (inside of the bubble) is related to the liquid pressure via the jump condition (2.5d). Assuming that no phase change occurs

$$p_{2i} - p_{1i} = \sigma\kappa + (\boldsymbol{\tau}_{2i} - \boldsymbol{\tau}_{1i}) : \vec{\mathsf{n}}\vec{\mathsf{n}}$$

and, therefore, the order of magnitude of the pressure in the gas phase near the interface p_{2i} is

$$p_{2i} \propto \rho^*(\mathsf{v}^*)^2 \left(1 + \frac{1}{\mathsf{We}} + \frac{1}{\mathsf{Re}}\right) \tag{2.25}$$

where

$$\mathsf{Re} = \frac{\rho^*\mathsf{v}^*\ell^*}{\mu^*} \quad \text{is the Reynolds number} \tag{2.26}$$

$$\mathsf{We} = \frac{\rho^*(\mathsf{v}^*)^2\ell^*}{\sigma^*} \quad \text{is the Weber number} \tag{2.27}$$

Then, for the mixture pressure in a volume containing both fluids one has

$$p_m \propto \rho^*(\mathsf{v}^*)^2 \left[1 + (1-f)\left(\frac{1}{\mathsf{We}} + \frac{1}{\mathsf{Re}}\right)\right] \tag{2.28}$$

This relation shows that p_m has the same order of magnitude as $\rho^*(\mathsf{v}^*)^2$ if $\mathsf{We} > 1$ and $\mathsf{Re} > 1$. For a more detailed discussion regarding other effects and their influence on the pressure jump see Sadhal *et al.* [40] (pg. 19–20).

- characteristic enthalpy (h^*): $h^* = C_pT^*$;

Using these characteristic values the dimensionless variables are:

Length	$\tilde{x}_i = x_i/\ell^*, \quad i = 1,2,3$
Velocity	$\tilde{\vec{\mathsf{v}}} = \vec{\mathsf{v}}/\mathsf{v}^*$
Time	$\tilde{t} = t/t^* = t\mathsf{v}^*/\ell^*$
Enthalpy	$\tilde{h} = h/h^*$
Density	$\tilde{\rho} = \rho/\rho^*$
Heat flux	$\tilde{\vec{\mathsf{q}}} = \vec{\mathsf{q}}\ell^*/(\lambda^*T^*)$
Pressure	$\tilde{p} = p/(\rho^*(\mathsf{v}^*)^2)$
Dynamic viscosity	$\tilde{\mu} = \mu/\mu^*$
Surface tension	$\tilde{\sigma} = \sigma/\sigma^*$

Viscous stress tensor	$\tilde{\boldsymbol{\tau}} = (\ell^*/\mu^*\mathsf{v}^*)\boldsymbol{\tau}$
Volume	$\tilde{V} = V/(\ell^*)^3$
Interface surface	$\tilde{S}_i = S_i/(\ell^*)^2$
Interface curvature	$\tilde{\kappa} = \kappa/\ell^*$

The equations for the dimensionless variables are:

$$\frac{\partial \tilde{\rho}_m}{\partial \tilde{t}} + \tilde{\nabla} \cdot \tilde{\rho}_m \tilde{\vec{\mathsf{v}}}_m = 0 \tag{2.29}$$

$$\frac{\partial \tilde{\rho}_m \tilde{\vec{\mathsf{v}}}_m}{\partial \tilde{t}} + \tilde{\nabla} \cdot \langle \tilde{\rho} \tilde{\vec{\mathsf{v}}} \tilde{\vec{\mathsf{v}}} \rangle = -\frac{p^*}{\rho^* (\mathsf{v}^*)^2} \tilde{\nabla} \tilde{p}_m + \frac{\mu^*}{\rho^* \mathsf{v}^* \ell^*} \tilde{\nabla} \cdot \tilde{\boldsymbol{\tau}}_m + \frac{\ell^*}{(\mathsf{v}^*)^2} \tilde{\rho}_m \vec{\mathsf{g}} + \frac{\sigma^*}{\rho^* (\mathsf{v}^*)^2 \ell^*} \frac{1}{\tilde{V}} \int_{\tilde{S}_i} \left(\tilde{\sigma} \tilde{\kappa} \vec{\mathsf{n}} + \tilde{\nabla}_i \tilde{\sigma} \right) \, dS \tag{2.30}$$

$$\begin{aligned} \frac{\partial \tilde{\rho}_m \tilde{h}_m}{\partial \tilde{t}} + \tilde{\nabla} \cdot \langle \tilde{\rho} \tilde{h} \tilde{\vec{\mathsf{v}}} \rangle = & -\frac{\lambda^* T^*}{\rho^* h^* \mathsf{v}^* \ell^*} \tilde{\nabla} \cdot \tilde{\vec{\mathsf{q}}}_m + \frac{\ell^* r^*}{h^* \mathsf{v}^*} \tilde{\rho}_m \tilde{r} + \frac{p^*}{\rho^* h^*} \left(\frac{\partial \tilde{p}_m}{\partial \tilde{t}} + \langle \tilde{\vec{\mathsf{v}}} \cdot \tilde{\nabla} \tilde{p} \rangle \right) \\ & + \frac{\mu^* \mathsf{v}^*}{\rho^* h^* \ell^*} \langle \tilde{\boldsymbol{\tau}} : \tilde{\nabla} \tilde{\vec{\mathsf{v}}} \rangle - \frac{\mu^* \mathsf{v}^*}{\rho^* h^* \ell^*} \frac{1}{\tilde{V}} \int_{\tilde{S}_i} \sum_{\varphi=1}^{2} \tilde{\vec{\mathsf{v}}}_{\varphi i} \cdot \tilde{\boldsymbol{\tau}}_{\varphi i} \cdot \vec{\mathsf{n}}_\varphi \, dS \\ & + \frac{\sigma^*}{\rho^* h^* \ell^*} \frac{1}{\tilde{V}} \int_{\tilde{S}_i} (\tilde{\sigma} \tilde{\kappa} \vec{\mathsf{n}} + \tilde{\nabla}_i \tilde{\sigma}) \cdot \tilde{\vec{\mathsf{v}}}_i \, dS + \frac{(\mathsf{v}^*)^2}{h^*} \frac{1}{\tilde{V}} \int_{\tilde{S}_i} \sum_{\varphi=1}^{2} \frac{1}{2} \tilde{\dot{m}}_\varphi |\tilde{\vec{\mathsf{v}}}_{\varphi i}|^2 \, dS \end{aligned} \tag{2.31}$$

where, the general body force $\vec{\mathsf{b}}$ was replaced by the gravity $\vec{\mathsf{g}}$. For simplicity, we drop the tilde notation for the dimensionless variables and introduce the dimensionless numbers:

$$\mathtt{Fr} = \frac{\ell^* g}{(\mathsf{v}^*)^2} \qquad \text{is the Froude number} \tag{2.32}$$

$$\mathtt{Pr} = \frac{C_p \mu^*}{\lambda^*} \qquad \text{is the Prandtl number} \tag{2.33}$$

$$\mathtt{Pe} = \mathtt{PrRe} = \frac{\rho^* C_p \mathsf{v}^* \ell^*}{\lambda^*} \quad \text{is the Peclet number} \tag{2.34}$$

then the dimensionless equations are:

$$\frac{\partial \rho}{\partial t} + \nabla \cdot \rho \vec{\mathsf{v}}_m = 0 \tag{2.35a}$$

$$\frac{\partial \rho_m \vec{\mathsf{v}}_m}{\partial t} + \nabla \cdot \langle \rho \vec{\mathsf{v}} \vec{\mathsf{v}} \rangle = -\nabla p_m + \frac{1}{\mathtt{Re}} \nabla \cdot \boldsymbol{\tau}_m + \frac{1}{\mathtt{Fr}} \rho_m \frac{\vec{\mathsf{g}}}{g} + \frac{1}{\mathtt{We}} \frac{1}{V} \int\limits_{\tilde{S}_i} (\sigma \kappa \vec{\mathsf{n}} + \nabla_i \sigma) \; dS \tag{2.35b}$$

$$\begin{aligned} \frac{\partial \rho_m h_m}{\partial t} + \nabla \cdot \langle \rho h \vec{\mathsf{v}} \rangle = & -\frac{1}{\mathtt{Pe}} \nabla \cdot \vec{\mathsf{q}}_m + \frac{\ell^* r^*}{h^* \mathsf{v}^*} \rho_m r \\ & + \frac{(\mathsf{v}^*)^2}{h^*} \left[\left(\frac{\partial p_m}{\partial t} + \langle \vec{\mathsf{v}} \cdot \nabla p \rangle \right) + \frac{1}{V} \int\limits_{\tilde{S}_i} \sum_{\varphi=1}^{2} \frac{1}{2} \dot{m}_\varphi |\vec{\mathsf{v}}_{\varphi i}|^2 \; dS \right] \\ & + \frac{(\mathsf{v}^*)^2}{h^*} \frac{1}{\mathtt{Re}} \left(\langle \boldsymbol{\tau} : \nabla \vec{\mathsf{v}} \rangle - \frac{1}{\tilde{V}} \int\limits_{\tilde{S}_i} \sum_{\varphi=1}^{2} \vec{\mathsf{v}}_{\varphi i} \cdot \boldsymbol{\tau}_{\varphi i} \cdot \vec{\mathsf{n}}_\varphi \; dS \right) \\ & + \frac{(\mathsf{v}^*)^2}{h^*} \frac{1}{\mathtt{We}} \frac{1}{V} \int\limits_{\tilde{S}_i} (\sigma \kappa \vec{\mathsf{n}} + \nabla_i \sigma) \cdot \vec{\mathsf{v}}_i \; dS \end{aligned} \tag{2.35c}$$

2.4.1 Dimensionless equations for incompressible flows

In the enthalpy equation $\dot{m}_k$ has been considered to be of the same order as $\rho^* \mathsf{v}^*$. With this assumption the term giving the influence of the kinetic energy transfer at the interface has the same order of magnitude as the work term. For incompressible and weakly compressible flows, $(\mathsf{v}^*)^2/h^*$ is small and the terms having this order can be neglected. Thus, the dimensionless equations for an incompressible two-phase flow are:

$$\nabla \cdot \vec{\mathsf{v}}_m = 0 \tag{2.36a}$$

$$\frac{\partial \rho_m \vec{\mathsf{v}}_m}{\partial t} + \nabla \cdot \langle \rho \vec{\mathsf{v}} \vec{\mathsf{v}} \rangle = -\nabla P_m + \frac{1}{\mathtt{Re}} \nabla \cdot \boldsymbol{\tau}_m - (1-f) \frac{\mathtt{Eo}}{\mathtt{We}} \frac{\vec{\mathsf{g}}}{g} + \frac{1}{\mathtt{We}} \frac{1}{V} \int\limits_{\tilde{S}_i} (\sigma \kappa \vec{\mathsf{n}} + \nabla_i \sigma) \; dS \tag{2.36b}$$

$$\frac{\partial \rho_m h_m}{\partial t} + \nabla \cdot \langle \rho h \vec{\mathsf{v}} \rangle = -\frac{1}{\mathtt{Pe}} \nabla \cdot \vec{\mathsf{q}}_m + \frac{\ell^* r^*}{h^* \mathsf{v}^*} \rho_m r \tag{2.36c}$$

while the volume fraction advection equation is:

$$\frac{\partial f}{\partial t} + \nabla \cdot (f\vec{\mathtt{v}}_m) = 0 \tag{2.36d}$$

In (2.36b) we take advantage of the incompressibility of the fluids and introduce the *reduced pressure* field P defined as the pressure field from which we subtract the hydrostatic pressure of the continuous phase:

$$P_m = p_m - \frac{1}{\mathtt{Fr}}\frac{\rho_1}{\rho^*}\frac{\vec{\mathtt{g}}}{g}\cdot\vec{\mathtt{x}} \tag{2.37}$$

Thus, in the momentum equation (2.36b) the buoyancy term $(1-f)\frac{\mathtt{Eo}}{\mathtt{We}}\frac{\vec{\mathtt{g}}}{g}$ appears. The Eötvös number

$$\mathtt{Eo} = (\rho_1 - \rho_2)\frac{g(\ell^*)^2}{\sigma^*} \tag{2.38}$$

is the square of the ratio between characteristic length and Laplace constant (neutral interfacial wavelength predicted by the Taylor stability analysis).

2.4.2 Dimensionless jump conditions

For incompressible two-phase flow without phase change the interface jump conditions for momentum are:

$$(p_{1i} - p_{2i}) - \frac{1}{\mathtt{Re}}(\boldsymbol{\tau}_{1i} - \boldsymbol{\tau}_{2i}) : \vec{\mathtt{n}}\vec{\mathtt{n}} = -\frac{1}{\mathtt{We}}\sigma\kappa \tag{2.39}$$

$$\frac{1}{\mathtt{Re}}(\boldsymbol{\tau}_{1i} - \boldsymbol{\tau}_{2i}) : \vec{\mathtt{n}}\vec{\mathtt{t}} = \frac{1}{\mathtt{We}}\nabla_i\sigma\cdot\vec{\mathtt{t}} \tag{2.40}$$

while, for the energy the jump condition (2.5f) reduces to

$$(\vec{\mathtt{q}}_{1i} - \vec{\mathtt{q}}_{2i})\cdot\vec{\mathtt{n}} = 0 \tag{2.41}$$

which states that when no phase change occurs at the interface the normal component of the heat flux is continuous.

3. NUMERICAL METHOD

In the previous chapter the volume-averaged equations for the mass, momentum and enthalpy were introduced. For incompressible adiabatic flows, Sabisch [38] and Sabisch *et al.* [39] developed a new numerical method, which combines the Volume-of-Fluid interface tracking technique with the solution of the dimensionless equations (2.36a) and (2.36b) using a projection method. A third order Runge-Kutta scheme approximate the time evolution while a finite volume formulation on a staggered grid is used for the spatial discretization of the momentum equation. For the interface reconstruction, a new piecewise linear algorithm (`EPIRA`) was developed. This method is used to simulate single gas bubbles [39] or swarm of bubbles [38] rising in a plane channel due to the buoyancy effects.

To simulate problems where the heat/mass transfer are important, one has also to solve the energy equation (2.36c). In this chapter, an extension of the original method from Sabisch [38] is introduced for the case of non-adiabatic flows without phase change at the interface. Under the assumption of constant fluids properties (see Chapter 4) the momentum equation is independent of the energy equation and can be solved before computing the enthalpy (temperature) field. Therefore, further on, the velocity field is assumed to be known for all time steps.

This chapter is structured as follows: first, the numerical treatment of the enthalpy equation (2.36c) will be discussed. Verification of the method for single phase forced convection in a rectangular channel will be presented. The method will also be tested for single phase natural convection of liquid metals and of air in a rectangular, respectively square, box.

3.1 Numerical procedure

The idea is to apply the volume averaged equation (2.36c) for each volume cell of the computational domain. Let us consider that our computational domain is discretized in $\mathtt{IM} \times \mathtt{JM} \times \mathtt{KM}$ cells, each one having the dimensions Δx, Δy and Δz_k. The grid is supposed

to be equidistant in x and y-directions and, only the cell dimension in z may vary. For a computational cell (i, j, k) the enthalpy equation is:

$$\frac{\partial \rho_{i,j,k} h_{i,j,k}}{\partial t} + \left[\nabla \cdot \langle \rho h \vec{\mathsf{v}} \rangle\right]_{i,j,k} = -\frac{1}{\mathtt{Pe}} \left[\nabla \cdot \langle \vec{\mathsf{q}} \rangle\right]_{i,j,k} \tag{3.1}$$

This equation expresses the time evolution of the volume-averaged value of the enthalpy $h_{i,j,k}$ corresponding to the cell (i, j, k), taking in account the heat fluxes across the cell boundaries. The numerical approximation of the convective and conductive terms will be introduced in section 3.1.1 and 3.1.2, respectively. The time integration and time-step criteria will be discussed in section 3.1.3.

3.1.1 Convective term approximation

The convective term in (3.1) can be written as the sum of enthalpy fluxes over the control volume boundary (cell faces):

$$\left[\nabla \cdot \langle \rho h \vec{\mathsf{v}} \rangle\right]_{i,j,k} = \sum_{\ell} \frac{S_\ell}{V_{i,j,k}} \frac{1}{S_\ell} \int\limits_{S_\ell} \rho h \vec{\mathsf{v}} \cdot \vec{\mathsf{n}}_\ell \, dS \;, \tag{3.2}$$

where S_ℓ are the faces of a centered cell $V_{i,j,k}$ and $\vec{\mathsf{n}}_\ell$ is its normal vector pointing outside the domain. These fluxes have to be constructed using the volume-averaged values of the enthalpy $h_{i,j,k}$ corresponding to the mesh cell (i, j, k) and the discrete velocity obtained from the numerical integration of the momentum equation.

Let us consider the face $S_{i,j,k+\frac{1}{2}}$ and evaluate the enthalpy convective flux through this face. Using the fact that the fluids are incompressible and supposing that the heat capacity C_p of each fluid is constant one has

$$\frac{1}{S_{i,j,k+\frac{1}{2}}} \int\limits_{S_{i,j,k+\frac{1}{2}}} \rho h w \, dS = f^S_{i,j,k+\frac{1}{2}} \rho_1 C_{p,1} \int\limits_{S^1_{i,j,k+\frac{1}{2}}} T w \, dS + (1 - f^S_{i,j,k+\frac{1}{2}}) \rho_2 C_{p,2} \int\limits_{S^2_{i,j,k+\frac{1}{2}}} T w \, dS \tag{3.3}$$

where, w is the velocity component in z-direction, and $f^S_{i,j,k+\frac{1}{2}}$ is the fraction of the face $S_{i,j,k+\frac{1}{2}}$ occupied by the fluid 1

$$f^S_{i,j,k+\frac{1}{2}} = \frac{S^1_{i,j,k+\frac{1}{2}}}{S_{i,j,k+\frac{1}{2}}} \tag{3.4}$$

This part is designated by $S^1_{i,j,k+\frac{1}{2}}$ while the part of the face inside the other fluid is $S^2_{i,j,k+\frac{1}{2}}$.

On the face $S_{i,j,k+\frac{1}{2}}$, the fluids are assumed in thermal equilibrium [25], that is

$$\frac{1}{S^1_{i,j,k+\frac{1}{2}}} \int\limits_{S^1_{i,j,k+\frac{1}{2}}} T \, dS = \frac{1}{S^2_{i,j,k+\frac{1}{2}}} \int\limits_{S^2_{i,j,k+\frac{1}{2}}} T \, dS = T_{i,j,k+\frac{1}{2}} \tag{3.5}$$

Thus, the temperature for each phase is $T = T_{i,j,k+\frac{1}{2}} + T'$ where T' is the local deviation from the mean value $T_{i,j,k+\frac{1}{2}}$. For the velocities let

$$\frac{1}{S^1_{i,j,k+\frac{1}{2}}} \int\limits_{S^1_{i,j,k+\frac{1}{2}}} w \, dS = w^1_{i,j,k+\frac{1}{2}} \tag{3.6a}$$

$$\frac{1}{S^2_{i,j,k+\frac{1}{2}}} \int\limits_{S^2_{i,j,k+\frac{1}{2}}} w \, dS = w^2_{i,j,k+\frac{1}{2}} \tag{3.6b}$$

be the surface averaged values corresponding to each phase. Similar to the temperature field, the velocity can be expressed as

$$w_1 = w^1_{i,j,k+\frac{1}{2}} + w'_1 \tag{3.7a}$$

$$w_2 = w^2_{i,j,k+\frac{1}{2}} + w'_2 \tag{3.7b}$$

Introducing in (3.3) one gets:

$$\begin{aligned} \frac{1}{S_{i,j,k+\frac{1}{2}}} \int\limits_{S_{i,j,k+\frac{1}{2}}} \rho h w \, dS = & \left[f^S_{i,j,k+\frac{1}{2}} \rho_1 C_{p,1} w^1_{i,j,k+\frac{1}{2}} + (1 - f^S_{i,j,k+\frac{1}{2}}) \rho_2 C_{p,2} w^2_{1,j,k+\frac{1}{2}} \right] T_{i,j,k+\frac{1}{2}} \\ & + f^S_{i,j,k+\frac{1}{2}} \rho_1 C_{p,1} \int\limits_{S^1_{i,j,k+\frac{1}{2}}} T'_1 w'_1 \, dS + (1 - f^S_{i,j,k+\frac{1}{2}}) \rho_2 C_{p,2} \int\limits_{S^2_{i,j,k+\frac{1}{2}}} T'_2 w'_2 \, dS \end{aligned} \tag{3.8a}$$

The second term in r.h.s. expresses the contribution of the local spatial fluctuations of the temperature and velocity to the convective heat flux. This term depends on the size of the grid used in the computations and becomes vanishing small with decreasing mesh size. In the literature [42] they are called Sub-Grid Scale (SGS) terms; they express phenomena having characteristic length smaller than the grid size and for coarse grids they have to be

computed using appropriate models. In this study we are concerned with Direct Numerical Simulation of a two-phase flow and we implicitly suppose that the grid is fine enough so that SGS terms are smaller than the error of the numerical scheme and will be ignored. The first term in r.h.s. represents the resolved part of the enthalpy convective flux, and it is expressed in terms of surface averages of temperature and velocities. If $w^S_{i,j,k+\frac{1}{2}}$ denotes the face mixture velocity, then

$$\frac{1}{S_{i,j,k+\frac{1}{2}}}\int\limits_{S_{i,j,k+\frac{1}{2}}} \rho h w \, dS \simeq \left[f^S_{i,j,k+\frac{1}{2}}\rho_1 C_{p,1} + (1-f^S_{i,j,k+\frac{1}{2}})\rho_2 C_{p,2}\right] w^S_{i,j,k+\frac{1}{2}} T_{i,j,k+\frac{1}{2}}$$
$$- \frac{f^S_{i,j,k+\frac{1}{2}}\rho_1(1-f^S_{i,j,k+\frac{1}{2}})\rho_2}{\left[f^S_{i,j,k+\frac{1}{2}}\rho_1 + (1-f^S_{i,j,k+\frac{1}{2}})\rho_2\right]}(C_{p,1}-C_{p,2})(w^1_{i,j,k+\frac{1}{2}} - w^2_{1,j,k+\frac{1}{2}})T_{i,j,k+\frac{1}{2}} \quad (3.8b)$$

Since the equations (2.36a, 2.36b, 2.36c) were derived under the assumption that, inside a cell, both phases move with the same velocity (homogenous model), the last term in (3.8b) vanishes. Thus, the enthalpy convective flux through the face $S_{i,j,k+\frac{1}{2}}$ can be approximated by

$$\frac{1}{S_{i,j,k+\frac{1}{2}}}\int\limits_{S_{i,j,k+\frac{1}{2}}} \rho h w \, dS \simeq (\rho C_p)_{i,j,k+\frac{1}{2}} w^S_{i,j,k+\frac{1}{2}} T_{i,j,k+\frac{1}{2}} \quad (3.8c)$$

with,

$$(\rho C_p)_{i,j,k+\frac{1}{2}} = f^S_{i,j,k+\frac{1}{2}}\rho_1 C_{p,1} + (1-f^S_{i,j,k+\frac{1}{2}})\rho_2 C_{p,2} \quad (3.9)$$

In the formulas above the velocity $w_{i,j,k+\frac{1}{2}}$ can be approximated with a precision up to second order by the staggered volume mixture velocity $w_{i,j,k+\frac{1}{2}}$ available from the integration of the Navier-Stokes equations. For the other quantities ($f^S_{i,j,k+\frac{1}{2}}$, $T_{i,j,k+\frac{1}{2}}$) supplementary assumptions have to be made.

The cell face temperature $T_{i,j,k+\frac{1}{2}}$ can be evaluated using a piecewise linear reconstruction between the values in the cells (i,j,k) and $(i,j,k+1)$. Thus

$$T_{i,j,k+\frac{1}{2}} \simeq \frac{T_{i,j,k}\Delta z_{k+1} + T_{i,j,k+1}\Delta z_k}{\Delta z_k + \Delta z_{k+1}} + \mathcal{O}(\delta^2) \quad (3.10)$$

where, $\delta = \frac{1}{2}(\Delta z_k + \Delta z_{k+1})$ is the distance between cells centers, and

$$T_{i,j,k} = \frac{\rho_{i,j,k} h_{i,j,k}}{f_{i,j,k}\rho_1 C_{p,1} + (1-f)\rho_2 C_{p,2}} \quad (3.11)$$

is the mixture temperature in the cell (i, j, k). This approximation is second order accurate when the grid is equidistant. The same approximation is used for variable grid size because, while only first order accurate, it is consistent with treatment of the continuity equation. Because it is usually associated with the centered difference schemes for convective terms further on it will be referred as the centered difference approximation (CD) of the temperature.

An other possibility is to use either $T_{i,j,k}$ or $T_{i,j,k+1}$ depending on the sign of the velocity $w_{i,j,k+\frac{1}{2}}$:

$$w_{i,j,k+\frac{1}{2}} T_{i,j,k+\frac{1}{2}} \simeq \frac{w_{i,j,k+\frac{1}{2}} + |w_{i,j,k+\frac{1}{2}}|}{2} T_{i,j,k} + \frac{w_{i,j,k+\frac{1}{2}} - |w_{i,j,k+\frac{1}{2}}|}{2} T_{i,j,k+1} + \mathcal{O}(\delta) \quad (3.12)$$

This approximation, also called upwind (UW) scheme, is only first order accurate. However, for problems with discontinuities it does not introduce new maxima or minima that were not already present in the solution avoiding the Gibbs phenomena associated with centered difference-type schemes.

For the face surface fraction $f^S_{i,j,k+\frac{1}{2}}$ one might try to compute these fractions using the interface reconstruction procedure in the staggered cells. This implies three new reconstruction steps, one for each space direction, which will increase the computational costs. An alternative way is to use the volume fractions $f_{i,j,k+\frac{1}{2}}$ instead, the same as it is done for the convective terms in the momentum equation. This solution, while simple and not expensive from computational point of view, generates numerical oscillations at the interface between the fluids (see Appendix B). The amplitude of this oscillations increases in time making the numerical scheme instable. Using smaller time steps reduces the amplification rate but it does not remove the instability[1]. This happens when either CD or UW scheme is used and no significant difference in the oscillations magnitude or growth rate have been observed. This phenomena is present also for the velocity but, in that case, no increase of the oscillations has been observed. This might be due to a balancing effect of the projection step which has the tendency to compensate the velocity fluctuations by a corresponding fluctuation of the pressure gradient.

To avoid such problems while keeping the computational costs at a reasonable level

[1] The oscillations are present and grow unbounded when a time step as small as 10^{-5} is used. For `TURBIT-VoF` code this value is considered to be the lowest value for which the results of the numerical simulation are not influenced by the numerical noise.

one can use the available interface reconstruction and compute, for each face of the cell, the corresponding surface fractions. For each face two surface fractions will be computed: $f^{+}_{i,j,k+\frac{1}{2}}$ corresponding to the cell (i,j,k) and $f^{-}_{i,j,k+\frac{1}{2}}$ for $(i,j,k+1)$ when the face $S_{i,j,k+\frac{1}{2}}$ is considered. From this two values one is selected depending on the sign of the velocity at that face:

$$f^{S}_{i,j,k+\frac{1}{2}} = \begin{cases} f^{+}_{i,j,k+\frac{1}{2}} & \text{if } w_{i,j,k+\frac{1}{2}} \geq 0 \\ f^{-}_{i,j,k+\frac{1}{2}} & \text{if } w_{i,j,k+\frac{1}{2}} < 0 \end{cases} \tag{3.13}$$

We call this an upwind procedure for the surface fractions. Using this approximation improves the results in the sense that the oscillation of the temperature field at the interface between the fluids are bounded when the CD scheme is used. A damping of this oscillation and a smoother solution can be obtained if the temperature at the cell faces are approximated using the UW scheme due to the numerical diffusion associated with the scheme.

Replacing (3.10) in (3.2) the CD numerical enthalpy convective term is approximated by

$$\begin{aligned}[\nabla \cdot \langle \rho h \vec{\mathbf{v}} \rangle]_{i,j,k} \simeq \frac{1}{\Delta z_k} \Bigg[& (\rho C_p)_{i,j,k+\frac{1}{2}} w_{i,j,k+\frac{1}{2}} \frac{T_{i,j,k}\Delta z_{k+1} + T_{i,j,k+1}\Delta z_k}{\Delta z_k + \Delta z_{k+1}} \\ & - (\rho C_p)_{i,j,k-\frac{1}{2}} w_{i,j,k-\frac{1}{2}} \frac{T_{i,j,k}\Delta z_{k-1} + T_{i,j,k-1}\Delta z_k}{\Delta z_k + \Delta z_{k-1}} \Bigg] \\ & + TCD_x + TCD_y \end{aligned} \tag{3.14}$$

where, TCD_x and TCD_y are the numerical approximations of the convective fluxes in x and y, respectively. The formula for UW approximation of the convective term is

$$\begin{aligned}[\nabla \cdot \langle \rho h \vec{\mathbf{v}} \rangle]_{i,j,k} \simeq \frac{1}{\Delta z_k} \Bigg[& (\rho C_p)_{i,j,k+\frac{1}{2}} \left(\frac{w_{i,j,k+\frac{1}{2}} + |w_{i,j,k+\frac{1}{2}}|}{2} T_{i,j,k} + \frac{w_{i,j,k+\frac{1}{2}} - |w_{i,j,k+\frac{1}{2}}|}{2} T_{i,j,k+1} \right) \\ & - (\rho C_p)_{i,j,k-\frac{1}{2}} \left(\frac{w_{i,j,k-\frac{1}{2}} - |w_{i,j,k-\frac{1}{2}}|}{2} T_{i,j,k} + \frac{w_{i,j,k-\frac{1}{2}} + |w_{i,j,k-\frac{1}{2}}|}{2} T_{i,j,k-1} \right) \Bigg] \\ & + TUW_x + TUW_y \end{aligned} \tag{3.15}$$

where, TUW_x and TUW_y are the corresponding terms in $x-$ and, respectively $y-$direction.

In `TURBIT-VoF` both methods are implemented. While the first one (CD) has the

advantage that is a second order scheme and gives better results in the bulk region of each fluid, the second one (UW) avoids the oscillations of the temperature at the interface between the fluids.

3.1.2 Conductive term approximation

For the conductive term in (3.1) we use the same approximation strategy. First, we write this term as the sum of the heat fluxes through the cell faces:

$$-\frac{1}{\mathtt{Pe}}\left[\nabla\cdot\langle\vec{\mathsf{q}}\rangle\right]_{i,j,k}=-\frac{1}{\mathtt{Pe}}\sum_{\ell}\frac{S_\ell}{V_{i,j,k}}\frac{1}{S_\ell}\int\limits_{S_\ell}\vec{\mathsf{q}}\cdot\vec{\mathsf{n}}\,dS$$

where, S_ℓ are the faces of the control volume. Using the Fourier law for heat flux one has:

$$-\frac{1}{\mathtt{Pe}}\left[\nabla\cdot\langle\vec{\mathsf{q}}\rangle\right]_{i,j,k}=\frac{1}{\mathtt{Pe}}\sum_{\ell}\frac{S_\ell}{V_{i,j,k}}\frac{1}{S_\ell}\int\limits_{S_\ell}\lambda\left.\frac{\partial T}{\partial n}\right|_\ell dS \tag{3.16}$$

For the face $S_{i,j,k+\frac{1}{2}}$ the corresponding term from the sum can be written as:

$$\frac{1}{S_{i,j,k+\frac{1}{2}}}\int\limits_{S_{i,j,k+\frac{1}{2}}}\lambda\frac{\partial T}{\partial z}\,dS=f^S_{i,j,k+\frac{1}{2}}\lambda_1\int\limits_{S^1_{i,j,k+\frac{1}{2}}}\frac{\partial T}{\partial z}\,dS+(1-f^S_{i,j,k+\frac{1}{2}})\lambda_2\int\limits_{S^2_{i,j,k+\frac{1}{2}}}\frac{\partial T}{\partial z}\,dS \tag{3.17}$$

Computing the mixture (equivalent) thermal conductivity as

$$\lambda^S_{i,j,k+\frac{1}{2}}=f^S_{i,j,k+\frac{1}{2}}\lambda_1+(1-f^S_{i,j,k+\frac{1}{2}})\lambda_2$$

and approximating the temperature derivative using the values at the center of the two neighboring cells seems to be the straightforward procedure to compute the heat flux over the face $S_{i,j,k+\frac{1}{2}}$. This simple approach leads to rather incorrect implications in some cases and can not handle the abrupt changes of conductivity at the interface as it was proved by Patankar [35]. The main point in developing the alternative to this approximation is that not the local value of conductivity at the face concerns us primarily but rather to obtain a good representation of the heat flux across the volume.

Let us consider that two neighboring cells one having the center in P and the other one in N are filled with two different fluids with thermal conductivities λ_P, λ_N (see Fig. 3.1).

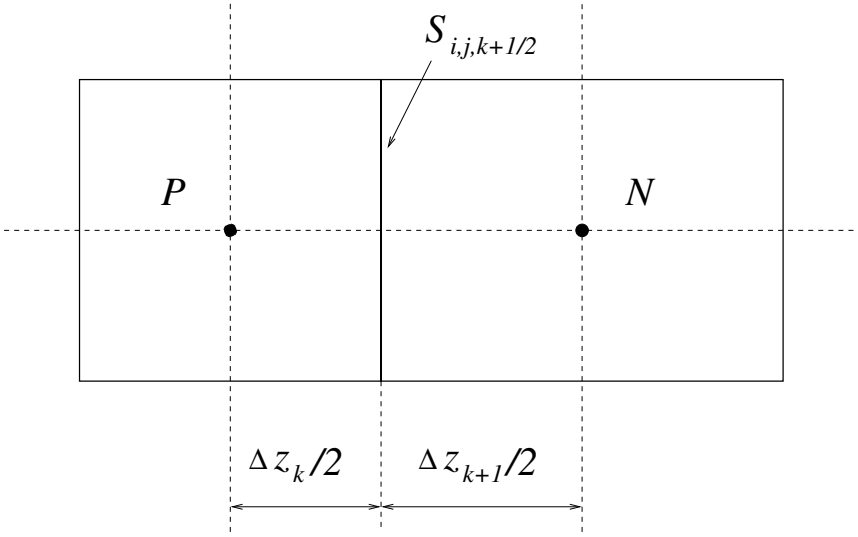

Fig. 3.1: Distances associated with the face $S_{i,j,k+\frac{1}{2}}$

The interface separating the two fluids is supposed to be rigid and without any thermal resistance. A steady one-dimensional analysis (without sources) leads to:

$$\mathsf{q}_{i,j,k+\frac{1}{2}} = \frac{T_P - T_N}{\dfrac{\Delta z_k}{2\lambda_P} + \dfrac{\Delta z_{k+1}}{2\lambda_N}} \tag{3.18}$$

Introducing the *effective* heat conductivity for the face $S_{i,j,k+\frac{1}{2}}$ as

$$\lambda_{i,j,k+\frac{1}{2}} = \frac{\Delta z_k + \Delta z_{k+1}}{\dfrac{\Delta z_k}{\lambda_P} + \dfrac{\Delta z_{k+1}}{\lambda_N}} \tag{3.19}$$

the heat flux through this surface can be written in a form similar to the single phase case as:

$$\mathsf{q}_{i,j,k+\frac{1}{2}} = \lambda_{i,j,k+\frac{1}{2}} \frac{T_P - T_N}{z_N - z_P} \tag{3.20}$$

In our simple example the grid fits the interface, i.e. all the cells are single phase cells. This is usually the case when a moving mesh method is used. For the VOF methods, near the interface the computational cell usually contain both fluids. However, the enthalpy (temperature) in each cell is defined as the mixture enthalpy (temperature) therefore we can treat each cell as it is filled with a single fluid with the same properties as the mixture. The heat flux at the face between two cells is then computed using (3.20).

To summarize, the procedure to compute the heat flux at a face between two cells P and N is:

- First, the mixture heat conductivities corresponding to each cell are computed:

$$\lambda_P = f_P\lambda_1 + (1 - f_P)\lambda_2 \tag{3.21}$$
$$\lambda_N = f_N\lambda_1 + (1 - f_N)\lambda_2 \tag{3.22}$$

- Then, the temperature corresponding to each cell is obtained from the mixture enthalpy;
- Finally, the heat flux is computed using (3.20).

3.1.3 Time integration and time-step criteria

To approximate numerically the time derivative in (3.1) we use a third order Runge-Kutta scheme, the same that it is used for the integration of the momentum equation (see [38]). Thus, if $h^n_{i,j,k}$ is the value of the enthalpy of the cell (i, j, k) at time-step n, the value at next time-step $n + 1$ corresponding to the same cell is computed as follows:

$$\begin{aligned}
\rho^{n+1}_{i,j,k}h^{(1)}_{i,j,k} &= (\rho h)^n_{i,j,k} + \Delta t\mathcal{L}(\rho^n, \vec{\mathsf{v}}^n, h^n) \\
\rho^{n+1}_{i,j,k}h^{(2)}_{i,j,k} &= \frac{3}{4}(\rho h)^n_{i,j,k} + \frac{1}{4}\rho^{(n+1)}_{i,j,k}h^{(1)}_{i,j,k} + \frac{1}{4}\Delta t\mathcal{L}(\rho^{n+1}, \vec{\mathsf{v}}^{n+1}, h^{(1)}) \\
\rho^{n+1}_{i,j,k}h^{n+1}_{i,j,k} &= \frac{1}{3}(\rho h)^n_{i,j,k} + \frac{2}{3}\rho^{(n+1)}_{i,j,k}h^{(2)}_{i,j,k} + \frac{2}{3}\Delta t\mathcal{L}(\rho^{n+1}, \vec{\mathsf{v}}^{n+1}, h^{(2)})
\end{aligned} \tag{3.23}$$

where $h^{(1)}_{i,j,k}$ and $h^{(2)}_{i,j,k}$ are intermediate values of the enthalpy, Δt is the integration time-step

$$\Delta t = t^{n+1} - t^n$$

and $\mathcal{L}$ is the numerical approximation of the convective and conductive heat fluxes:

$$\mathcal{L} = -\left[\nabla \cdot \langle \rho h\vec{\mathsf{v}}\rangle\right]_{i,j,k} - \frac{1}{\mathsf{Pe}}\left[\nabla \cdot \langle \vec{\mathsf{q}}\rangle\right]_{i,j,k}$$

which has been described in previous two sections. This method belongs to the class of TVD (total variation diminishing) high order Runge-Kutta methods developed in [46] and further in [12].

To find the restriction for the time step Δt let us assume that a first order Euler forward time stepping is used:

$$\phi^{n+1} = \phi^n + \Delta t \mathcal{L}(\phi^n) \tag{3.24}$$

where, $\phi = \rho h$. This time discretization is stable in a certain norm if

$$\| \phi^{n+1} \| \leq \| \phi^n \| \tag{3.25}$$

under a suitable restriction on the time step:

$$\Delta t \leq \Delta t_0 \tag{3.26}$$

In the case of higher order Runge-Kutta methods, in order to satisfy the same stability condition (3.25), the time step has to satisfy the following restriction:

$$\Delta t \leq c \Delta t_0 \tag{3.27}$$

where c is termed *the CFL coefficient* for the high order time discretization and depends on the coefficients in the Runge-Kutta scheme. For (3.23) it has been demonstrated [46] that

$$c = 1$$

This means that TVD high order time discretization defined above maintains the stability, in whatever norm, of the Euler forward first order time stepping. For a multi-dimensional scalar equation like the energy equation (3.1) the maximum norm stability should be used [12, 45].

If the convective term is approximated using CD scheme (3.14) the equation (3.24) can be written as

$$\begin{aligned} \phi^{n+1}_{i,j,k} - \phi^n_{i,j,k} = \Delta t(A_{i+1,j,k}\phi^n_{i+1,j,k} + A^n_{i,j+1,k}\phi^n_{i,j+1,k} + A_{i,j,k+1}\phi^n_{i,j,k+1}) \\ - \Delta t A_{i,j,k}\phi^n_{i,j,k} \\ + \Delta t(A_{i-1,j,k}\phi^n_{i-1,j,k} + A^n_{i,j-1,k}\phi^n_{i,j-1,k} + A_{i,j,k+1}\phi^n_{i,j,k-1}) \end{aligned} \tag{3.28}$$

where,

$$A_{i,j,k+1} = -\frac{1}{2\Delta z}\frac{(\rho C_p)^n_{i,j,k+\frac{1}{2}}}{(\rho C_p)^n_{i,j,k+1}} w^n_{i,j,k+\frac{1}{2}} + \frac{1}{\mathtt{Pe}}\frac{1}{\Delta z^2}\frac{\lambda^n_{i,j,k+\frac{1}{2}}}{(\rho C_p)^n_{i,j,k+1}}$$

$$\begin{aligned} A_{i,j,k} =& \frac{1}{2\Delta x}\frac{(\rho C_p)^n_{i+\frac{1}{2},j,k}u^n_{i+\frac{1}{2},j,k} - (\rho C_p)^n_{i-\frac{1}{2},j,k}u^n_{i-\frac{1}{2},j,k}}{(\rho C_p)^n_{i,j,k}} + \frac{1}{\mathtt{Pe}}\frac{1}{\Delta x^2}\frac{\lambda^n_{i+\frac{1}{2},j,k} + \lambda^n_{i-\frac{1}{2},j,k}}{(\rho C_p)^n_{i,j,k}} \\ &+ \frac{1}{2\Delta y}\frac{(\rho C_p)^n_{i,j+\frac{1}{2},k}v^n_{i,j+\frac{1}{2},k} - (\rho C_p)^n_{i,j-\frac{1}{2},k}v^n_{i,j-\frac{1}{2},k}}{(\rho C_p)^n_{i,j,k}} + \frac{1}{\mathtt{Pe}}\frac{1}{\Delta y^2}\frac{\lambda^n_{i,j+\frac{1}{2},k} + \lambda^n_{i,j-\frac{1}{2},k}}{(\rho C_p)^n_{i,j,k}} \\ &+ \frac{1}{2\Delta z}\frac{(\rho C_p)^n_{i,j,k+\frac{1}{2}}w^n_{i,j,k+\frac{1}{2}} - (\rho C_p)^n_{i,j,k-\frac{1}{2}}w^n_{i,j,k-\frac{1}{2}}}{(\rho C_p)^n_{i,j,k}} + \frac{1}{\mathtt{Pe}}\frac{1}{\Delta z^2}\frac{\lambda^n_{i,j,k+\frac{1}{2}} + \lambda^n_{i,j,k-\frac{1}{2}}}{(\rho C_p)^n_{i,j,k}} \end{aligned}$$

$$A_{i,j,k-1} = \frac{1}{2\Delta z}\frac{(\rho C_p)^n_{i,j,k-\frac{1}{2}}}{(\rho C_p)^n_{i,j,k-1}} w^n_{i,j,k-\frac{1}{2}} + \frac{1}{\mathtt{Pe}}\frac{1}{\Delta z^2}\frac{\lambda^n_{i,j,k-\frac{1}{2}}}{(\rho C_p)^n_{i,j,k-1}}$$

The coefficients for $\phi^n_{i,j\pm1,k}$ and $\phi^n_{i,j,k\pm1}$ have similar expressions and can be obtained modifying the indices accordingly. For simplicity, in the formula above we have assumed that the grid is uniform in each directions. To find Δt_0 one can use a Von Neumann analysis for (3.24) and enforce the stability condition (3.25). However, this procedure is rather complicated and requires to compute the eigenvalues of an amplification matrix that is constructed using the coefficients above. From a practical point of view we need a simple relation to define the maximum time step. For this we use the *positive coefficients rule* introduced by Patankar [35] which states that in (3.28) all the coefficients of the terms corresponding to the same time step should have the same sign. Assuming that the velocities are all positive one has

$$1 - \Delta t A_{i,j,k} \geq 0 \tag{3.29}$$

$$\frac{1}{\mathtt{Pe}}\frac{1}{\Delta z^2}\frac{\lambda^n_{i,j,k+\frac{1}{2}}}{(\rho C_p)^n_{i,j,k+1}} \geq \frac{1}{2\Delta z}\frac{(\rho C_p)^n_{i,j,k+\frac{1}{2}}}{(\rho C_p)^n_{i,j,k+1}} w^n_{i,j,k+\frac{1}{2}} \tag{3.30}$$

and two other inequalities similar to (3.30) corresponding to $x-$ and $y-$directions. The second inequality (3.30) expresses a restriction on the numerical scheme itself, that is, it defines the maximum Peclet number that can be simulated when the convective flux is approximated using the CD scheme (3.14) and the heat conduction is computed using

(3.20):

$$\mathtt{Pe} \leq 2\frac{\lambda^n_{i,j,k+\frac{1}{2}}}{(\rho C_p)^n_{i,j,k+\frac{1}{2}} w^n_{i,j,k+\frac{1}{2}} \Delta z} \tag{3.31}$$

Assuming that fluids properties are constant we retrieve the restriction found by Patankar [35] for a convection-diffusion single-phase flow.

The first condition (3.29) expresses a *CFL-like condition* and defines the time step limit as:

$$\Delta t \leq \min_{i,j,k} \frac{1}{\mid A_{i,j,k} \mid} \tag{3.32}$$

As for the previous condition, if one assumes constant fluid properties and using the discrete continuity equation for incompressible flows, the time step restriction for a diffusion equation is retrieved:

$$\Delta t \leq \mathtt{Pe}\frac{\rho C_p \Delta^2}{6\lambda}$$

where, the grid is supposed to have uniform mesh size (Δ) in all three spatial directions.

When the convective heat fluxes are approximated using the UW scheme the same procedure to determine the time step restriction applies and a condition similar to (3.32) is obtained. The factor $A_{i,j,k}$, when UW is used, has the following contribution corresponding to $z-$direction:

$$\frac{1}{2\Delta z}\frac{(\rho C_p)^n_{i,j,k+\frac{1}{2}}(w^n_{i,j,k+\frac{1}{2}} + |w^n_{i,j,k+\frac{1}{2}}|) - (\rho C_p)^n_{i,j,k-\frac{1}{2}}(w^n_{i,j,k-\frac{1}{2}} - |w^n_{i,j,k-\frac{1}{2}}|)}{(\rho C_p)^n_{i,j,k}} + \frac{1}{\mathtt{Pe}}\frac{1}{\Delta z^2}\frac{\lambda^n_{i,j,k+\frac{1}{2}} + \lambda^n_{i,j,k-\frac{1}{2}}}{(\rho C_p)^n_{i,j,k}}$$

The main difference between the two cases is that, for UW scheme, there is no restriction for the Pe number. This is a consequence of the fact that, when the velocity is positive the term

$$A_{i,j,k+\frac{1}{2}} = -\frac{1}{2\Delta z}\frac{(\rho C_p)^n_{i,j,k+\frac{1}{2}}(w^n_{i,j,k+\frac{1}{2}} - |w^n_{i,j,k+\frac{1}{2}}|)}{(\rho C_p)^n_{i,j,k}} + \frac{1}{\mathtt{Pe}}\frac{1}{\Delta z^2}\frac{\lambda^n_{i,j,k+\frac{1}{2}}}{(\rho C_p)^n_{i,j,k}} = \frac{1}{\mathtt{Pe}}\frac{1}{\Delta z^2}\frac{\lambda^n_{i,j,k+\frac{1}{2}}}{(\rho C_p)^n_{i,j,k}}$$

does not depend on the velocity field and is always positive.

For our simulations, since we do not know a priori the local velocities and phase distri-

bution, we consider the initial time step as

$$\Delta t_0 = \texttt{CDTKOR} \cdot \min\left(\texttt{Pe}\frac{(\rho C_p)_1 \Delta^2}{6\lambda_1}, \texttt{Pe}\frac{(\rho C_p)_2 \Delta^2}{6\lambda_2}\right) \tag{3.33}$$

where, CDTKOR is a safety factor. In our simulations $\texttt{CDTKOR} = 0.8$.

3.2 Verification for single-phase flow

To verify the validity of the numerical approximations introduced in section (3.1.1) and (3.1.2) simulations are performed for a fully developed flow with heat transfer in a rectangular channel and for natural convection in a rectangular 2D box with heated vertical walls. In this section all the simulations were done for single phase flows considering fluids with different properties. The two-phase results will be presented in the next chapter.

3.2.1 Flow in a channel with rectangular cross-section

To verify the numerical approximation of the convective terms we simulate the flow of a fluid along a horizontal straight channel with rectangular cross-section. The fluid properties are assumed to be constant along the channel and do not vary with the temperature. Also, the hight of the channel is assumed to be small and, therefore, the gravitational effects can be neglected. In Fig. 3.2 the channel geometry and the orientation of the coordinates system

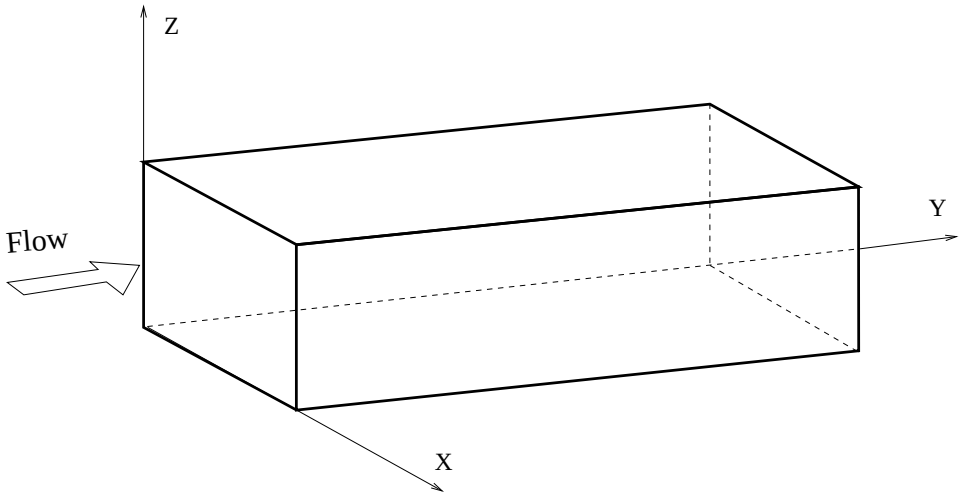

Fig. 3.2: Channel geometry and coordinate system. The channel has walls in x- and z-direction, while the fluid flows in positive y-direction.

is presented. The channel has walls in x- and z-direction and let L_x and, respectively L_z, be the distance between the walls. The fluid flows in y-direction. The length of the channel is L. This length is related to the characteristic length of the flow in stream-wise direction.

Hydrodynamic considerations

For a single phase flow in a channel with constant cross-section the flow is said to be *fully developed* if the velocity cross-section profile does not change in stream-wise direction:

$$\frac{\partial \vec{\mathtt{v}}}{\partial y} = 0. \tag{3.34}$$

A direct consequence of (3.34) is that the cross-section averaged pressure has a linear variation in stream-wise direction:

$$\frac{d}{dy}\int_0^{L_x}\int_0^{L_z} p\; dxdz = \int_0^{L_z}\left(\mu\left.\frac{\partial v}{\partial x}\right|_{L_x,z} - \mu\left.\frac{\partial v}{\partial x}\right|_{0,z}\right) dz + \int_0^{L_x}\left(\mu\left.\frac{\partial v}{\partial z}\right|_{x,L_z} - \mu\left.\frac{\partial v}{\partial z}\right|_{x,0}\right) dx = \beta \tag{3.35}$$

where, β is the pressure drop, and is a constant of the flow. Let us define the reduced pressure field as:

$$P(x,z) = p(x,y,z) - \beta y \tag{3.36}$$

which is uniform in stream-wise direction.

For fully developed laminar flows $u = w = 0$ and the reduced pressure is constant in every cross-section ($P = 0$). The velocity profile can be determined exactly using an analogy with the stress function of the theory of elasticity [32]:

$$v(x,z) = \frac{4}{\pi^3}(-\beta)\,\mathtt{Re}\frac{1}{\alpha^2}\sum_{n=1,3,\ldots}^{\infty}\frac{(-1)^{(n-1)/2}}{n^3}\left(1 - \frac{\cosh(n\pi(z-0.5)\alpha)}{\cosh(\frac{n\pi}{2}\alpha)}\right)\cos(n\pi(x-0.5)\alpha) \tag{3.37}$$

where $\alpha = L_z/L_x$ is the channel aspect ratio. The relation (3.37) is written in dimensionless form, with mean velocity (v_m) as reference velocity

$$v_m = \frac{1}{\rho L_x L_z}\int_0^{L_x}\int_0^{L_z} \rho v\; dxdz \tag{3.38}$$

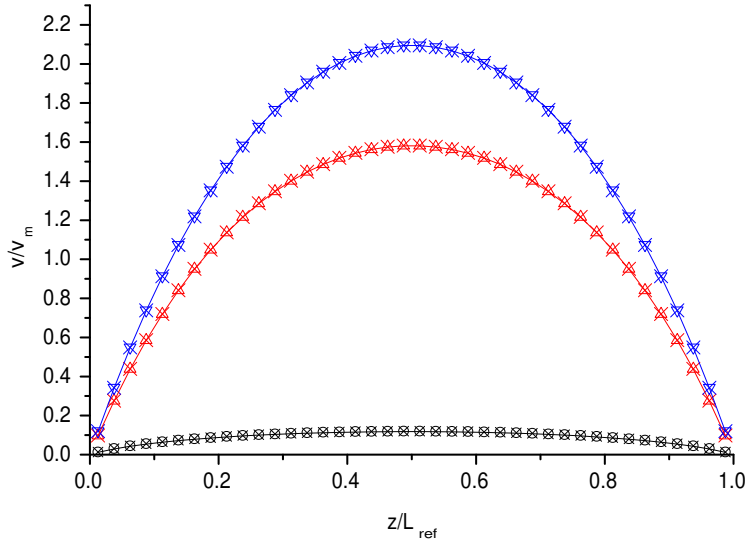

Fig. 3.3: Velocity profiles for square channel for three cross-section positions: z = 0.0125 (circle), 0.2375 (triangle-up), 0.4875 (triangle-down); the computed values are shown as symbols while the continuous lines are the exact solution.

while the distance between the walls in z-direction is chosen as reference length ($L_z = 1$). The pressure gradient β is given in terms of mean velocity (v_m) by

$$v_m = 1 = \frac{1}{12}(-\beta)\,\mathtt{Re}\frac{1}{\alpha^2}\left[1 - \frac{192}{\pi^5}\frac{1}{\alpha}\sum_{n=1,3,\ldots}^{\infty}\frac{1}{n^5}\tanh\left(\frac{n\pi}{2}\alpha\right)\right] \tag{3.39}$$

In Fig. 3.4 and 3.3 we present the comparison between computed velocity profiles and the exact solution. The computations have been performed for two channel geometries: a rectangular channel with an aspect ratio $\alpha = 0.5$ and a square channel ($\alpha = 1$). The mesh grid used to discretize the domain has 80×40 cells per cross-section for the rectangular channel and 40×40 for the square one. In stream-wise direction the channel has the same length as its width in z-direction in both cases. Near the wall, the computed velocity is larger than the exact solution with $\varepsilon \approx 13\%$ in the cells at the corners of the channel and is only $\varepsilon \approx 2\%$ larger at midpoints of each side. Away from the wall the error is smaller then 1%. All the simulations were done for $\mathtt{Re} = 100$.

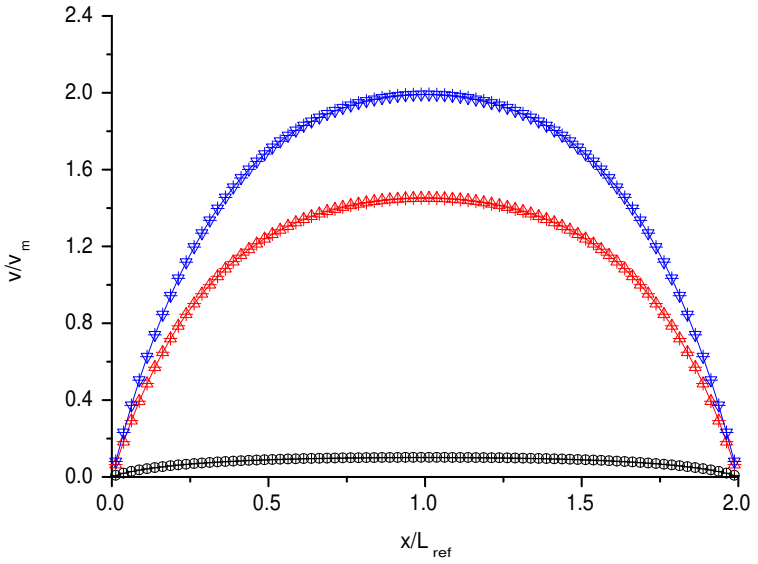

(a)

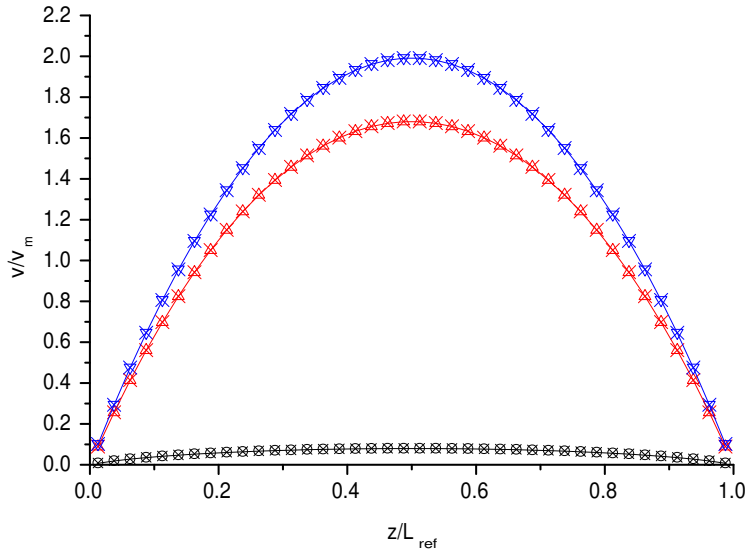

(b)

Fig. 3.4: Velocity profiles for rectangular channel: (a) x-profiles: x = 0.0125 (circle), 0.4875 (triangle-up), 0.9875 (triangle-down); (b) z-profiles: z = 0.0125 (circle), 0.2375 (triangle-up), 0.4875 (triangle-down) ; the computed values are shown as symbols while the continuous lines are the exact solution.

Thermally developed single phase flow

The existence of convection heat transfer between the walls and the fluid dictates that the fluid temperature is changing in stream-wise direction. This means that one can not use directly the same approach as for the hydrodynamic case; instead of using the temperature field one can characterize such kind of flows using the *internal heat transfer coefficient*[2]:

$$\mathsf{h} = q/(T_w - T_m) \tag{3.40}$$

where, q is the local wall heat flux, T_w is the local wall temperature and

$$T_m = \frac{1}{L_x L_z \rho v_m C_p} \int_0^{L_x} \int_0^{L_z} \rho v C_p T \, dxdz \tag{3.41}$$

is the *mixed mean fluid temperature* (also referred to as mass-averaged temperature, bulk fluid temperature, or mixing-cup temperature).

The flow is called thermally developed if the heat transfer coefficient is independent of the stream-wise coordinate. There are four types of thermal boundary conditions that are compatible with the existence of a thermally developed regime [47]:

(a) axial uniform wall temperature[3], T_w = constant;

(b) axial uniform wall heat flux[4], q = constant;

(c) exponential variation of the wall heat flux $q = \exp(\alpha y)$;

(d) convective heat transfer from external surface of the duct to a fluid environment with heat transfer coefficient h_e and temperature T_∞, both of which are uniform.

It has been proved [47] that (a), (b) and (d) boundary conditions are, in fact, special case of (d) and can be treated in a similar manner. We will consider here only the case of axial uniform heat flux.

[2] It is also called *convective conductance*.

[3] Constant surface temperature occurs in applications such as evaporators, condensers, and, in fact, any heat exchanger where one fluid has a very much higher capacity rate than the other (capacity rate = product of mass flow rate and specific heat of fluid).

[4] Constant heat rate problems arise in a number of situations: electric resistance heating, radiant heating, nuclear heating, and in counterflow heat exchangers when the fluid capacity rates are the same.

The usual way to describe a thermally developed flow is to define a dimensionless temperature difference:

$$\vartheta(x,y,z) = \frac{T(x,y,z) - T_{ref}(y)}{T_m(y) - T_{ref}(y)} \tag{3.42}$$

which for thermally developed flows is constant in stream-wise direction:

$$\frac{\partial \vartheta}{\partial y} = 0 \tag{3.43}$$

While the definition (3.42) is simple, the difficulty is choosing the reference temperature T_{ref}. For problems with uniform or perimetrical uniform wall temperature condition the wall temperature is taken as T_{ref}. When the wall temperature is not constant, a perimetrical averaged temperature is used.

However, for axially uniform wall heat flux an alternate method is available. For such cases the thermally developed regime is characterized by $\partial T/\partial y = \theta =$ constant [36]. Thus, the temperature field can be subdivided into two components:

$$T(x,y,z) = \theta y + \Theta(x,z) \tag{3.44}$$

where, the reduced temperature field Θ is uniform in stream-wise direction. It can be easily shown that

$$\theta = \frac{1}{\mathtt{Pe}} \frac{Q}{C_p \dot{m}} \tag{3.45}$$

where, $\dot{m}$ is the mass flow rate

$$\dot{m} = \frac{1}{L_x L_z} \int_0^{L_x} \int_0^{L_z} \rho v \; dxdz \tag{3.46}$$

and Q is the rate of heat addition:

$$Q = \frac{1}{L_x L_z} \left[\int_0^{L_z} \left(\lambda \left. \frac{\partial T}{\partial x} \right|_{x=L_x} - \lambda \left. \frac{\partial T}{\partial x} \right|_{x=0} \right) dz + \int_0^{L_x} \left(\lambda \left. \frac{\partial T}{\partial z} \right|_{z=L_z} - \lambda \left. \frac{\partial T}{\partial z} \right|_{z=0} \right) dx. \right] \tag{3.47}$$

Both, the mass flow rate and the rate of heat addition are constants of the flow and, thus, θ is also constant.

This new formulation has the advantage that the reference temperature can be chosen

independently of the perimetric variation of the wall temperature. Also, this method can be easily extended to stream-wise periodic wall heat fluxes or two-phase flows.

Replacing (3.44) in (2.36c) and assuming that the control volume V is vanishing small, one has:

$$\frac{\partial \rho C_p \Theta}{\partial t} + \nabla \cdot (\rho C_p \Theta \vec{\mathsf{v}}) + \rho C_p \theta v = -\frac{1}{\mathtt{Pe}} \nabla \cdot \vec{\mathsf{q}} + \frac{\ell^* r^*}{h^* v^*} \rho r \tag{3.48}$$

where, v is the stream-wise velocity component. Note that the influence of the wall heating along the channel on the local reduced temperature profile is given by the supplemental term $\rho C_p \theta v$ which is a source term. Since it does not depend on Θ the same numerical approximation as for (3.1) applies.

For convective heat transfer in rectangular channels there are no analytical solutions for the temperature profile. To characterize the heat transfer, in technical applications, the ratio of the convective conductance h and the molecular thermal conductance λ/D_h (D_h is the hydraulic diameter), i.e. the Nusselt number ($\mathtt{Nu}$), is used:

$$\mathtt{Nu} = \frac{D_h Q}{\dfrac{\lambda}{C_p}(h_{w,m} - h_m)} \tag{3.49}$$

where, h_m is the fluid bulk enthalpy and $h_{w,m}$ is the peripheral mean fluid enthalpy at the wall

$$h_{w,m} = \frac{1}{2(L_x + L_z)} \left(\int_0^{L_x} (h(x, y, 0) + h(x, y, L_z)\, dx + \int_0^{L_z} (h(0, y, z) + h(L_x, y, z))\, dz \right) \tag{3.50}$$

In Table 3.1 we compare the $\mathtt{Nu}$ number computed using `TURBIT-VoF` numerical code and the values reported in [44]. The computations have been done for air ($\mathtt{Pr} = 0.71$) for two types of cross-sections: a square (aspect ratio $\alpha = L_z/L_x = 1$) and a rectangular cross-section ($\alpha = 0.5$). In both cases, two grids have been used: a coarse one with the mesh cell width $\Delta = L_z/20$ and one with $\Delta = L_z/40$. An other computation has been performed using water ($\mathtt{Pr} = 7$) instead of air to verify the code behavior for larger Pr numbers. This computation has been done only for the square channel and the finer grid. For all the simulations uniform wall heat flux is considered, both in stream-wise direction

	$\alpha = 1$			$\alpha = 0.5$		
mesh cell	Nu	$T^*_{w,max}$	$T^*_{w,min}$	Nu	$T^*_{w,max}$	$T^*_{w,min}$
air Pr = 0.71						
1/20	3.11	1.3546	0.77	3.0323	1.4716	0.4992
1/40	3.0928	1.376	0.769	3.0224	1.4868	0.4992
water Pr = 7						
1/40	3.093	1.3767	0.7695	–	–	–
Shah and London [44]						
–	3.091	1.39	0.769	3.017	1.50	0.499

Tab. 3.1: Comparison for Nu, $T^*_{w,max}$ and $T^*_{w,min}$ between the values computed with TURBIT-VoF and those given by Shah and London [44] for two different aspect ratios and mesh sizes; uniform wall heat flux is considered, both in stream-wise direction and around the channel

and around the channel[5]. The error for the computed Nu number is smaller than 0.6 % for all the cases that have been considered. The largest error corresponds to the case when the fluid was air and the coarse grid has been used. For the finer grid the error decreases to 0.06 %. The wall temperature distribution around the duct periphery is not uniform and a normalized maximum and minimum wall temperatures are define as follows [44]:

$$T^*_{w,max} = \frac{T_{w,max} - T_c}{T_{w,m} - T_c} \tag{3.51a}$$

$$T^*_{w,min} = \frac{T_{w,min} - T_c}{T_{w,m} - T_c} \tag{3.51b}$$

where T_c is the fluid temperature at the duct centerline. The maximum temperature occurs at the corners and the minimum temperature occurs on the midpoint of the long side. They give useful information for the proper design of the hot and cold regions of the duct. The computed values for this normalized temperatures are also given in Table 3.1. When compared with the values reported in the literature the error of the computed $T^*_{w,min}$ is smaller than 0.1%, while for $T^*_{w,max}$ the largest error is 2.5%.

3.2.2 Natural convection

In the previous section we considered a case for which the convective effects dominate the fluid flow and the flow was stationary. To verify the numerical scheme for a situation when

[5] In [44] they are identified as H2 boundary conditions.

the heat conduction is more important and the flow is time-dependent we simulate the natural convection in a 2D box with heated vertical walls. The fluid density is assumed to be constant in the unsteady and convective terms, and is treated as temperature-dependent only in the buoyancy term. This is called the *Boussinesq approximation*. One usually assumes that the density varies linearly with temperature:

$$(\rho - \rho^0)g = -\rho^0 g\beta(T - T^0) \tag{3.52}$$

where, β is the coefficient of volumetric expansion and ρ^0 is the density value at the reference temperature T^0. This approximation introduces errors of order of 1% if the temperature differences are below e.g. 2° for water and 15° for air [8, 13].

Since the density in the gravitational term is no longer constant one has to redefine the reduced pressure (2.37) by replacing ρ_1 with its value at the reference temperature:

$$P_m = p_m - \frac{1}{\mathtt{Fr}}\frac{\rho_1^0}{\rho^*}\frac{\vec{\mathtt{g}}}{g}\cdot\vec{\mathtt{x}} \tag{3.53}$$

The buoyancy term in (2.36b) becomes then

$$-(1-f)\frac{\mathtt{Eo}}{\mathtt{We}}\frac{\vec{\mathtt{g}}}{g} = \frac{1}{\rho^*(\mathtt{v}^*)^2}\left[f(\rho_1-\rho_1^0)g + (1-f)(\rho_2-\rho_2^0)g\right]\frac{\vec{\mathtt{g}}}{g} - (1-f)\frac{(\rho_1^0-\rho_2^0)g}{\rho^*(\mathtt{v}^*)^2}\frac{\vec{\mathtt{g}}}{g} \tag{3.54}$$

Using the Boussinesq approximation for each phase the formula above becomes:

$$-(1-f)\frac{\mathtt{Eo}}{\mathtt{We}}\frac{\vec{\mathtt{g}}}{g} = -\frac{\mathtt{Gr}}{\mathtt{Re}^2}\left[f\frac{\rho_1^0}{\rho^*}\frac{\beta_1}{\beta^*} + (1-f)\frac{\rho_2^0}{\rho^*}\frac{\beta_2}{\beta^*}\right]\frac{T-T^0}{\Delta T^*}\frac{\vec{\mathtt{g}}}{g} - (1-f)\frac{\mathtt{Eo}^0}{\mathtt{We}}\frac{\vec{\mathtt{g}}}{g} \tag{3.55}$$

where

$$\mathtt{Gr} = \frac{\mathtt{Ra}}{\mathtt{Pr}} \qquad \text{is the Grashof number} \tag{3.56}$$

$$\mathtt{Ra} = g\beta^*\Delta T^*(\ell^*)^3\frac{(\rho^*)^2 C_p^*}{\mu^*\lambda^*} \text{ is the Rayleigh number} \tag{3.57}$$

and ΔT^* is the characteristic temperature difference. For natural convection this is the difference between the temperature of the warm wall and the temperature of the cold wall.

Dimensionless temperature and temperature computation

The mixture enthalpy in an interface cell is:

$$h_m = \frac{1}{\rho_m}\left[f\rho_1 C_{p,1} T_1 + (1-f)\rho_2 C_{p,2} T_2\right] \tag{3.58}$$

Assuming that in the cell the phases are in thermal equilibrium $T_1 = T_2 = T_m$, the mixture temperature in the corresponding cell is:

$$T = T_m = \frac{\rho_m h_m}{\left[f\rho_1 C_{p,1} + (1-f)\rho_2 C_{p,2}\right]} \tag{3.59}$$

If one takes $C_p^* = C_{p,1}$ and $\rho^* = \rho_1$, then

$$\frac{T - T^0}{\Delta T^*} = \frac{\rho\left(\dfrac{h_m}{C_p^* T^0} - 1\right)}{\left[f + (1-f)\dfrac{\rho_2}{\rho_1}\dfrac{C_{p,2}}{C_{p,1}}\right]}\frac{T^0}{\Delta T^*} + \frac{(1-f)\dfrac{\rho_2}{\rho_1}\left(1 - \dfrac{C_{p,2}}{C_{p,1}}\right)}{\left[f + (1-f)\dfrac{\rho_2}{\rho_1}\dfrac{C_{p,2}}{C_{p,1}}\right]}\frac{T^0}{\Delta T^*}$$

where, $\rho = \rho_m/\rho^*$ is the dimensionless mean density. Further, if one chooses

$$h = \frac{h_m - C_p^* T^0}{C_p^* \Delta T^*}$$

as dimensionless enthalpy the dimensionless temperature is defined as:

$$\frac{T - T^0}{\Delta T^*} = \frac{\rho h}{\left[f + (1-f)\dfrac{\rho_2}{\rho_1}\dfrac{C_{p,2}}{C_{p,1}}\right]} + \frac{(1-f)\dfrac{\rho_2}{\rho_1}\left(1 - \dfrac{C_{p,2}}{C_{p,1}}\right)}{\left[f + (1-f)\dfrac{\rho_2}{\rho_1}\dfrac{C_{p,2}}{C_{p,1}}\right]}\frac{T^0}{\Delta T^*} \tag{3.60}$$

Now, let us see how this can be used to evaluate the buoyancy terms in the momentum equation when a projection method is used to enforce the divergence-free condition. Since a staggered grid is used for each velocity component a different control volume is used. This means that for each velocity component the buoyancy term from (3.55) has to be evaluated in a different control volume. Let us consider the case of the z-direction velocity

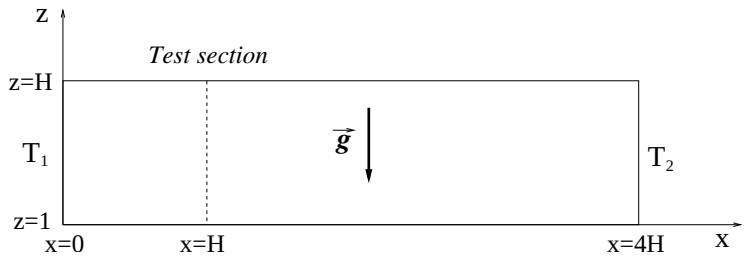

Fig. 3.5: Geometry of the benchmark problem; at $z = 1$ and $z = H$ one has adiabatic walls.

component corresponding to the cell (i, j, k). The corresponding buoyancy term is:

$$-\frac{\mathtt{Gr}}{\mathtt{Re}^2}\left[f_{i,j,k+\frac{1}{2}}\frac{\rho_1^0}{\rho^*}\frac{\beta_1}{\beta^*}+(1-f_{i,j,k+\frac{1}{2}})\frac{\rho_2^0}{\rho^*}\frac{\beta_2}{\beta^*}\right]\frac{T_{i,j,k+\frac{1}{2}}-T^0}{\Delta T^*}\frac{\vec{\mathtt{g}}}{g}+(1-f_{i,j,k+\frac{1}{2}})\frac{\mathtt{Eo}}{\mathtt{We}}\frac{\vec{\mathtt{g}}}{g} \tag{3.61}$$

where, $T_{i,j,k+\frac{1}{2}}$ is the temperature corresponding to the staggered cell $(i, j, k+\frac{1}{2})$. Since the enthalpy is computed for the centered cells one has to approximate the temperature value for the staggered cells. To do this one can use the temperature values $T_{i,j,k}$ and $T_{i,j,k+1}$ computed using (3.59). If we consider a linear variation of the temperature field between the two cells, the temperature value corresponding to the staggered cell is:

$$T_{i,j,k+\frac{1}{2}}=\frac{T_{i,j,k}\Delta z_{k+1}+T_{i,j,k+1}\Delta z_k}{\Delta z_{k+1}+\Delta z_k} \tag{3.62}$$

which corresponds to the dimensionless temperature:

$$\frac{T_{i,j,k+\frac{1}{2}}-T^0}{\Delta T^*}=\frac{1}{2}\left(\frac{T_{i,j,k}-T^0}{\Delta T^*}+\frac{T_{i,j,k+1}-T^0}{\Delta T^*}\right) \tag{3.63}$$

where, $(T_{i,j,k}-T_{ref})/\Delta T_{ref}$ is evaluated using (3.60).

Liquid metal test case

For the verification of the time integration scheme and of the conductive terms we consider, first, the oscillatory natural convection of a low-Prandtl-number fluid subject to buoyancy forces in a long horizontal cavity whose vertical walls are maintained at constant (different) temperatures: T_1 and T_2. The domain has an aspect ratio $H/L = 4$ and is assumed to be infinite in y-direction (Fig. 3.5). The horizontal walls bounding the domain in z-direction are considered as adiabatic walls.

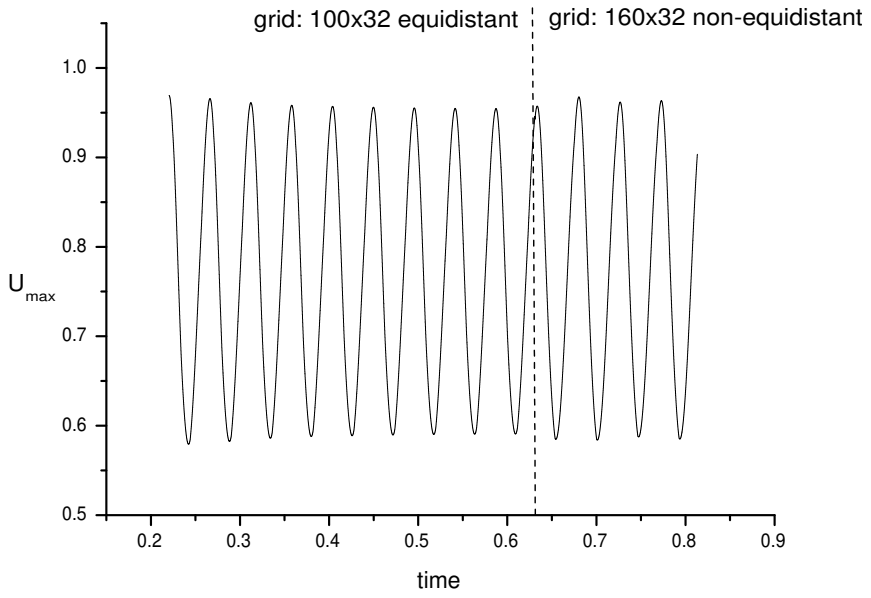

Fig. 3.6: Time variation of the maximum value of the horizontal velocity component U_{max} in the test section.

Experiments performed by Hart [14] and Hurle *et al.* [19] establish that the buoyancy-driven flow, which appears as soon as $T_1 \neq T_2$, becomes oscillatory beyond a certain critical value of the Grashof number, which is defined using $\Delta T^* = T_2 - T_1$ as reference temperature difference.

In Fig. 3.6, the time dependence of the maximum value of the horizontal velocity in the test section for a oscillatory convection at `Gr` = 40000 is shown. The value of the Prandtl number is Pr = 0.015. Two different grids have been used: one with 100×32 equidistant cells and an other with 160×32 cells which are equidistant in x-directions and non-equidistant in z-direction. Using a non-equidistant grid enables us to solve with a higher precision the laminar layer near the wall. To emulate a 2D computation, in the direction perpendicular on the flow plane (y) 4 mesh cells have been considered in both simulations. In order to reach faster the limit cycle of the instability the computations for the finer grid are started from an interpolated velocity and temperature fields obtained for the coarser grid.

In the literature there are no experiments available for this `Gr` and Pr numbers. To verify our computations we use the numerical results from Behnia and de Vahl Davis [1] which

	Grid	U_{max}	f
equidistant grid	100×32	0.9546	21.62
non-equidistant grid	160×32	0.9634	21.81
Behnia & de Vahl Davis [1]	321×81	1.093	21.76

Tab. 3.2: Oscillatory convection: maximum value of the horizontal velocity in the test section and oscillations frequency and comparison with reference values

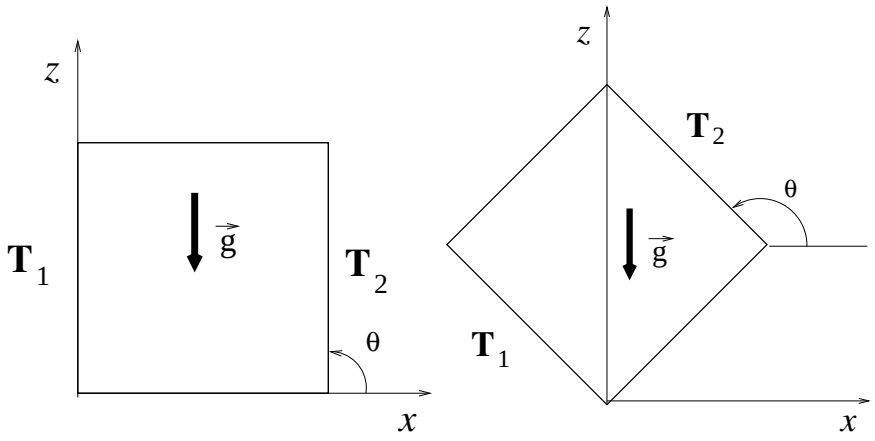

Fig. 3.7: Natural convection of air in tilted square cavities

used a 321×81 computational grid for their simulations. In Table 3.2 the reference values from [1] for maximum of the horizontal velocity in the test section and oscillations frequency are compared with the results obtained using our numerical method. For both grids, equidistant and non-equidistant, the values of U_{max} are with 13% and 11%, respectively, lower than the reference value. However, for grid refinement U_{max} has the correct trend. In the case of flow oscillation frequencies, the values obtained using our method match the reference values within an error of 0.6% for the equidistant grid and 0.2% for the non-equidistant grid.

Natural convection of air in a square enclosure

The second test case considers the natural convection of air ($\mathtt{Pr} = 0.71$) in a 2D square enclosure. Same as for the previous case, two opposite walls are maintained at constant temperatures T_1 and T_2 and the other two walls are adiabatic. Two different situations are considered: in the first one the heated walls are parallel with the vertical direction while, in the second case, they make an angle of 45° with the vertical (see Fig. 3.7). In both cases $\mathtt{Ra} = 1.01 \times 10^5$ and the temperature difference is $\Delta T^* = 10$ K. The cold wall

temperature is considered as reference temperature $T^0 = T_1 = 303$ K. The computation domain is discretized in $32 \times 4 \times 32$ uniform cells. For a grid refinement study a finer grid with $64 \times 4 \times 64$ cells is used.

The overall heat transfer across the cavity can be represented by a Nusselt number defined by

$$\mathtt{Nu} = \frac{-\int_0^H \left(\lambda \frac{\partial T}{\partial x}\right)_w dz}{\lambda \Delta T^*}$$

where the wall heat flux $(\lambda\, \partial T/\partial x)_w$ is computed either at the cold wall ($w = 1$) or the hot wall ($w = 2$). There are several correlations in the literature for the natural convection of air in tilted cavities. For the case when the heated walls are vertical Zhong, Yang and Lloyd [62] proposed the following correlation

$$\mathtt{Nu}(90^\circ) = \frac{\mathtt{Ra}^{0.322}}{8 + \left(\frac{\alpha_2}{\alpha_1}\right)^{0.84}} \tag{3.64}$$

where, α_1 and α_2 are the thermal diffusivity of the air at the cold and, respectively, the hot wall. Since we use the Boussinesq approximation this ratio is equal to unity. This formula is valid for a Rayleigh number in the interval

$$\mathtt{Ra}_{lim} = 780 \left(1 + \frac{\Delta T^*}{T^0}\right)^{2.7} \leq \mathtt{Ra} \leq 10^6$$

where, the lower limit is equal to $\mathtt{Ra}_{lim} = 851.5$. For the case when the cavity is tilted with an angle of $\theta = 135^\circ$ to the horizontal Zhong, Lloyd and Yang [61] proposed the following relation for the Nusselt number:

$$\mathtt{Nu}(\theta) = \mathtt{Nu}(180^\circ) + \frac{2}{\pi}(\pi - \theta)(\mathtt{Nu}(90^\circ) - \mathtt{Nu}(180^\circ)) \sin\theta \tag{3.65}$$

where $\mathtt{Nu}(180^\circ)$ is the Nusselt number for pure convection. This correlation is valid for

$$10^4 \leq \mathtt{Ra} \leq 10^6\,, \quad \frac{\Delta T^*}{T^0} \leq 2.0$$

In Table 3.3 the computed Nusselt numbers are compared with those given by the

Nu	$\theta = 90°$	$\theta = 135°$
$32 \times 4 \times 32$	4.77	2.079
$64 \times 4 \times 64$	4.65	2.097
literature [62, 61]	4.52	2.24

Tab. 3.3: Nusselt number for natural convection of air in tilted cavities

empirical correlations (3.64) and (3.65). In the case of vertical heated walls ($\theta = 90°$) the Nusselt number obtained from the numerical simulation is with $\varepsilon = 5.5\%$ larger than the one obtained using (3.64). Refining the grid reduces the difference to only $\varepsilon = 2.9\%$. When the cavity is tilted with $\theta = 135°$ a lower value for the Nusselt number than the one given by (3.65) is obtained. For the coarse grid ($32 \times 4 \times 32$) the difference between these two values is $\varepsilon = 7.2\%$ while, in the case of finer grid the difference is reduced to $\varepsilon = 6.4\%$.

4. SMALL CHANNELS TWO-PHASE FLOWS

For small channels the length is typically much larger than the hydraulic diameter therefore, one can identify a region along the channel where there is no influence of the entrance effects. If the flow itself has an intrinsic periodicity, a characteristic *flow cell* can be defined. This flow cell has the same length as the periodicity length of the flow and fully characterizes the flow in its steady state. Experimentally, this fluid cell is the domain where the observations are done either following it in its movement along the channel (e.g. with a mounted camera) or considering a fixed volume with the same dimensions as the fluid cell. For numerical simulation the second approach is more convenient since it can be reproduced using periodic boundary conditions.

In real life applications periodic steady flows are often used when the process needs to be controlled as it is the case in chemical processing. Slug flow in small channels is an example of a two-phase flow regime with increased heat and mass transfer rates compared to single-phase. This type of flow, also referred as bubble-train flow [48, 49], consists of trains of long bubbles separated by liquid slugs. The bubbles occupy most of the channel cross-section while the liquid slugs are free of smaller bubbles [52]. Breakage and coalescence of bubbles is largely absent. Due to the dominance of the surface tension effects the walls are always wetted and a thin liquid layer separates the gas from the channel walls.

In this chapter, a new method to describe a steady periodic two-phase flow is presented. Throughout the chapter, the steady slug (bubble-train) flow is considered as the prototype of the periodic two-phase flow in small channels. The liquid will be referred as fluid 1 or continuous phase, while the gas will represent the fluid 2 or dispersed phase.

Throughout this chapter it is assumed that the temperature variations are not large enough to determine a change in fluids properties along the channel. The first consequence of this assumption is that the momentum equation it is not coupled with the energy equation and can be treated separately. First, the case of an adiabatic flow is considered and a new concept called *periodic fully developed regime* is introduced. The convective heat

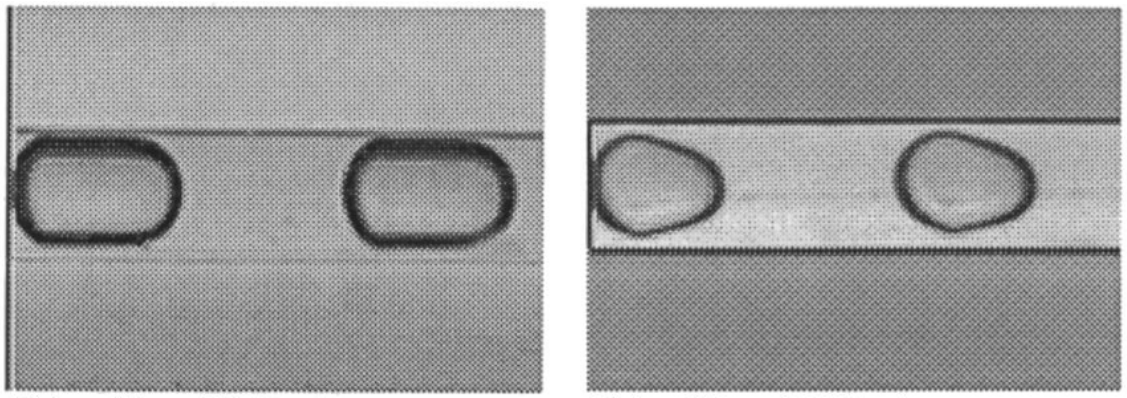

(a) (b)

Fig. 4.1: Slug flow in a circular (a) and triangular (b) channel. Reproduced from [52]

transfer problem when a axially periodic heat flux is imposed as wall boundary condition will be discussed next.

4.1 Periodic fully developed flow

For two-phase flows, a fully developed regime, as defined by (3.34), is possible to be identified only for annular flows. In small channels, the velocity profiles strongly depend on the gas distribution along the channel. However, for bubble-train regime, far from the entrance region, there is a uniform distribution of the bubbles along the channel, i.e. bubbles have the same shape and the liquid slugs separating the bubbles have the same length (see Fig. 4.1). For such situations, one can identify a cell (of length L) which characterizes the flow (Fig. 4.2). It is said that the flow is periodic fully developed if the density[1]and the velocity field are periodic in stream-wise direction:

$$\begin{aligned} \rho(x,y,z) &= \rho(x,y+L,z) = \rho(x,y+2L,z) = \dots \\ \vec{\mathsf{v}}(x,y,z) &= \vec{\mathsf{v}}(x,y+L,z) = \vec{\mathsf{v}}(x,y+2L,z) = \dots \end{aligned} \tag{4.1}$$

Since the velocity and the density/viscosity and theirs derivatives are periodic it can be shown that the pressure gradient is also periodic. If β is the pressure drop along the

[1] Since the fluids are incompressible the density periodicity implies the same periodicity for the phases distribution X_φ.

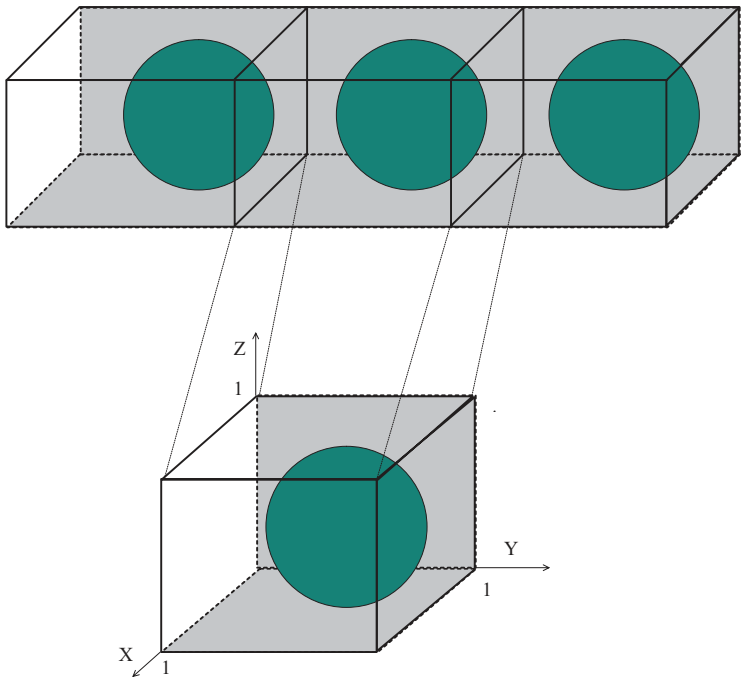

Fig. 4.2: Computational domain and initial condition

channel defined as:

$$\beta = \frac{1}{L_x L_z} \sum_{\varphi=1,2} \int_0^{L_x} \int_0^{L_z} \left(p_\varphi(x, y+L, z) - p_\varphi(x, y, z) \right) X_\varphi(x, y, z) \, dxdz \tag{4.2}$$

then, integrating the momentum equation (2.36b) over the volume of the characteristic cell one has:

$$\beta = \frac{1}{\mathtt{Re}} \frac{1}{L} \int_0^{L} \left\{ \int_0^{L_x} \left[\mu_1 \frac{\partial v}{\partial z}(x, \eta, L_z) - \mu_1 \frac{\partial v}{\partial z}(x, \eta, 0) \right] dx \right.$$
$$\left. + \int_0^{L_z} \left[\mu_1 \frac{\partial v}{\partial x}(L_x, \eta, z) - \mu_1 \frac{\partial v}{\partial x}(0, \eta, z) \right] dz \right\} d\eta \tag{4.3}$$

In the previous formula we use the fact that all four channel walls are wetted and no contact line appears. This means that the surface tension integral is zero. One can see

that β is constant and is equal to the wall friction per unit length. The *reduced pressure*

$$P_\varphi(x,y,z) = p_\varphi(x,y,z) - \beta y \ , \quad \varphi = 1,2 \tag{4.4}$$

is then periodic in stream-wise direction, same as the density or the velocity. Also, since the pressure drop is constant, the reduced pressure field satisfies the interface jump condition (2.39):

$$P_{1i} - P_{2i} = -\frac{1}{\mathtt{We}}\sigma\kappa + \frac{1}{\mathtt{Re}}(\boldsymbol{\tau}_{1i} - \boldsymbol{\tau}_{2i}) : \vec{\mathtt{n}}\vec{\mathtt{n}} \tag{4.5}$$

This means that, instead of simulation the entire flow, it is enough to compute the flow inside this characteristic domain. For the rest of the channel (except the entrance region) the density and velocity field can be found using the periodicity property while the pressure field is computed using (4.4).

When the gravity is considered we have to combine (2.37) and (4.4). The reduced pressure field is in this case:

$$P_\varphi(x,y,z) = p_\varphi(x,y,z) - \frac{1}{\mathtt{Fr}}\frac{\rho_1}{\rho^*}\frac{\vec{\mathtt{g}}}{g}\cdot\vec{\mathtt{x}} - \beta y \ , \quad \varphi = 1,2 \tag{4.6}$$

The jump condition (4.5) holds also for this case.

4.1.1 Pressure Gradient Correction

In the original version of the computer code `TURBIT-VoF` it was assumed that when inside a computational cell we have both fluids (interface cell) they share the same pressure. This assumption works well as long as the pressure jump at the interface is small. This is generally the case for large, deformable bubbles in large channels for which `TURBIT-VoF` was developed. When the bubble size diminishes, the interface curvature increases which results in an increase of the pressure jump at the interface. In dimensionless form, this corresponds to a decrease of the bubble Weber number. In large channels, an air bubble of 1 mm diameter in water can be considered as spherical and, its movement can be described using simple models. For this kind of bubbles there is no need to perform an interface tracking and reconstruction. If we consider, now, a similar bubble in a small channel, the bubble shape is strongly influenced by the presence of the channel walls and has to be treated as being "large" and deformable. The pressure jump at the interface is of the same order of magnitude as for the large channels but in this case the interface dynamics

has to be solved numerically. Using the original model for the pressure implemented in `TURBIT-VoF` can result in a smeared pressure gradient at the interface.

In this section we propose an improved model to account for the pressure jump at the interface. For easy reference, the numerical algorithm used in `TURBIT-VoF` will be summarized, first. Using the notations introduced by Sabisch [38] the equation (2.36b) can be written as:

$$\frac{\partial(\rho\vec{\mathrm{v}})}{\partial t} + \mathcal{K} - \mathcal{D} - \mathcal{Q} - \mathcal{O} = -\nabla P \tag{4.7}$$

where, $\mathcal{K}$ is the convective term, $\mathcal{D}$ is the diffusive term, $\mathcal{Q}$ is the body force and $\mathcal{O}$ stands for surface tension force. To compute the velocity field, a projection method is used: first, an intermediate momentum (velocity) field is computed as:

$$\frac{\partial}{\partial t}(\rho\vec{\mathrm{v}})^* = -\mathcal{K} + \mathcal{D} + \mathcal{Q} \tag{4.8}$$

where the velocity components are computed on a staggered grid. This velocity field is not divergence-free, therefore, a Poisson equation for the pressure is solved in order to enforce the condition of a solenoidal velocity field:

$$\nabla \cdot \left[\frac{1}{\rho}\nabla p\right] = \nabla \cdot \left(\frac{\partial \vec{\mathrm{v}}^*}{\partial t}\right) + \nabla \cdot \left[\frac{1}{\rho}\mathcal{O}\right] \tag{4.9}$$

The pressure equation is approximated numerically as:

$$\nabla \left[\frac{\Delta t}{\rho^{n+1}}\nabla p^{n+1}\right] = \nabla \cdot \vec{\mathrm{v}}^* + \nabla \cdot \left[\frac{\Delta t}{\rho^{n+1}}\mathcal{O}^{n+1}\right] \tag{4.10}$$

The superscripts are indicating the time step at which the terms are computed. To ensure the consistency of the method the pressure is defined on a centered grid.

In all above equations the variables are mean quantities, i.e. they are obtained using the averaging procedure introduced in Chapter 2. Thus these values are characteristic to the volume where they are defined and not to a specific point. Using staggered grids may complicate the problem since different volumes are used to define the velocity components and the pressure. In the next subsections we will analyze what are the approximations used in `TURBIT-VoF` and what are the errors introduced due to these approximations.

Discrete pressure equation

An important aspect of the numerical method is how the pressure equation is constructed when a projection method with a staggered grid is used to enforce the divergence–free condition for the velocity.

Discretizing separately the momentum equation (4.8) and the Poisson equation (4.9) for the pressure might produce a violation of the consistency of the divergence operator with the gradient operator (Ferziger & Perić [8]). To avoid this we will derive the equation for the pressure from the discretized momentum and continuity equations. Using the same notation as in previous section, the semidiscretized form of the momentum equation (4.7) in the x -direction is:

$$\frac{\partial}{\partial t}(\rho u)_{i+\frac{1}{2},j,k} \;+\; \mathcal{L}^x_{i+\frac{1}{2},j,k} \;-\; \mathcal{O}^x_{i+\frac{1}{2},j,k} \;=\; -\frac{1}{V_{i+\frac{1}{2}}}\left[\int\limits_{S^x_{i+1,j,k}} p\; dS - \int\limits_{S^x_{i,j,k}} p\; dS\right] \tag{4.11}$$

where,

$$\mathcal{L}^x_{i+\frac{1}{2},j,k} = \mathcal{K}^x_{i+\frac{1}{2},j,k} - \mathcal{D}^x_{i+\frac{1}{2},j,k} - \mathcal{Q}^x_{i+\frac{1}{2},j,k} \tag{4.12}$$

and

$$\rho_{i+\frac{1}{2},j,k} = f_{i+\frac{1}{2},j,k}\rho_1 + (1 - f_{i+\frac{1}{2},j,k})\rho_2 \tag{4.13}$$

For the construction of the discrete gradient we take in account that the differential equation (4.7) is written for volume average values of the variables. The surface integrals can be written as:

$$\int\limits_{S^x_{i,j,k}} p\; dS = \left[f^x_{i,j,k}\bar{p}^{(1)}_{i,j,k} + (1 - f^x_{i,j,k})\bar{p}^{(2)}_{i,j,k}\right]\Delta y_j \Delta z_k \tag{4.14}$$

where, $\bar{p}^{(1)}_{i,j,k}$ and $\bar{p}^{(2)}_{i,j,k}$ are the surface averaged values of the pressure in the fluid 1 and 2, and $f^x_{i,j,k}$ is the surface fraction of the surface $S^x_{i,j,k}$ which is inside the fluid 1. Following the same integration strategy as in `TURBIT-VoF` we are computing first a provisional solution $(\rho\vec{\mathbf{v}})^*$ of the momentum at time $(n+1)\Delta t$. This is done using an explicit scheme. The

relation between the momentum at time $(n+1)\Delta t$ and the approximate momentum is:

$$(\rho u)^{n+1}_{i+\frac{1}{2},j,k} = (\rho u)^{*}_{i+\frac{1}{2},j,k} + \mathcal{O}^{x}_{i+\frac{1}{2},j,k} - \frac{\Delta t}{V_{i+\frac{1}{2},j,k}} \left[\int\limits_{S^{x}_{i+1,j,k}} p \, dS - \int\limits_{S^{x}_{i,j,k}} p \, dS \right] \tag{4.15}$$

Next, we need to ensure the divergence–free condition for the velocity field at next time step $\vec{\mathsf{v}}^{n+1}$. At this point it is useful to define the intermediate velocity field in terms of momentum fields:

$$(\rho u)^{n+1}_{i+\frac{1}{2},j,k} = \rho^{n+1}_{i+\frac{1}{2},j,k} (u)^{n+1}_{i+\frac{1}{2},j,k}, \tag{4.16}$$

$$(\rho u)^{*}_{i+\frac{1}{2},j,k} = \rho^{n+1}_{i+\frac{1}{2},j,k} (u)^{*}_{i+\frac{1}{2},j,k} \tag{4.17}$$

Thus, using a central difference scheme for the divergence operator an approximate pressure equation for the node (i,j,k) can be constructed:

$$\nabla^{h} \cdot \left(\frac{\Delta t}{\rho} \nabla^{h} p_{i,j,k} \right) = \nabla^{h} \cdot \vec{\mathsf{v}}^{*} + \nabla^{h} \cdot \left[\frac{\Delta t}{\rho} \mathcal{O} \right] \tag{4.18a}$$

where,

$$\begin{aligned} \nabla^{h} \cdot \left(\frac{\Delta t}{\rho} \nabla^{h} p_{i,j,k} \right) = {} & A^{(1)}_{i,j,k} p^{(1)}_{i,j,k} + A^{(2)}_{i,j,k} p^{(2)}_{i,j,k} \\ & + A^{(1)}_{i+1,j,k} p^{(1)}_{i+1,j,k} + A^{(2)}_{i+1,j,k} p^{(2)}_{i+1,j,k} + A^{(1)}_{i-1,j,k} p^{(1)}_{i-1,j,k} + A^{(2)}_{i-1,j,k} p^{(2)}_{i-1,j,k} \\ & + A^{(1)}_{i,j+1,k} p^{(1)}_{i,j+1,k} + A^{(2)}_{i,j+1,k} p^{(2)}_{i,j+1,k} + A^{(1)}_{i,j-1,k} p^{(1)}_{i,j-1,k} + A^{(2)}_{i,j-1,k} p^{(2)}_{i,j-1,k} \\ & + A^{(1)}_{i,j,k+1} p^{(1)}_{i,j,k+1} + A^{(2)}_{i,j,k+1} p^{(2)}_{i,j,k+1} + A^{(1)}_{i,j,k-1} p^{(1)}_{i,j,k-1} + A^{(2)}_{i,j,k-1} p^{(2)}_{i,j,k-1} \end{aligned} \tag{4.18b}$$

and

$$A^{(1)}_{i+1,j,k} = \frac{\Delta t}{h^2} \frac{1}{\rho_{i+\frac{1}{2},j,k}} f^{x}_{i+1,j,k} A^{(2)}_{i+1,j,k} = \frac{\Delta t}{h^2} \frac{1}{\rho_{i+\frac{1}{2},j,k}} (1 - f^{x}_{i+1,j,k}) \tag{4.18c}$$

$$A^{(1)}_{i-1,j,k} = \frac{\Delta t}{h^2} \frac{1}{\rho_{i-\frac{1}{2},j,k}} f^{x}_{i-1,j,k} A^{(2)}_{i-1,j,k} = \frac{\Delta t}{h^2} \frac{1}{\rho_{i-\frac{1}{2},j,k}} (1 f^{x}_{i-1,j,k}) \tag{4.18d}$$

$$A^{(1)}_{i,j,k} = -\frac{\Delta t}{h^2}\left[\left(\frac{1}{\rho_{i+\frac{1}{2},j,k}}+\frac{1}{\rho_{i-\frac{1}{2},j,k}}\right)f^x_{i,j,k}+\left(\frac{1}{\rho_{i,j+\frac{1}{2},k}}+\frac{1}{\rho_{i,j-\frac{1}{2},k}}\right)f^y_{i,j,k}\right.$$
$$\left.+\left(\frac{1}{\rho_{i,j,k+\frac{1}{2}}}+\frac{1}{\rho_{i,j,k-\frac{1}{2}}}\right)f^z_{i,j,k}\right] \tag{4.18e}$$

$$A^{(2)}_{i,j,k} = -\frac{\Delta t}{h^2}\left[\left(\frac{1}{\rho_{i+\frac{1}{2},j,k}}+\frac{1}{\rho_{i-\frac{1}{2},j,k}}\right)(1-f^x_{i,j,k})\right. \tag{4.18f}$$
$$\left.+\left(\frac{1}{\rho_{i,j+\frac{1}{2},k}}+\frac{1}{\rho_{i,j-\frac{1}{2},k}}\right)(1-f^y_{i,j,k})+\left(\frac{1}{\rho_{i,j,k+\frac{1}{2}}}+\frac{1}{\rho_{i,j,k-\frac{1}{2}}}\right)(1-f^z_{i,j,k})\right]$$

The other coefficients can be obtained replacing the corresponding indices. For the coefficients expressions a mesh with constant grid width in each direction has been considered ($\Delta x = \Delta y = \Delta z = h$). This was made just for an easier presentation and is not an restriction of the method.

The first observation regarding the structure of the approximate Laplacian is that the surface fractions are involved and not the volume fractions. This feature rises two main problems: first, the surface fractions depend on the surface orientation and we can not define a mean pressure in the volume centered in (i, j, k) as $p_m = f\bar{p}^{(1)} + (1-f)\bar{p}^{(2)}$, and, second, the pressures $\bar{p}^{(1)}$ and $\bar{p}^{(2)}$ are surface averages and not volume averages. The last problem can be avoided using pressure volume averages $\bar{p}^1_{i,j,k}$ and $\bar{p}^2_{i,j,k}$ instead of surface averages. This approximation is consistent with the approximations made in chapter 2 when the general equations were obtained. However, this will not entirely solve our problems because we still need two values for the pressure at each grid cell.

In `TURBIT-VoF` a mean value for the pressure is defined on the control volume centered in $\mathbf{P}(i, j, k)$ and is used for both faces. This is the same as assuming that $f^x_{i,j,k} = f^y_{i,j,k} = f^z_{i,j,k} = f_{i,j,k}$ or that the local deviations of the pressure from the mean value, which are usually ignored, balance the effect of unequal splitting of the faces. This might be true in cells where the fraction of volume f is around 0.5 and the interface splits the cell in two equal parts but does not hold if the interface is parallel with one of the cell faces. In such cases, the corresponding surface fraction will be either 0 or 1 depending on which fluid is the center of the cell, while the volume fraction $0 < f_{i,j,k} < 1$. This wrong estimation of the coefficients in the pressure equation results in a smeared pressure jump at the interface which affects the computed velocity in the cells containing both fluids.

A solution to this problem is proposed by Popinet and Zaleski [37]. They use a

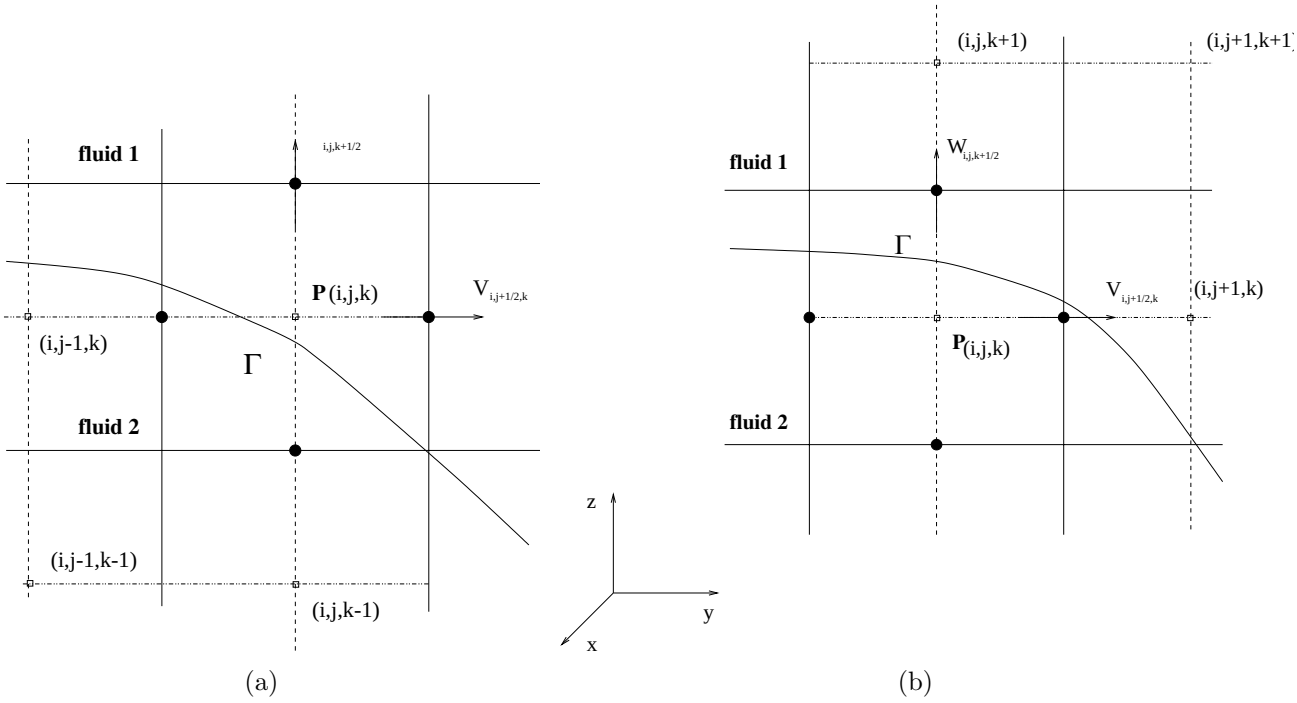

Fig. 4.3: The location of the interface relative to the pressure nodes

"pressure–gradient correction" in order to take in account this effect. They approximate the face integrals using the nearest pressure nodes. Thus only one value for the pressure is needed at each grid point. Let write the relation (4.14) in a form similar to the formulation from [37] (see fig. 4.3):

- if the center of the cell (i, j, k) is inside fluid 1:

$$\int\limits_{S^x_{i,j,k}} p\, dS = \Delta y_{i,j,k}\Delta z_{i,j,k}\left[p^{(1)} + (1 - f^x_{i,j,k})(p^{(2)} - p^{(1)})\right] \tag{4.19a}$$

- or, if the center of the cell is inside the fluid 2:

$$\int\limits_{S^x_{i,j,k}} p\, dS = \Delta y_{i,j,k}\Delta z_{i,j,k}\left[p^{(2)} + f^x_{i,j,k}(p^{(1)} - p^{(2)})\right] \tag{4.19b}$$

We can see that approximating $p^{(1)}$ and $p^{(2)}$ with the averaged values of the pressure ($\overline{p}^1$ and $\overline{p}^2$) we get an equation for the averaged values of pressure instead an equation for mean value of the pressure p_m.

The above relations are considered as a correction to the standard centered estimate. This leads to a discretization of the Poisson equation in the form:

$$\nabla^h \cdot \nabla^h (p^{(n+1)} + I[p^{(n+1)}]) = \nabla^h \cdot \mathsf{v}^* \tag{4.20}$$

where, $I[p^{(n+1)}]$ is the pressure gradient correction defined as:

$$I_{i,j,k}[p] = \Delta y_{i,j,k} \Delta z_{i,j,k} (1 - f^x_{i,j,k})(\overline{p}^2 - \overline{p}^1) \tag{4.21a}$$

if $\mathbf{P}(i,j,k)$ is inside fluid 1, and

$$I_{i,j,k}[p] = \Delta y_{i,j,k} \Delta z_{i,j,k} f^x_{i,j,k} (\overline{p}^1 - \overline{p}^2) \tag{4.21b}$$

if $\mathbf{P}(i,j,k)$ is inside fluid 2; ∇^h is the discrete operator The matrix of the linear system associated to the equation (4.20) has a structure which depends strongly on the way the pressure gradient correction is constructed. This means that the nonzero terms appearing in the matrix are no longer arranged in diagonals and the faster numerical algorithms developed for this kind of matrices can not be used. For a projection method solving the system associated to the pressure equation is the most computational demanding part of the algorithm therefore it is useful to find an approximation of (4.20) which recovers the diagonal structure of the matrix. Popinet and Zaleski [37] considered the pressure gradient correction as a source term in the momentum balance equation. Using the pressure at time-step (n) to compute this correction, the approximate pressure equation is:

$$\nabla^h \cdot \nabla^h p^{(n+1)} = \nabla^h \cdot \mathsf{v}^* - \nabla^h \cdot \nabla^h I[p^{(n)}] \tag{4.22}$$

We still need to evaluate $\overline{p}^1 - \overline{p}^2$. In 2D this can be done very easy. Popinet and Zaleski [37] used the pressure of the closest point and $I[p]$ is expressed in terms of p_i, p_{i+1}, p_{i-1}. In 3D this procedure needs some modifications because we have three neighboring values ($p_{i,j+1,k}$, $p_{i,j,k+1}$, $p_{i,j+1,k+1}$ or $p_{i,j+1,k}$, $p_{i,j,k+1}$, $p_{i,j+1,k+1}$) for the unknown pressure. In this case we have two options:

- compute $\overline{p}^1 - \overline{p}^2$ taking the unknown pressure from the closest grid point which is in the same fluid; or,
- compute $\overline{p}^1 - \overline{p}^2$ using a pressure jump model.

Inhere we consider the first approach since its implementation is straightforward.

4.1.2 Bubble-train flow in a channel of square cross-section

To verify the method described above we consider the case of a bubble-train flow in a channel with square cross-section ($L_x = L_z = 1$). The periodicity length L is taken the same as the width of the channel. Thus, our fluid cell is a cube having the dimensions $1 \times 1 \times 1$. In Fig. 4.2 the coordinate system and a sketch of the computational domain is presented. The computational domain is discretized by 64^3 uniform mesh cells. The flow is in y-direction while in the other two directions walls bound the domain where no-slip boundary conditions are used. The presence and influence of the neighboring unit cells is simulated using periodic boundary conditions in stream-wise direction.

The simulation is started from an initially spherical bubble with diameter $d = 0.858$; this corresponds to an overall void fraction of $\varepsilon = 33\%$. To determine a specific overall flow rate a constant pressure drop is imposed in stream-wise direction. After a transient, the simulation results in a fully developed regime with steady bubble shape and constant gas (J_2) and liquid (J_1) flow rates.

	ε	ρ_2/ρ_1	μ_2/μ_1	Re	Eo	$-\beta$	J_1/J	J_2/J
BT1	33%	1/81	1/260	1.35	1.065	27	0.806	1.89
BT2	33%	1/78	1/25	75.88	1.347	0.2	1.04	1.10

Tab. 4.1: Simulation parameters for bubble-train flow. The Re and Eö numbers are computed using the bubble diameter and bubble velocity as reference length, and velocity, respectively.

We performed simulations for two different cases (Table 4.1). The fluids properties correspond to an experiment where the flow of air bubbles in silicone oil of different viscosities in a square channel is investigated [48]. In order to increase the computational efficiency, in the numerical simulation the gas density and viscosity is chosen 10 times higher than in the experiment [48]. Since we are interested only on the fully developed regime modifying the density and viscosity ratio has no influence on the final results [59].

The first case (BT1) simulates a flow for which the kinematic viscosity of the continuous phase (liquid) is three times larger than for the dispersed phase (gas). This results in a relatively thick liquid layer near the wall while the bubble remains axisymmetric. After a very short transient ($t = 0.12$) the liquid reaches a constant flow rate while for the gas

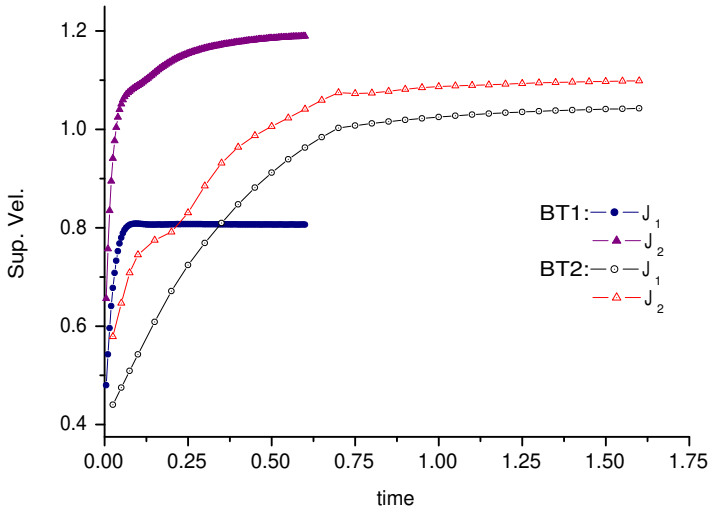

Fig. 4.4: Time evolution of the dimensionless liquid (J_1) and gas (J_2) superficial velocities

flow rate it takes longer to reach the steady regime. At $t = 0.6$ the slope of the bubble velocity increase in time is only 0.04 and we assumed that it has reached its final velocity (Fig. 4.4).

In the second case (BT2) the liquid is taken to be less viscous than in the first case, therefore it takes more time to reach a steady bubble shape and bubble velocity. For times larger than t = 1.0 the liquid and gas superficial velocities increase very slowly in time. The slope is smaller than 0.03 and therefore we assume that the fully developed regime has been reached. The bubble diameter becomes larger than in the (BT1) case and almost fills the channel width. Since the liquid film in the axial planes becomes very thin the liquid is pushed to the corners of the channel and it is strongly accelerated. This results in a stronger mixing both in the liquid slug and inside the bubble. The flow inside the bubble for the two cases is compared in Fig. 4.5. For that, we consider the referential linked to the bubble center of mass and insert massless particles into the flow at different position inside the bubble. Since the flow is steady and the bubbles move with constant speed there is no need to take in to account acceleration effects. For (BT1) the gas inside the bubble forms a single annular vortex (Fig. 4.5.a) while in (BT2) a second vortex appears at the rear side of the bubble (Fig. 4.5.b). The presence of the second vortex can be explained by a breakage of the symmetry of the flow inside the bubble due to higher `Re` number. The

geometry of the channel and the fact that the walls are close to the bubble interface have also an influence on the movement of particles inside the bubble. In the cross-section, the thickness of the liquid film surrounding the bubble varies along each channel side. This results in a azimuthal movement of the particles inside the bubble (see Fig. 4.5.c and .d). The mixing in azimuthal direction is more intense for BT2 case which has a higher `Re` number and a thinner liquid film while in BT1 case the flow is almost axisymmetric.

The mixing characteristics of the flow inside the bubble is of great interest in chemical processing where the bubbles are used as micro-reactors in which the precipitation reagents are thoroughly mixed avoiding the heterogeneous reaction conditions in classical large batch reactors. For the heat exchangers, the structure of the flow inside the liquid is more important. In Fig. 4.6 the flow in the liquid layer between the bubble and the walls and in the liquid slug is presented. Again, a referential linked to the bubble is used. The massless particles are inserted in front of the bubble ($y = 1$). At the corner of the channel the particles have a rectilinear trajectory and their velocity is almost constant along the channel. Close to the bubble, particles are accelerated as they approach the cross-section where the bubble has the larger diameter, and then decelerate, some of the particles being captured in the vortex behind the bubble in (BT2). For the (BT1) case the acceleration of the particles near the bubble is less important than for (BT2) and the particles are not trapped in the liquid slug. For the (BT2) case, the presence of the second vortex inside the bubble generates also two vortices in the liquid slug: one close to the rear side of the bubble that is coupled with the vortex at the bottom of the bubble, and a second one coupled with the vortex at the top of the next bubble. In both cases the `Eo` number is close to unity, that means that the Laplace constant and the channel hydraulic diameter (D_h) have the same order of magnitude. For a air-water system this corresponds to a channel having a width around 1 mm.

In order to assess our numerical code we compare the results with the experimental data obtained by Thulasidas *et al.* [48] (Fig. 4.7). They measured the bubble diameter and the bubble velocity for a bubble-train flow in a square channel with a hydraulic diameter of 2mm. From the measured values they compute the dimensionless bubble diameter D_B/D_h, dimensionless bubble velocity U_B/J, and the relative bubble velocity $W = (U_B - v_{ls})/U_B$, where $J = J_1 + J_2$ is the total superficial velocity and v_{ls} is the liquid slug velocity. They plot their results as a function of the Capillary number of the flow which is defined as the

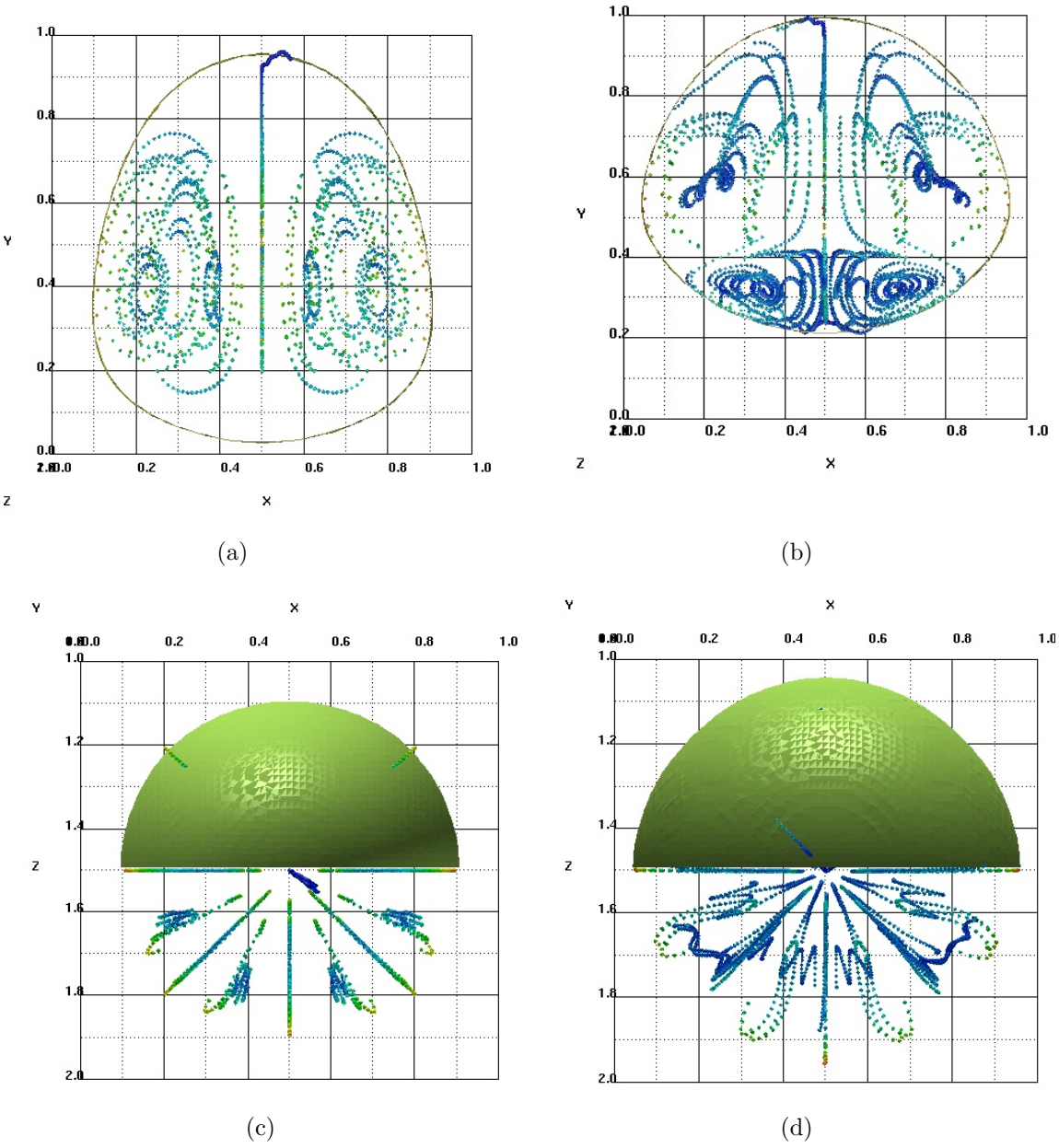

(a) (b)

(c) (d)

Fig. 4.5: Visualization of the flow structure inside the bubble for the BT1 case (a, c) and BT2 case (b, d): front view (a, b); top view (c, d). Massless particles were inserted inside the bubble and advected by the velocity field, in a referential linked to the bubble center of mass.

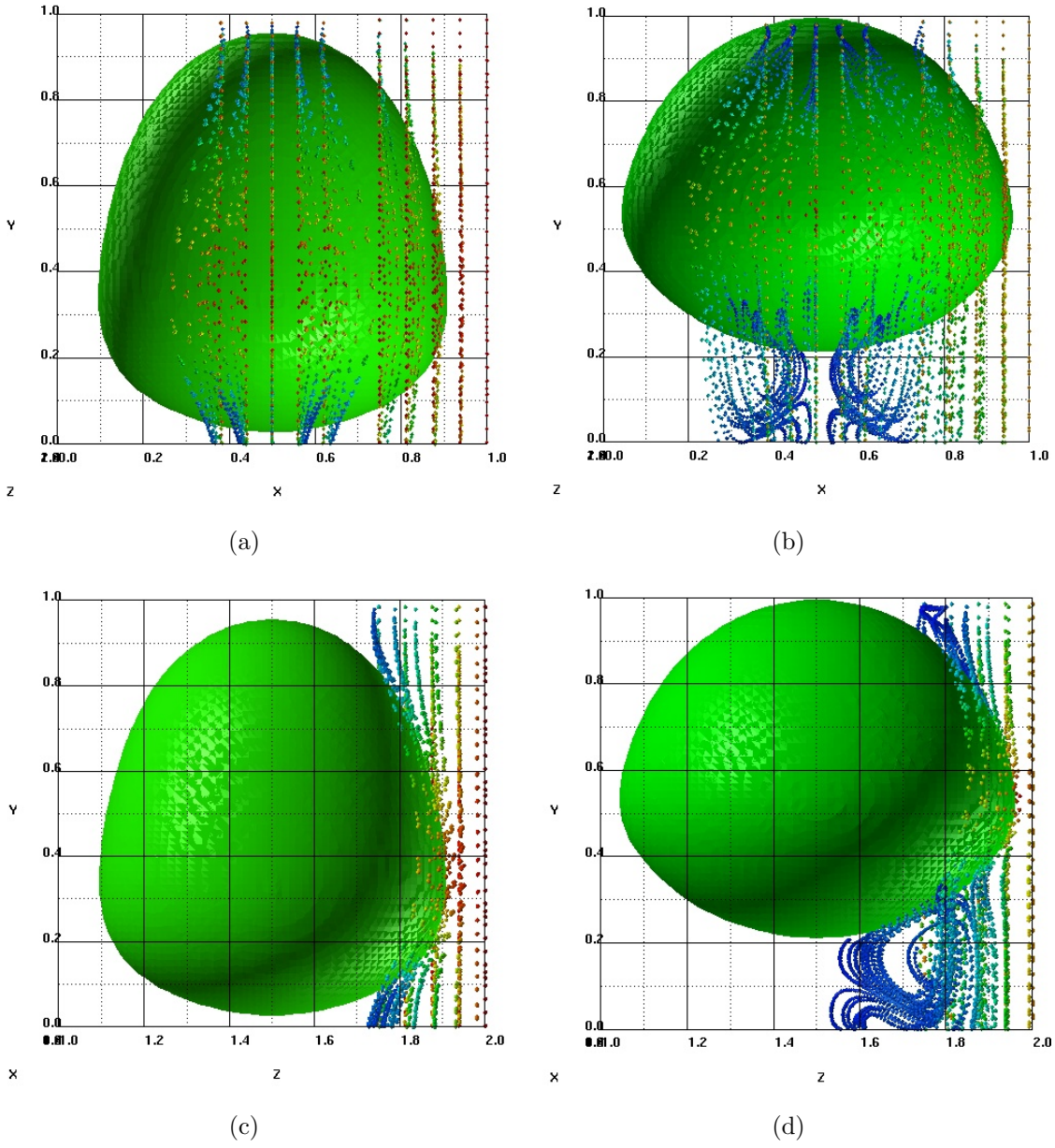

Fig. 4.6: Visualization of the flow structure in the liquid for the BT1 case (a, c) and BT2 case (b, d): front view (a, b); lateral view (c, d). A referential linked to the bubble center of mass is used. The massless particles are inserted in the top of the computational domain and they move along the current lines of the flow.

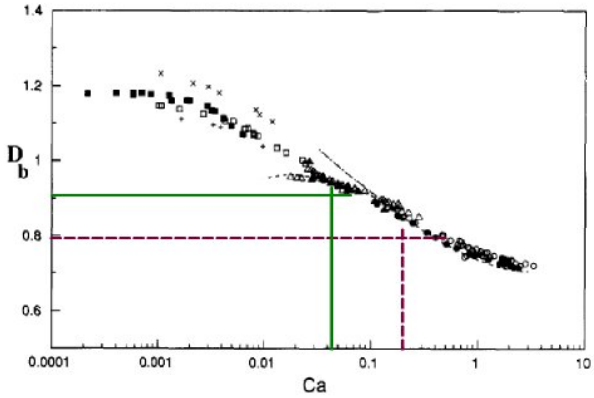

(a)

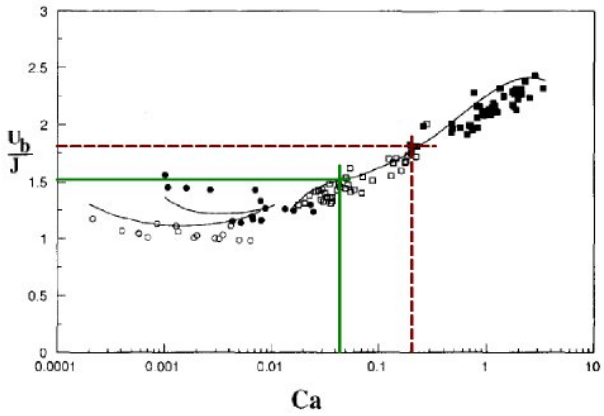

(b)

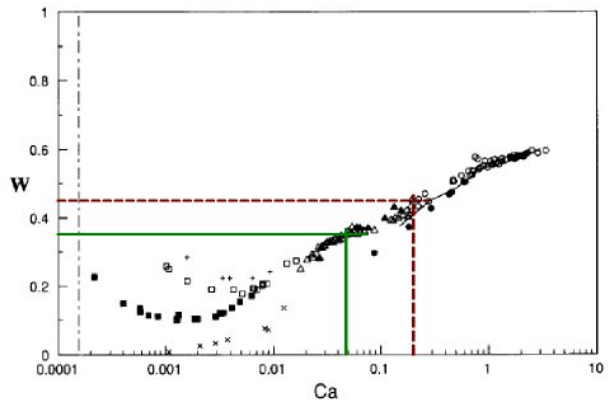

(c)

Fig. 4.7: Comparison of the computed values (Table II) with experimental data from Thulasidas *et al.* [48]: (a) dimensionless bubble diameter; (b) dimensionless bubble velocity; (c) relative bubble velocity. Reproduced from [48]

ratio between the magnitude of viscous effects in the liquid and the capillary effects:

$$\mathtt{Ca} = \frac{\mu^* \mathtt{v}^*}{\sigma^*} \ , \tag{4.23}$$

where the bubble final velocity is used as reference velocity. The values of these parameters obtained from the numerical simulations are given in Table 4.2.

	Ca	D_B/D_h	U_B/J	W
BT1	0.205	0.812	1.80	0.445
BT2	0.043	0.919	1.55	0.355

Tab. 4.2: Computed Capillary number, dimensionless bubble diameter, bubble velocity and relative bubble velocity.

For the dimensionless bubble diameter (Fig. 4.7.a) the computed values are slightly smaller than the measured values. This difference can be explained by the fact that in experiments the bubbles have the length several times the channel width and the diameter is measured in the cylindrical part while in our computations the bubbles are much shorter and can not develop into an elongated Taylor bubble. For the bubble velocity (Fig. 4.7.b) and relative bubble velocity (Fig. 4.7.c) we have a better agreement, the computed values being in the range of the measured data.

4.2 Periodic fully developed heat transfer

In the previous section the channel walls were assumed to be adiabatic and there are no heat sources in the domain. Thus, both fluids have the same constant temperature. In many applications of interest, heat is introduced or removed from the system either by heating/cooling the walls or due to chemical reactions. This results in a nonuniform temperature field which depends on the flow structure and the heat conductivities of each fluid. Except for the special case of the annular flow, the gas distribution varies along the channel and the definition of a fully developed heat transfer as it was introduced in section 3.2.1 can not be used. However, when the fluid flow is periodic and the heating conditions are also periodic, one can extend the concept of fully developed heat transfer and reduce the analysis of the temperature field to an isolated module, in the same way as it is done for the velocity and pressure field.

In this section, the case of an axially periodic wall heat flux will be considered:

$$\lambda \left.\frac{\partial T}{\partial n}\right|_{wall} = q \tag{4.24}$$

which has the same periodicity length (L) as the flow through the channel

$$q(x, y, z) = q(x, y + L, z) = q(x, y + 2L, z) = \dots \tag{4.25}$$

Since the flow is supposed to be (hydrodynamic) periodic developed the velocity and the pressure field are subject to the conditions and relations from section 4.1.

The fact that the wall heat flux $\vec{\mathsf{q}}$ has the same periodicity length as the flow means that the temperature profiles for y, $y+L$, $\dots$ have the same slope at the wall. Thus, the periodic thermally developed regime for prescribed, modularly repeating wall heat transfer can be visualized by considering temperature profiles at a succession of stream-wise positions y, $(y+L)$, $(y+2L)$, $\dots$. These profiles will have identical shape and, for the case of heating, will be displaced one above the other by the same distance:

$$T_\varphi(x, y + L, z) - T_\varphi(x, y, z) = T_\varphi(x, y + L, z) - T_\varphi(x, y + 2L, z) = \dots \qquad \varphi = 1, 2 \tag{4.26a}$$

Similar to the single phase situation, let us define

$$\theta_\varphi(x, y, z) = \frac{T_\varphi(x, y + L, z) - T_\varphi(x, y, z)}{L} \qquad \varphi = 1, 2 \tag{4.26b}$$

and subdivide the temperature field in two components:

$$T_\varphi(x, y, z; t) = y\theta_\varphi(x, y, z; t) + \Theta_\varphi(x, y, z; t) \qquad \varphi = 1, 2 \tag{4.26c}$$

Further on we will refer to θ as linear temperature coefficient and to Θ as the reduced temperature field. For now, θ is assumed to vary both spatially and in time, and it is defined separately for each fluid φ.

The periodic fully developed heat transfer condition (4.26a) implies that θ_φ is periodic in stream-wise direction (y), that is:

$$\theta_\varphi(x, y, z; t) = \theta_\varphi(x, y + L, z; t) = \theta_\varphi(x, y + 2L, z; t) = \dots \qquad \varphi = 1, 2 \tag{4.27}$$

Further, introducing the temperature decomposition (4.26c) in (4.26b) one gets

$$\theta_\varphi(x,y,z;t) = \frac{(y+L)\theta_\varphi(x,y+L,z;t) + \Theta_\varphi(x,y+L,z;t) - [y\theta_\varphi(x,y,z;t) + \Theta_\varphi(x,y,z;t)]}{L}$$

and, taking in account the periodicity of θ

$$\theta_\varphi(x,y,z;t) = \theta_\varphi(x,y,z;t) + \frac{\Theta_\varphi(x,y+L,z;t) - \Theta_\varphi(x,y,z;t)}{L}$$

which implies that the reduced temperature Θ_k is also periodic:

$$\Theta_\varphi(x,y,z;t) = \Theta_\varphi(x,y+L,z;t) = \Theta_\varphi(x,y+2L,z;t) = \ldots \qquad \varphi = 1,2 \tag{4.28}$$

This means that, in case of heat transfer problems subject to (4.26a) the temperature field can be described using two periodic fields, one that takes in account the overall temperature variation along the channel (θ) and the other (Θ) giving the temperature distribution due to the local heating.

4.2.1 Volume-averaged heat convection equation

To derive the volume-averaged equations governing the convective heat transfer for a two-phase flow one can use directly the equation (2.36c) for the mean enthalpy as it was done for single phase case in section 3.2.1, or start from the local enthalpy equations for each phase and apply the averaging technique described in chapter 2. Inhere, the second method is preferred because it allows us to have a better picture about the contributions of θ and Θ to the local heat transfer. Thus, for each fluid φ, in the bulk region, the heat transfer and convection is governed by the local enthalpy equation:

$$\frac{\partial \rho_\varphi h_\varphi}{\partial t} + \nabla \cdot (\rho_\varphi h_\varphi \vec{\mathbf{v}}_\varphi) = \frac{1}{\mathtt{Pe}} \nabla \cdot (\lambda_\varphi \nabla T_\varphi) \tag{4.29}$$

where the contribution of the pressure work and heat dissipation due to viscous forces in the energy balance are neglected because the fluids are assumed to be incompressible (see Section 2.4.1). The energy source term was omitted in (4.29). This has been done for a simpler presentation and because it does not play any role in the development of the method provided that it varies periodically along the channel. Using the decomposition

(4.26c) the previous equation becomes:

$$\frac{\partial \rho_\varphi C_{p,\varphi} \Theta_\varphi}{\partial t} + \nabla \cdot \left(\rho_\varphi C_{p,\varphi} \Theta_\varphi \vec{\mathbf{v}}_\varphi - \frac{1}{\mathtt{Pe}} \lambda_\varphi \nabla \Theta_\varphi \right) = -\rho_\varphi v_\varphi \theta_\varphi + \frac{2}{\mathtt{Pe}} \lambda_\varphi \frac{\partial \theta_\varphi}{\partial y} - y \left[\frac{\partial \rho_\varphi C_{p,\varphi} \theta_\varphi}{\partial t} + \nabla \cdot \left(\rho_\varphi C_{p,\varphi} \theta_\varphi \vec{\mathbf{v}}_\varphi - \frac{1}{\mathtt{Pe}} \lambda_\varphi \nabla \theta_\varphi \right) \right] \quad (4.30)$$

Since all the quantities and the fluid properties in the equation above are periodic in y with the same periodicity length the last term in (4.30) has to be equal to zero:

$$\frac{\partial \rho_\varphi C_{p,\varphi} \theta_\varphi}{\partial t} + \nabla \cdot \left(\rho_\varphi C_{p,\varphi} \theta_\varphi \vec{\mathbf{v}}_\varphi - \frac{1}{\mathtt{Pe}} \lambda_\varphi \nabla \theta_\varphi \right) = 0 \qquad \varphi = 1, 2 \quad (4.31)$$

This represents the advection-diffusion equation for θ_φ. It depends only on the flow characteristics and there is no dependence on the reduced temperature Θ_φ.

The equation for the reduced enthalpy $C_{p,\varphi}\Theta_\varphi$ is then

$$\frac{\partial \rho_\varphi C_{p,\varphi} \Theta_\varphi}{\partial t} + \nabla \cdot \left(\rho_\varphi C_{p,\varphi} \Theta_\varphi \vec{\mathbf{v}}_\varphi - \frac{1}{\mathtt{Pe}} \lambda_\varphi \nabla \Theta_\varphi \right) = -\rho_\varphi C_{p,\varphi} v_\varphi \theta_\varphi + \frac{2}{\mathtt{Pe}} \lambda_\varphi \frac{\partial \theta_\varphi}{\partial y} \qquad \varphi = 1, 2 \quad (4.32)$$

Note that compared with the single phase equation (3.48) an additional term due to the spatial variation of θ appears.

Interface jump conditions

To describe the behavior of the new quantities at the interface, jump conditions has to be specified. For a two-phase system with reversible heat transfer at the interface the temperature is continuous over the interface (see 2.1.4), that is:

$$T_{1i} = T_{2i} \quad (4.33)$$

Using the definition for the linear temperature coefficient and the fact that the flow is spatially periodic, it implies that θ is also continuous:

$$\theta_{1i} = \theta_{2i} \quad (4.34)$$

Introducing the temperature decomposition (4.26c) in (4.33) and using the jump relation (4.34) the jump condition for the reduced temperature is:

$$\Theta_{1i} = \Theta_{2i} \tag{4.35}$$

which means that both θ and Θ fields are continuous in all the computational domain, the same as the temperature.

For the heat transfer problems, a second jump condition concerning the interface heat fluxes exists. Using the Fourier law to express the heat flux, the jump condition (2.41) becomes

$$-\lambda_1 \left.\frac{\partial T}{\partial n}\right|_{1i} + \lambda_2 \left.\frac{\partial T}{\partial n}\right|_{2i} = 0 \tag{4.36a}$$

Since the flow is periodic it means that if (x_i, y_i, z_i) is a point on the interface separating the two fluids, the point $(x_i, y_i + L, z_i)$ is also an interface point and the jump condition (4.36a) applies. Thus, for the linear temperature coefficient one has:

$$\begin{aligned}
\lambda_1 \left.\frac{\partial \theta_1}{\partial n}\right|_{(x_i,y_i,z_i)} &= \frac{1}{L}\left[\lambda_1 \left.\frac{\partial T_1}{\partial n}\right|_{(x_i,y_i+L,z_i)} - \lambda_1 \left.\frac{\partial T_1}{\partial n}\right|_{(x_i,y_i,z_i)}\right] \\
&= \frac{1}{L}\left[\lambda_2 \left.\frac{\partial T_2}{\partial n}\right|_{(x_i,y_i+L,z_i)} - \lambda_2 \left.\frac{\partial T_2}{\partial n}\right|_{(x_i,y_i,z_i)}\right] \\
&= \lambda_2 \left.\frac{\partial \theta_2}{\partial n}\right|_{(x_i,y_i,z_i)}
\end{aligned} \tag{4.36b}$$

The interface jump condition for the flux of the reduced temperature can be obtained introducing the decomposition (4.26c) in (4.36a). Using this procedure and taking in account the jump condition (4.36b) one has:

$$\lambda_1 \left.\frac{\partial \Theta}{\partial n}\right|_{1i} + \lambda_1 \theta_{1i} \vec{\mathsf{e}}_y \cdot \vec{\mathsf{n}} = \lambda_2 \left.\frac{\partial \Theta}{\partial n}\right|_{2i} + \lambda_2 \theta_{2i} \vec{\mathsf{e}}_y \cdot \vec{\mathsf{n}} \tag{4.36c}$$

One can see that the flux for θ across the interface is continuous while in the case of the reduced temperature Θ a supplementary term appears.

Boundary conditions

In order to have a complete system, the boundary conditions have to be specified. Since the flow and the heat transfer are fully developed, for stream-wise direction periodic boundary conditions for both θ and Θ are imposed.

For the other two directions the channel is bounded by straight walls. Using the definition for θ and the fact that the wall heat flux is periodic one gets:

$$\begin{aligned}\lambda_1 \left.\frac{\partial \theta_1}{\partial n}\right|_{wall} &= \lambda_1 \left.\frac{\partial T_1(x, y+L, z)}{\partial n}\right|_{wall} - \lambda \left.\frac{\partial T_1(x, y, z)}{\partial n}\right|_{wall} \\ &= q(x, y+L, z) - q(x, y, z) = 0 \end{aligned} \tag{4.37}$$

which means that the linear temperature coefficient obeys an adiabatic wall boundary condition.

For the reduced temperature, since the walls are parallel to the flow direction, one has:

$$\lambda \left.\frac{\partial \Theta}{\partial n}\right|_{wall} = \lambda \left.\frac{\partial T}{\partial n}\right|_{wall} - y\lambda \left.\frac{\partial \theta}{\partial n}\right|_{wall} = q \tag{4.38}$$

where, n denotes the direction normal to the wall, i.e. either x or z. Note that the temperature T and the reduced temperature Θ have the same wall boundary condition.

The equation (4.31) together with the boundary conditions (4.37) and the jump relations (4.34) and (4.36b) indicate that for the linear temperature coefficient one has the same type of problem as for the temperature in an adiabatic flow, that is θ is constant both in time and space.

Volume-averaged equation for the reduced temperature

The volume-averaged heat convection equation for the reduced enthalpy can be obtained applying the averaging operator (2.10) to the local equations (4.32) for a fixed control volume Ω with rigid boundaries and following the same steps as in Chapter 3 for the energy equation. Since θ is constant the last term in (4.32) vanishes and the equation is

$$\frac{\partial}{\partial t}\langle \rho C_p \Theta \rangle + \nabla \cdot \left(\langle \rho C_p \Theta \vec{\mathsf{v}} \rangle - \frac{1}{\mathsf{Pe}} \langle \lambda \nabla \Theta \rangle \right) = -\langle \rho C_p v \rangle \theta - \frac{1}{\mathsf{Pe}} (\lambda_1 - \lambda_2) \theta \frac{1}{V} \int\limits_{S_i} \vec{\mathsf{e}}_y \cdot \vec{\mathsf{n}} \, dS \tag{4.39}$$

The last term in (4.39) appears because of the interface heat flux jump condition (4.36c).

This new equation differs from the enthalpy equation (3.1) only by two source terms which do not depend on Θ and, therefore, the numerical procedure introduced in Chapter 3 can be used to approximate the l.h.s. of the equation.

Linear temperature coefficient

To find the value of θ one can integrate the equation (4.32) over the entire computational domain $\Omega = [0, L_x] \times [0, L] \times [0, L_z]$:

$$\begin{aligned}\frac{\partial}{\partial t}\sum_{\varphi=1,2}\int_V \rho_\varphi C_{p,\varphi}\Theta_\varphi X_\varphi \, dV + \sum_{\varphi=1,2}\left(\int_{S_L} \rho_\varphi C_{p,\varphi}\Theta_\varphi v_\varphi X_\varphi \, dS - \int_{S_0} \rho_\varphi C_{p,\varphi}\Theta_\varphi v_\varphi X_\varphi \, dS\right) \\ - \frac{1}{\mathtt{Pe}}\sum_{\varphi=1,2}\left(\int_{S_L} \lambda_\varphi \frac{\partial \Theta_\varphi}{\partial y} X_\varphi \, dS - \int_{S_0} \lambda_\varphi \frac{\partial \Theta_\varphi}{\partial y} X_\varphi \, dS\right) \\ = \frac{1}{\mathtt{Pe}}\frac{Q}{L} - \theta \sum_{\varphi=1,2}\int_V \rho_\varphi C_{p,\varphi} v_\varphi X_\varphi \, dV - \theta(\lambda_1 - \lambda_2)\int_{S_i} \vec{\mathsf{e}}_y \cdot \vec{\mathsf{n}} \, dS \end{aligned} \quad (4.40)$$

where, S_0 and S_L designate the inflow and, respectively, the outflow cross sections, V is the volume of Ω, Q is the rate of heat addition through the channel walls given by (3.47), and S_i is the interface separating the two fluids. Since the heat transfer is fully developed and all the quantities are periodic in stream-wise direction all the terms on the l.h.s. of the equation are zero. Also, S_i can be considered as a closed surface as the bubbles along the channels have the same shape which means that the last term in the equation cancels itself. Thus, for θ one has

$$\theta = \frac{1}{\mathtt{Pe}} \frac{Q}{L \sum_{\varphi=1,2}\int_V \rho_\varphi C_{p,\varphi} v_\varphi X_\varphi \, dV} \quad (4.41)$$

Comparing this expression with (3.45) giving the temperature coefficient for the single phase one can see that they are similar.

4.2.2 Bubble-train flow in a channel with a prescribed axial wall heat flux

Let us apply now the method described above to compute the temperature field corresponding to the bubble-train flow simulated in section 4.1.2 when an uniform heat flux is

imposed at the channel walls. Inhere, the fully developed regime corresponding to `BT2` case is chosen as base flow.

For this numerical simulation we take a specific heat capacity ratio of $C_{p,2}/C_{p,1} = 0.2401$ and a thermal conductivity ratio of $\lambda_2/\lambda_1 = 0.0451$. The Prandtl number for the liquid is $\mathrm{Pr} = 2.34$ which means that the the gas has $\mathrm{Pr} = 0.5$. These values correspond to an air-water system at $T = 350$ K.

The time step used for this numerical computation is $\Delta t = 10^{-4}$, the same as for the simulation of the adiabatic case. The maximum value given by the time step criteria (3.33) is $\Delta t_0 = 1.3 \times 10^{-4}$. To reduce the oscillations of the solution near the interface an upwind scheme is preferred to approximate the conductive terms.

At time $t = 0$ both fluids are assumed to have the same temperature. The fully developed regime is considered as established when a balance between the heat introduced into the system due to wall heating and the heat removed due to streamwise convection occurs. This can be expressed quantitatively by the value of the domain mixture reduced temperature:

$$\Theta_V = \frac{\displaystyle\sum_{\varphi=1,2} \int_0^{L_x}\int_0^{L}\int_0^{L_z} \rho_\varphi C_{p,\varphi} \Theta_\varphi X_\varphi \, dx\, dy\, dz}{\displaystyle\sum_{\varphi=1,2} \int_0^{L_x}\int_0^{L}\int_0^{L_z} \rho_\varphi C_{p,\varphi} X_\varphi \, dx\, dy\, dz}$$

In Figure 4.8 the time variations of the domain mixture reduced temperature and, respectively, mixture temperature are presented. While the last one is almost constant indicating that the fully developed heat transfer has been reached since its variations being of the same order of magnitude with the numerical rounding performed in `TURBIT-VoF`, the volume mixture temperature

$$T_V = \frac{\displaystyle\sum_{\varphi=1,2} \int_0^{L_x}\int_0^{L}\int_0^{L_z} \rho_\varphi C_{p,\varphi} T_\varphi X_\varphi \, dx\, dy\, dz}{\displaystyle\sum_{\varphi=1,2} \int_0^{L_x}\int_0^{L}\int_0^{L_z} \rho_\varphi C_{p,\varphi} X_\varphi \, dx\, dy\, dz}$$

has an oscillatory behavior. This can be explained by the fact that cold bubbles enter the domain but, as they move along the channel, the gas gets warmer by conduction in the vicinity of the walls and due to recirculation inside the bubble. As the bubble moves out of the fluid cell an other cold bubble enters the domain determining a decrease of the overall

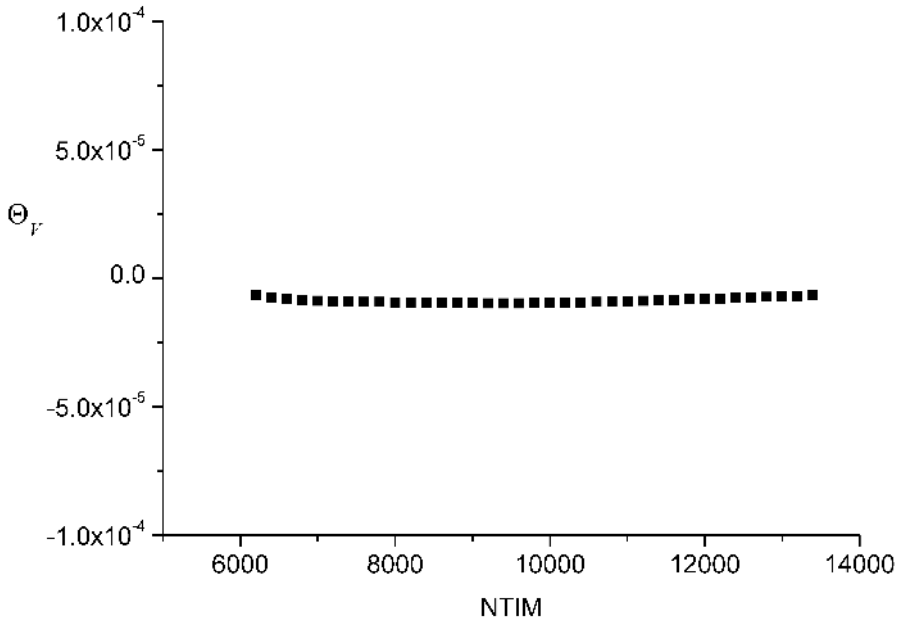

(a)

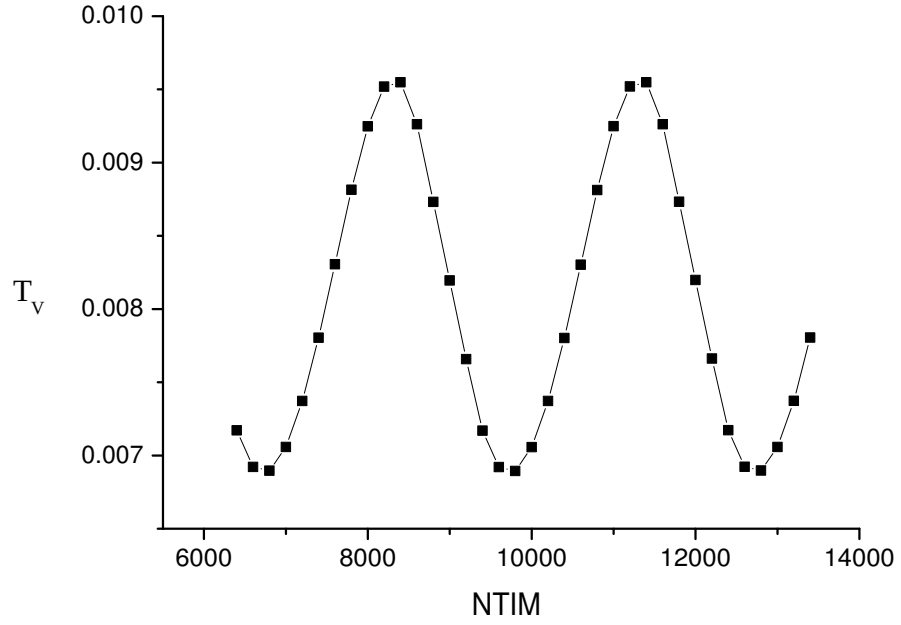

(b)

Fig. 4.8: Time variation of the mixture reduced temperature (a) and mixture temperature (b) for the entire unit cell.

temperature of the system.

In Figure 4.9 the structure of the temperature field inside the bubble and in the liquid slug is visualized. The presence of the gas in the channel modifies the temperature field corresponding to single phase heat convection simulated in section 3.2.1. The isothermal lines show that gas has higher temperature in the region where the bubble interface is closer to the walls. However, moving towards the center of the channel the temperature decreases slower in the bubble than it does in the liquid phase. Since the heat conductivity of the gas is lower than the one corresponding to the liquid the only explanation for this behavior is the strong recirculation inside the bubble (Figure 4.5) which transports the hotter gas near the interface towards the center of the bubble. For the liquid slug this mixing effect is smaller and there is a region in the center of the channel where the liquid remains colder. This can be observed also comparing the temperature field in two cross-sections, one through the liquid slug (Fig. 4.10(a)) and the other at the position, along the channel, where the bubble has the largest diameter (Fig. 4.10(b)). In these figures the temperature isolines are represented using the same number of iso-levels between the maximum and the minimum temperature. These limits are computed for the whole domain therefore one can directly correlate the magnitude of the temperature gradient with the density of the isolines. Thus, in the slug one can identify a region with large temperature gradients making the transition from the higher temperature in the corners of the channel to the lower temperature in the central region. In the cross-sections where the bubble is present the temperature gradients are larger in the liquid layer surrounding the interface at the corners of the channel. Inside the bubble the gradient is much smaller because of the heat convection due to inner recirculation.

An other interesting aspect about the transverse temperature distribution is the direction of the temperature gradients. For the single phase heat convection problem, when the flow is laminar, the heat transfer is done only by conduction in the direction perpendicular to the wall. The temperature isolines are, in this case, concentric circles and the temperature gradient points toward the center of the channel (see Fig. 4.11). For the bubble train flow, the isolines pattern changes. Because of the lateral movement of the liquid induced by the passage of the bubbles, a part of the heat from the middle of the wall is transported towards the channel corners. In the liquid slug (see Fig. 4.10(a)), looking along a diagonal, the isolines are first concentric arcs with the center in the corner of the channel. Moving towards the center of the channel, there is a region where the temperature is constant in

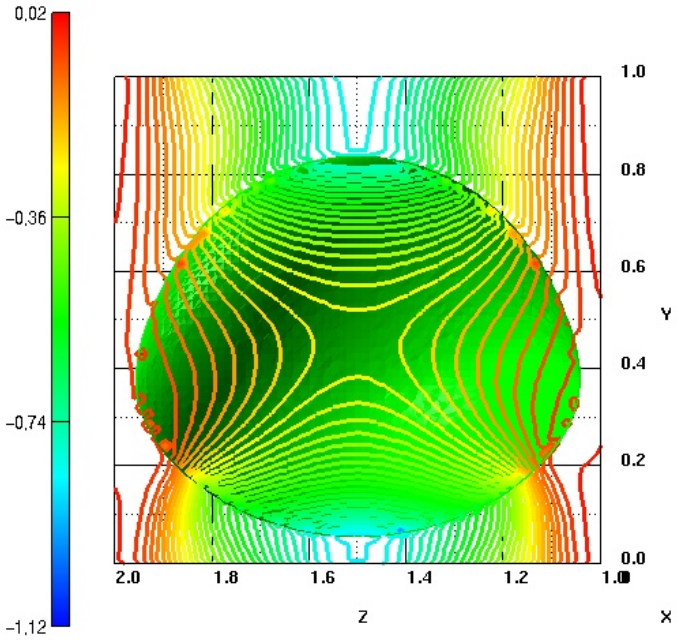

(a) NTIM=11800

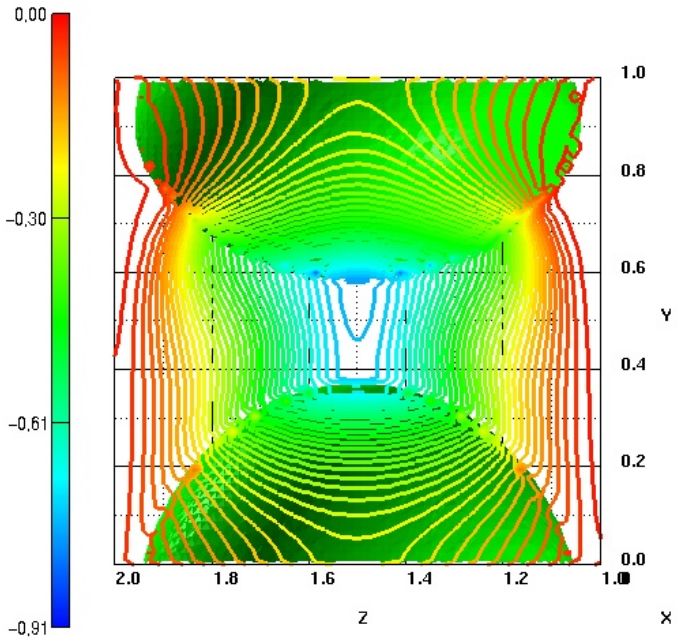

(b) NTIM=13400

Fig. 4.9: Temperature field in a longitudinal plane containing the channel axis for two different instants in time.

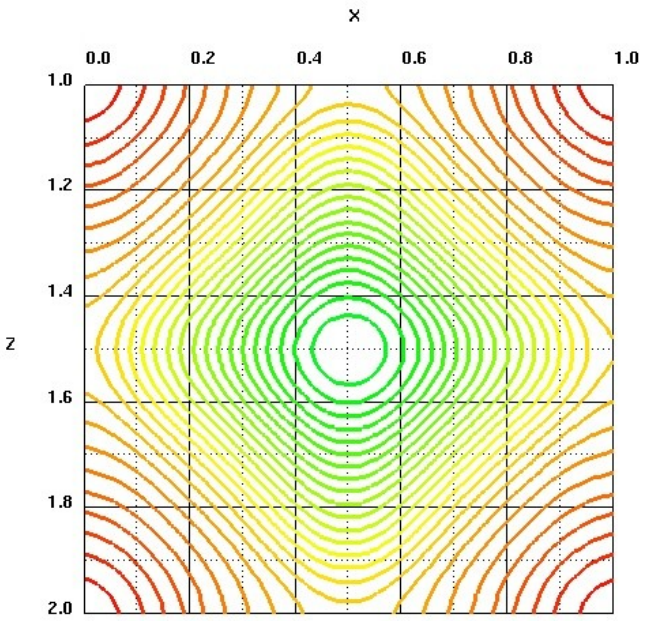

(a) Through the slug slug

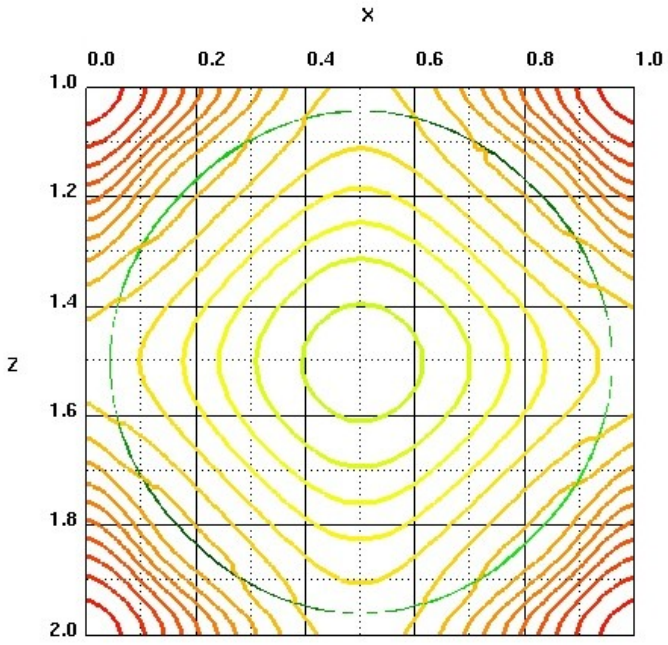

(b) Through the bubble

Fig. 4.10: Structure of the temperature field in a transversal plane at NTIM=11400.

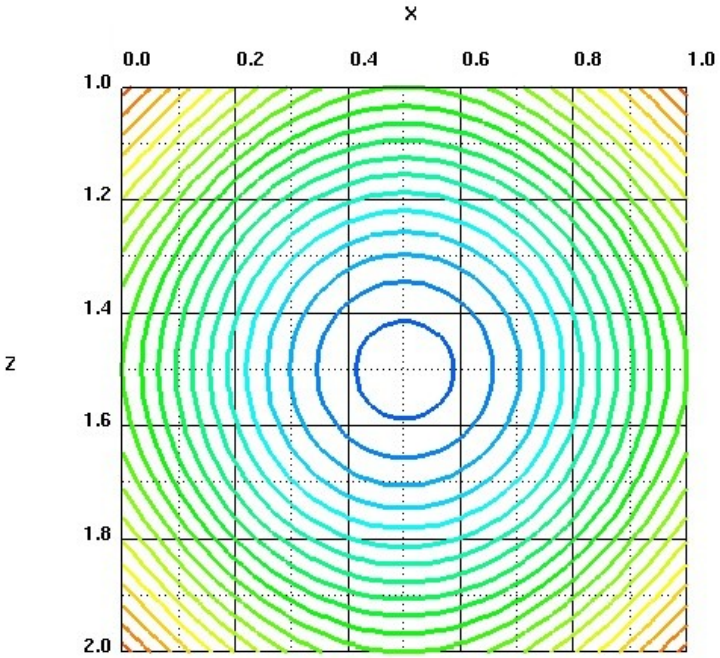

Fig. 4.11: Structure of the temperature field in a transversal plane for a laminar single phase flow.

the direction perpendicular to the diagonal while, close to the center the isolines form concentric circles. The same picture holds in a cross-section through the bubble, the isolines being slightly deformed due to the presence of the interface (see Fig. 4.10(b)). This pattern suggests that, compared to the single phase situation, the heat transfer improves in the middle part of the wall while it diminishes in the corners of the channel. This observation is confirmed by comparing the normalized maximum and minimum wall temperatures given by Eq. (3.51) with the corresponding values for the single phase flow. In Figure 4.12 the variation along the channel for $T^*_{w,max}$ (Fig. 4.12(a)) and $T^*_{w,min}$ (Fig. 4.12(b)) are presented. Two different time steps were considered: one (NTIM=11400) corresponding to the moment when the mixture temperature of the unit cell is close to its maximum value and the other one (NTIM=12600) close to its minimum value. The values of $T^*_{w,max}$ and $T^*_{w,min}$ for the single phase are represented with continuous line. From this figures one can see that the normalized maximum wall temperature, which corresponds to the temperature in the corner, is always larger in the case of bubble-train flow than when the single phase flow is considered. For the normalized minimum wall temperature, corresponding to the

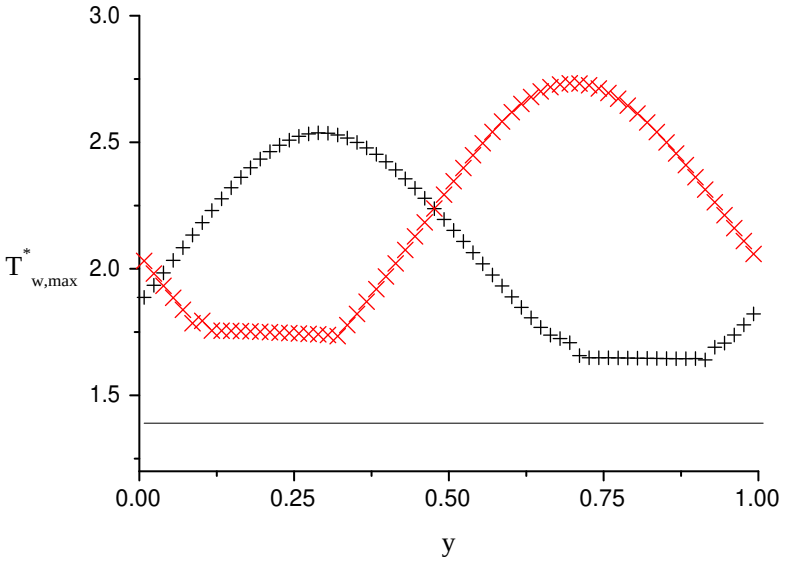

(a)

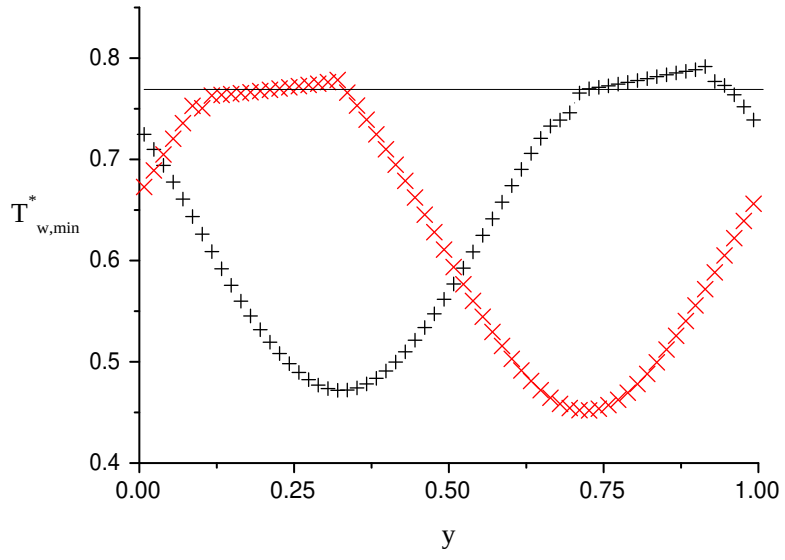

(b)

Fig. 4.12: Normalized maximum and minimum wall temperature variation along the channel for two different time-steps: (+): NTIM=11400; (×): NTIM=12600; continuous line: single phase flow.

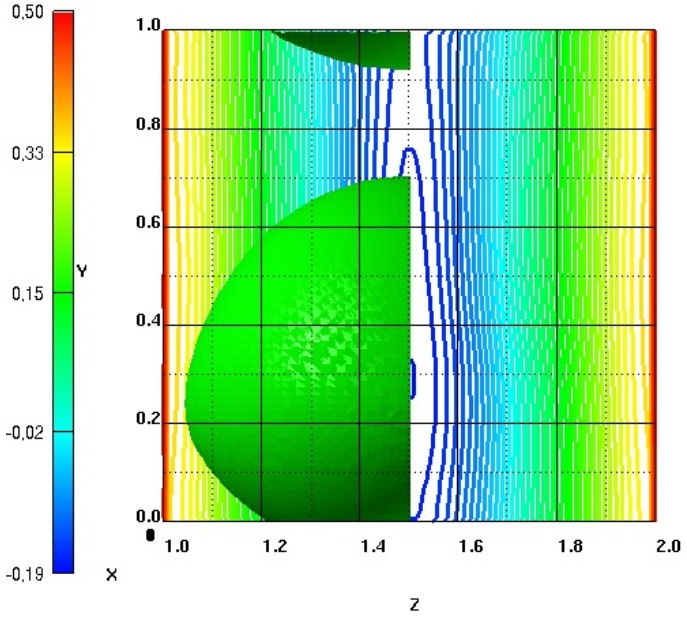

(a) NTIM=11400

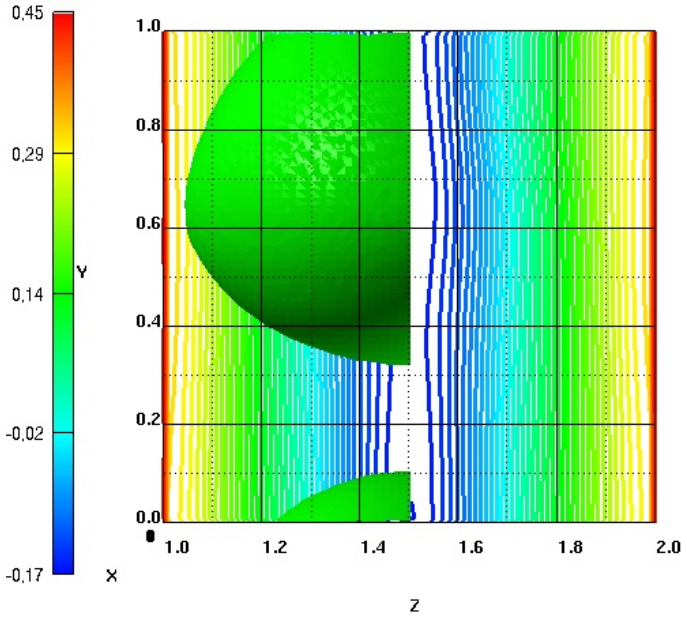

(b) NTIM=12600

Fig. 4.13: Wall temperature isolines two different time steps.

temperature in the middle of the wall, the values for bubbly flow are relatively close to the single phase value in the region of the liquid slug and smaller in rest. For easy reference the position of the bubble and temperature isolines at the wall are given in Figure 4.13.

Unfortunately, there are no experimental results available in the literature in order to validate our computations. Because of the small cross-sectional dimensions of the channel the temperature profiles can not be measured. The available experiments [50] regarding mass/heat transfer in capillaries study only the dispersion during bubble-train flow by measuring the concentration or a specific substance (marker) at the outlet. Since the marker is injected only in one slug the periodicity condition is not fulfilled. To analyze the characteristics of a periodic fully developed heat/mass transfer an experiment using infrared temperature measurements should be performed in order to obtain data regarding the wall temperatures and compare it with the computed wall temperature. Also, Laser Induced Fluorescence methods could be used to visualize the temperature fields inside the channel.

5. SUMMARY AND CONCLUSIONS

This work has highlighted the development of a new numerical method to describe the flow and heat transfer characteristics of a gas-liquid two-phase flow in channels with hydraulic diameter of the order of 1 mm and its implementation in the computer code `TURBIT-VoF`. Particular emphasis have been given to the modeling of steady periodic slug flows in rectangular channels with prescribed wall heat flux.

To account for heat transfer an energy equation has been implemented. Using a volume-averaging method the enthalpy equation for a two-components system have been deduced. Interfacial source terms for surface tension effects, interphase mass and heat transfer have also been included. For the case when the components can be considered as incompressible and there is no phase change at the interface, a simplified energy equation is derived.

The numerical method for the discretization of the energy equation is also discussed. The volume-averaged form of the equation suggests that a finite volume numerical method should be used. Due to low influence of buoyancy effects on the flows in small channels, the momentum equation is supposed to be independent from the energy equation. Therefore, first the fluids distribution and the velocity field were computed; then the enthalpy distribution was determined. To ensure a better numerical approximation of the pressure jump at the interface, a new form for the pressure equation was constructed using a procedure that ensures the consistency between the gradient and divergence discrete operators. For the energy equation, special care has been taken when the convective term are approximated. Due to a new upwinding procedure, the instabilities near the interface are avoided. Tests for the fully developed heat transfer regime for a single phase flow in a rectangular channel have been performed. Both air and water flows were considered. The computed Nusselt numbers match well the values available in literature in within an error of 0.6%.

For spatially periodic two-phase flows in small channels a new concept to model convective heat transfer has been introduced. This new concept, called *periodic fully developed flow*, is an extension for periodic multiphase flow of a model for single phase flows in chan-

nels with variable cross-section (see Patankar [36]). Based on the periodical characteristics of the velocity components and reduced pressure, the flow field analysis can be confined to a single isolated module. A similar analysis is done for the enthalpy field, but the periodicity conditions are of a different nature. For prescribed stream-wise periodic wall heat flux the enthalpy itself is periodic, provided that a linear term related to the bulk enthalpy change is subtracted.

Using this method, the bubble-train flow along a square channel has been simulated. For the adiabatic case, two simulation runs resulting in two different values of the Capillary number ($Ca_B = 0.205$ and $Ca_B = 0.043$) are compared. For both cases computed global flow parameters agree well with available experimental data. The results for the bubble shape, flow structure within the bubble, and flow structure in the liquid slug are analyzed in detail. The comparison reveals the important role of the Capillary number as the main physical control parameter for two-phase flow in small channels. The decrease of the Capillary number only by a factor of 5 is associated with the thinning of the liquid film, the appearance of a second vortex in the bubble, the enhancement of non-axisymmetry of the flow inside the bubble, and the appearance of a vortex in the liquid slug. This corresponds, on one side, with a better separation of the flows between adjacent slugs (plug effect) while, on the other side, it intensifies the mixing characteristics in each individual slug.

When an uniform wall heat flux is considered, the temperature distribution inside the channel could be computed up to an arbitrary constant. Both axial, and transverse temperature variation could be analyzed, and the changes due to the presence of the gas bubble could be studied. Thus, in the liquid, an improvement of the heat transfer in the middle of the channel faces could be observed due to the liquid movements toward the channel corners where a decrease of the heat transfer characteristics could be seen. Inside the gas bubbles the strong mixing has the tendency to reduce temperature gradients.

These results show that this new method is a valuable tool for the numerical analysis of spatially periodic two-phase flows in channels with or without heat transfer. Using global quantities as input parameters the method allows the reconstruction of the local flow or temperature field. For low mass fluxes the temperature-mass analogy can be also used to compute the local concentrations of different species in the channel. Here it is referred to the chemical substance that are passively transported by the flow. When chemical reactions take place and new products are generated an extension of the actual version of the code has to be done in order to account for these phenomena.

This numerical method is, however, restricted to spatially periodic flows only. This limitation is quite severe when heat transfer is concerned. When phenomena like phase change at the interface or exothermal reactions between reactants transported by the flow occur, the heat exchange depends strongly on local temperature and can not be regarded as periodic anymore. To extend the applicability of the code for more general cases the introduction of inflow and outflow boundary conditions is mandatory. The absence of experiments from the literature, that could be used to validate the results for heat transfer, represents, also, a sensible point of this work. Therefore future experiments to verify the numerical results measurements of wall temperature or temperature profiles inside the channel should be performed.

BIBLIOGRAPHY

[1] M. Behnia and G. de Vahl Davis, *Fine mesh solutions using stream function-vorticity formulation*, Notes on Numerical Fluid Mechanics (B. Roux, ed.), vol. 27, Vieweg Verlag, Braunschweig, 1990, pp. 11–18. [46, 47]

[2] L. Chen, S.V. Garimella, J.A. Reizes, and E. Leonardi, *Motion of interacting gas bubbles in a viscous liquid including wall effects and evaporation*, Numerical Heat Transfer, A **31** (1997), 629–654. [3]

[3] R. Clift, J.R. Grace, and M.E. Weber, *Bubbles, drops and particles*, Academic Press, 1978. [3]

[4] M.R. Davidson and M. Rudman, *Volume-of-fluid calculation of heat or mass transfer across deforming interfaces in two-fluid flow*, Numer Heat Transfer Part B Fundam **41** (2002), 291–308. [3]

[5] J.M. Delhaye, *Jump conditions and entropy sources in two–phase systems. Local instant formulation*, Int J Multiphase Flow **1** (1974), 395–409. [5, 7, 8]

[6] D. A. Drew and S.L. Passman, *Theory of multicomponent fluids*, Springer–Verlag, 1999. [7, 9, 12]

[7] W. Ehrfeld, V. Hessel, and H. Löwe, *Microreactors: New technology for modern chemistry*, Wiley-VCH, Weinheim, 2000. [1, 3]

[8] J.H. Ferziger and M. Perić, *Computational methods for fluid dynamics*, Springer, 1996. [43, 56]

[9] M. Gad-el Hak, *The fluid mechanics of microdevices – the freeman scholar lectures*, J Fluids Eng Trans ASME **121** (1999), 5–33. [6]

[10] R. Gatignol, *Asymptotic modeling of fluid–fluid interfaces*, Dynamics of Multiphase Flows Across Interfaces (A. Steinchen, ed.), Springer–Verlag, 1996, pp. 15–27. [7, 8]

[11] S.M. Ghiaasiaan and S.I. Abdel-Khalik, *Two-phase flow in microchannels*, Advances in heat transfer, vol. 34, Academic Press, 2001, pp. 145–254. [2]

[12] S. Gottlieb and C.-W. Shu, *Total variation dimishing Runge-Kutta schemes*, Mathematics of Computation **67** (1998), no. 221, 73–85. [31, 32]

[13] D.D. Gray and A. Giorgini, *The validity of the Boussinesq approximation for liquids and gases*, Int J Heat Mass Transfer **19** (1976), 545–551. [43]

[14] J.E. Hart, *Low prandtl-number convection between differentially heated end walls*, Int J Heat Mass Transfer **26** (1983), 1069–1074. [46]

[15] V. Haverkamp, G. Emig, V. Hessel, M.A. Liauw, and H. Löwe, *Characterization of a gas/liquid microreactor, the micro bubble column: determination of specific interfacial area*, Microreaction Technology, IMRET-5: Proc. Fifth Int. Conf. on Microreaction Technology (M. Matlosz, W. Ehrfeld, and J.P. Baselt, eds.), Springer, 2002, pp. 203–214. [1, 3]

[16] G. Hetsroni, *Handbook of multiphase systems*, McGraw–Hill, 1982. [13]

[17] A. Huang and D.D. Joseph, *Instability of the equilibrium of a liquid below its vapor between horizontal heated plates*, J Fluid Mech **242** (1992), 235–247. [13]

[18] A. Huang and D.D. Joseph, *Stability of liquid–vapor flow down an inclined channel with phase change*, Int J Heat Mass Transfer **36** (1993), no. 3, 663–672. [13]

[19] D.T.J. Hurle, E. Jakemen, and C.P. Johnson, *Convective temperature oscillations in molten gallium*, J Fluid Mech **64** (1974), 565–576. [46]

[20] M. Ishii, *Thermo–fluid dynamic theory of two–phase flow*, 1975. [5, 7, 9, 12, 13, 15]

[21] K.F. Jensen, *Microreaction engineering – is small better?*, Chem Eng Sci **56** (2001), 293–303. [1]

[22] N. Jongen, M. Donnet, P. Bowen, J. Lemaître, H. Hofmann, R. Schenk, C. Hofmann, M. M. Viviani, M.T. Buscaglia, V. Buscaglia, P. Herguijuela, *Development of a continuous segmented flow tubular reactor and the s̈cale-outc̈oncept - in search of perfect powders*, Chem. Eng. Technol. **26** (2003), 3003–305. [1]

[23] D. Juric and G. Tryggvason, *Computations of boiling flows*, Int J Multiphase Flow **24** (1998), no. 3, 387–410. [9]

[24] I. Kataoka, *Local instant formulation of two–phase flow*, Int J Multiphase Flow **12** (1986), no. 5, 745–758. [5, 6, 7]

[25] M. Kaviany, *Principles of heat transfer in porous media, 2nd ed.*, Springer–Verlag, 1995. [25]

[26] Peter A. Kew and Keith Cornwell, *Confined bubble flow and boiling in narrow spaces*, Proc. 10^{th} Int. Heat Transfer Conf. (Brighton), 1994, pp. 473–478. [3]

[27] A.A. Klinghoffer, R.L. Cerro, and M.A. Abraham, *Influence of flow properties on the performance of the monolith froth reactor for catalytic wet oxidation of acetic acid*, Ind Eng Chem Res **37** (1998), 1203–1210. [3]

[28] D.A. Knoll, D.B. Kothe, and B. Lally, *A new non linear solution method for phase change problems*, Tech. report, LA–UR–98–2350, 1998. [2, 16]

[29] W.B. Kolb and R.L. Cerro, *Film flow in the space between a circular bubble and a square tube*, Journal of Colloid and Interface Science **159** (1993), 302–311. [2]

[30] W.B. Kolb and R.L. Cerro, *The motion of long bubbles in tubes of square cross section*, Phys. Fluids A **5** (1993), no. 7, 1549–1557. [2]

[31] D.B. Kothe, W.J. Rider, S.J. Mosso, and J.S. Brock, *Volume tracking of interfaces having surface tension in two and three dimensions*, Tech. report, LA–UR–96–0088, 1996. [16]

[32] S.M. Marco and L.S. Han, *A note on limiting laminar Nusselt number in ducts with constant temperature gradient by analogy to thin-plate theory*, Trans. ASME **77** (1955), 625–630. [36]

[33] R.L. Panton, *Incompressible flow*, second ed., Wiley-Interscience, 1996. [6]

[34] M. Pasandideh-Fard, R. Bhola, S. Chandra, and J. Mostaghimi, *Deposition of tin droplets on a steel plate: simulations and experiments*, Int J Heat Mass Transfer **41** (1998), 2929–2945. [2]

[35] S.V. Patankar, *Numerical heat transfer and fluid flow*, Series in Computational and Physical Processes in Mechanics and Thermal Science, Taylor & Francis, 1980. [29, 33, 34]

[36] S.V. Patankar, C.H. Liu, and E.M. Sparrow, *Fully developed flow and heat transfer in ducts having streamwise-periodic variations of cross-sectional area*, Journal of Heat Transfer **99** (1977), 180–186. [40, 84]

[37] S. Popinet and S. Zaleski, *A front tracking algorithm for accurate representation of surface tension*, International Journal for Numerical Methods in Fluids **30** (1999), no. 6, 775–793. [58, 59, 60]

[38] W. Sabisch, *Dreidimensionale numerische Simulation der Dynamik von aufsteigenden Einzelblasen und Blasenschwärmen mit einer Volume of Fluid Methode*, Ph.D. thesis, Universität Karlsruhe (TH), 2000, FZKA 6478. [3, 5, 12, 23, 31, 55, 95]

[39] W. Sabisch, M. Wörner, G. Grötzbach, and D.G. Cacuci, *3D volume-of-fluid simulation of a wobbling bubble in a gas-liquid system of low Morton number*, New-Orleans, Louisiana, U.S.A., May 27 - June 1 2001, paper 244. [23]

[40] S.S. Sadhal, P.S. Ayyaswamy, and J.N. Chung, *Transport phenomena with drops and bubbles*, Springer, 1997. [18]

[41] K. Schubert, J. Brandner, M. Fichtner, G. Linder, U. Schygulla, and A. Wenka, *Microstructure devices for applications in thermal and chemical engineering*, Microscale Thermophysical Engineering **5** (2001), 17–39. [1]

[42] U. Schumann, *Ein Verfahren zur direkten numerischen Simulation turbulenter Strömungen in Platten- und Ringspaltkanälen und über seine Anwendung zur Untersuchung von Turbulenzmodellen*, Ph.D. thesis, Universität Karlsruhe (TH), 1973, KfK 1854. [25]

[43] A. Serizawa, Z. Feng, and Z. Kawar, *Two-phase flow in microchannels*, Exp. Thermal Fluid Sci. **26** (2002). [2]

[44] R.K. Shah and A.L. London, *Laminar flow forced convection in ducts*, Advances in heat transfer, Academic Press, 1978, Suppliment I. [vii, 41, 42]

[45] C.-W. Shu, *Essentially Non-Oscillatory and Weighted Essentially Non-Oscillatory schemes for hyperbolic conservation laws*, Report 97–65, ICASE, 1997. [32, 96, 98]

[46] C.-W. Shu and S. Osher, *Efficient implementation of essentially non-oscillatory shock-capturing schemes*, J. Comput. Phys. **77** (1988), 439–471. [31, 32]

[47] E.M. Sparrow and S.V. Patankar, *Relationship among boundary conditions and Nusselt numbers for thermally developed duct flows*, Journal of Heat Transfer **99** (1977), 483–485, Technical notes. [39]

[48] T.C. Thulasidas, M.A. Abraham, and R.L: Cerro, *Bubble-train flow in capillaries of circular and square cross section*, Chem Eng Sci **50** (1995), no. 2, 183–199. [x, 2, 51, 61, 63, 66]

[49] T.C. Thulasidas, M.A. Abraham, and R.L: Cerro, *Flow patterns in liquid slugs during bubble-train flow inside capillaries*, Chem Eng Sci **52** (1997), no. 17, 2947–2962. [2, 51]

[50] T.C. Thulasidas, M.A. Abraham, and R.L. Cerro, *Dispersion during bubble-train flow in capillaries*, Chem. Eng. Sci. **54** (1999), 61–67. [82]

[51] K.A. Triplett, S.M. Ghiaasiaan, S.I. Abdel-Khalik, A. LeMouel, and B.N. McCord, *Gas-liquid two-phase flow in microchannels: Part ii: void fraction and pressure drop*, Int J Multiphase Flow **25** (1999), 395–410. [2]

[52] K.A. Triplett, S.M. Ghiaasiaan, S.I. Abdel-Khalik, and D.L. Sadowski, *Gas-liquid two-phase flow in microchannels: Part I: two-phase flow patterns*, Int J Multiphase Flow **25** (1999), 377–394. [ix, 2, 51, 52]

[53] G. Tryggvason, B. Bunner, O. Ebrat, and W. Tauber, *Computations of multiphase flows by a finite difference/front tracking method. I. Multi–fluid flows*, Von Karman Institute Lecture Notes, Von Karman Institute, Brussels, Belgium, 1998. [14]

[54] S.O. Unverdi and G. Tryggvason, *A front–tracking method for viscous, incompressible, multi–fluid flows*, J Comp Physics **100** (1991), 25–37. [5]

[55] S.O. Unverdi and G. Tryggvason, *Computations of multi-fluid flows*, Physica D **60** (1992), 70–83. [5]

[56] P. Woehl and R.L. Cerro, *Pressure drop in monolith reactors*, Catalysis Today **69** (2001), 171–174. [2]

[57] M.G. Wohak, *Numerische Simulation des Verdampfungsvorgangs eines aufsteigenden Tropfens im Direkt–Kontakt mit einer heißeren, schwereren und nicht mischbaren Flüssigkeit*, Ph.D. thesis, Technische Hochschule Darmstadt, 1996. [2]

[58] M.G. Wohak and H. Beer, *Numerical simulation of direct–contact evaporation of a drop rising in a hot, less volatile immiscible liquid of higher density – posibilities and limits of the sola–vof/csf algorithm*, Numerical Heat Transfer, A **33** (1998), 561–582. [2]

[59] M. Wörner, *The influence of gas-liquid density ratio on shape and rise velocity of an ellipsoidal bubble: a numerical study by 3D Volume-of-Fluid computations*, 1^{st} International Berlin Workshop - IBW1 on Transport Phenomena with Moving Boundaries (Berlin, Germany), $11^{th} - 12^{th}$ October 2001, pp. 67–84. [61, 95]

[60] M. Wörner, W. Sabisch, G. Grötzbach, and D.G. Cacuci, *Volume-averaged conservation equations for volume-of-fluid interface tracking*, New-Orleans, Louisiana, U.S.A., 27^{th} May - 1^{st} June 2001, paper 245. [5, 12, 17]

[61] Z.Y. Zhong, J.R. Lloyd, and K.T. Yang, *Variable-property natural convection in tilted square cavities*, Numerical methods in thermal problems (J.A. Johnson R.W. Lewis and W.R. Smith, eds.), vol. III, Pineridge Press, 1983, pp. 968–979. [48, 49]

[62] Z.Y. Zhong, K.T. Yang, and J.R. Lloyd, *Variable property effects in laminar natural convection in a square enclosure*, J Heat Transfer **107** (1985), 133–138. [48, 49]

APPENDIX

A. COMPARISON BETWEEN CENTRAL DIFFERENCES AND WENO-BASED INTEGRATION ALGORITHMS

In the computer code `TURBIT-VoF` the convection term in the momentum equation can be approximated either using a second order central differences scheme or a WENO (Weighted Essentially Non-Oscillatory) scheme (see Sabisch [38]). Since the WENO algorithm is designed for problems with picewise smooth solutions containing discontinuities, it has been assumed that using this procedure will reduce the velocity and pressure oscillations in the vicinity of the interface. Using a third order WENO scheme, Sabisch [38] simulated the flow of a bubble in a quiescent liquid for various bubble shape regimes. Wörner [59] successfully performed simulations, for the same type of problem, using central differences to approximate the convective terms. The later simulations were done without any other modifications for the `TURBIT-VoF` code which indicates that there might not be any clear benefit in using the more complicated WENO algorithm.

In this chapter, comparative tests, for the same problem, using central differences and WENO approximations are performed. First, we compare the velocity and the momentum fields computed using both schemes for the advection with constant speed of a discontinuous density field. Then, the bubble shapes and positions are compared for the case of a bubble rising in a quiescent liquid.

For both tests the WENO scheme in `TURBIT-VoF` has been modified in order to have a conservative formulation of the convective term. This new algorithm (FV-WENO) is based on a finite volume formulation in contrast with the original version which was based on finite differences approximation (FD-WENO) [38].

A.1 Finite Volume-based WENO scheme

If $(i+1/2, j, k)$ is a numerical cell in which the momentum equation (2.36b) in x-direction has to be numerically integrated, for a finite volume formulation, the convective term is

computed as the sum of the fluxes through the cell faces:

$$[\nabla \cdot \langle \rho u \vec{\mathsf{v}} \rangle]_{i+\frac{1}{2},j,k} = \sum_{\ell} \frac{S_\ell}{V_{i+\frac{1}{2},j,k}} \frac{1}{S_\ell} \int\limits_{S_\ell} \rho u \vec{\mathsf{v}} \cdot \vec{\mathsf{n}}_\ell \, dS \, , \tag{A.1}$$

where $V_{i+\frac{1}{2},j,k}$ is the cell volume, S_ℓ are the faces of the cell and $\vec{\mathsf{n}}_\ell$ is the face normal vector pointing outside the cell. These fluxes which are defined over a surface have to be computed using the volume (cell) averaged values of the velocity. A WENO method implies that one has to use a reconstruction procedure to find point values for the velocity, which are further used to approximate the flux by a q-point Gaussian integration formula. A fully 3D reconstruction algorithm of third order of precision, or higher, requires a large amount of data to be stored and can not be implemented in an efficient way [45]. If only a second order of precision is required (which is acceptable for most of the practical situation we are interested in) a simpler way to compute the surface integrals can be derived. Using Taylor series development the flux through the face ℓ can be approximated as:

$$\mathcal{F}_\ell = \frac{1}{S_\ell} \int\limits_{S_\ell} (\rho u) v_\ell \, dS = (\rho u)(x_\ell, y_\ell, z_\ell) v_\ell(x_\ell, y_\ell, z_\ell) + \mathcal{O}(\Delta^2) \tag{A.2}$$

where, (x_ℓ, y_ℓ, z_ℓ) is the center of the face S_ℓ, $v_\ell = \vec{\mathsf{v}} \cdot \vec{\mathsf{n}}_\ell$ and Δ is the maximum value of the cell length.

The momentum surface-average

$$\varphi_\ell = \frac{1}{S_\ell} \int_{S_\ell} (\rho u) \, dS$$

approximates $(\rho u)(x_\ell, y_\ell, z_\ell)$ up to second order of precision and can be obtained, from the volume-averaged value $[\langle \rho u \rangle]_{i+\frac{1}{2},j,k}$, using a 1D WENO reconstruction of the third order in the direction perpendicular to the face S_ℓ. By this procedure two values $\varphi_\ell^{\pm}$ are obtained corresponding to the right and left side reconstructions. Both these values are used when the flux is computed.

For $v_\ell(x_\ell, y_\ell, z_\ell)$ we can not use the WENO reconstruction. The reason is that each velocity component (and its volume-averaged value) is computed for a different staggered volume and reconstruction procedure is valid only for points inside the volume where the averaged value is defined. To make it more clear, let us take a 2D case (see Fig. A.1):

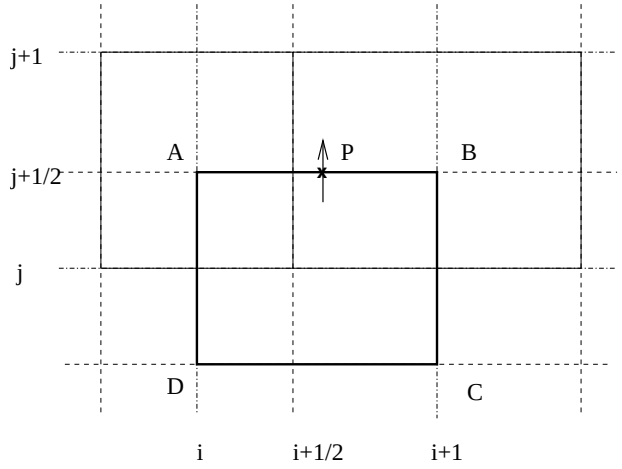

Fig. A.1: 2D view of the computational grid and staggered cell $(i + 1/2, j, k)$ for which the x-velocity component is computed.

the convective term has to be computed for the staggered cell $(i + 1/2, j)$ $(ABCD)$ and the averaged values of the velocity components u and v are defined over $(i + 1/2, j)$ and $(i, j + 1/2)$, respectively. Thus, for the face (AB), the value of velocity component in y-direction (v) has to be computed in the point P. Using a WENO reconstruction one can get only $\frac{1}{\Delta y}\int_{y_j}^{y_{j+1}} v\, dy$. However, this value does not approximate v_P up to second order of precision if P is not the middle of the segment $[y_j, y_{j+1}]$. Also, if the grid is equidistant in x direction we have two distinct values for the reconstructed "surface"-average: one from the left side reconstruction and one from the right side. Contrary to the case for φ there is no suitable criteria to choose between these two values. Thus, in general, for v_ℓ an other approximation has to be used. The simplest way is to compute v_ℓ as the mean value from the neighboring cells values. For the 2D example above this means

$$v_P = \frac{v_{i,j+1/2} + v_{i+1,j+1/2}}{2}. \tag{A.3}$$

This approximation has the advantage that if the velocity field used for the reconstruction is solenoidal, the divergence-free condition will also be valid for the advection field v_ℓ.

As we have mentioned earlier the WENO reconstruction gives two momentum values at each cell face. Thus, the numerical flux $\hat{\mathcal{F}}_\ell$ is defined by

$$\hat{\mathcal{F}}_\ell = h(\varphi_\ell^-, \varphi_\ell^+) \tag{A.4}$$

with the values $\varphi_\ell^{\pm}$ obtained by the WENO procedure. The two argument function h is a monotone flux. It satisfies:

- $h(a,b)$ is a Lipschitz continuous function in both arguments;
- $h(a,b)$ is a nondecreasing function in a and a non-increasing function in b;
- $h(a,b)$ is consistent with the physical flux f, that is $h(a,a) = f(a)$.

Further on we give some examples of monotone fluxes taken from [45]. They were introduced for the case of hyperbolic equations. For Finite Volume method Shu [45] proposes:

1. **Godunov** flux:
$$h(a,b) = \begin{cases} \min\limits_{a\le u\le b} \mathcal{F}(u) & \text{if } a \le b, \\ \max\limits_{b\le u\le a} \mathcal{F}(u) & \text{if } a > b \end{cases} \tag{A.5a}$$

2. **Engquist-Osher** flux:
$$h(a,b) = \int_0^a max(\mathcal{F}'(u),0)\,du + \int_0^b min(\mathcal{F}'(u),0)\,du + \mathcal{F}(0) \tag{A.5b}$$

3. **Lax-Friederichs** flux:
$$h(a,b) = \frac{1}{2}\left[\mathcal{F}(a) + \mathcal{F}(b) - \alpha(b-a)\right] \tag{A.5c}$$
where, $\alpha = \max\limits_{\varphi} |\mathcal{F}'(\varphi)|$ is a constant. The maximum is taken over the relevant range of φ.

For the Finite Difference Shu is also proposing the **Roe-type** flux. In order to use this flux one has to compute the **Roe speed**:
$$\bar{a}_{i+1} = \frac{\mathcal{F}(\varphi_{i+3/2}) - \mathcal{F}(\varphi_{i+1/2})}{\varphi_{i+3/2} - \varphi_{i+1/2}} \tag{A.5d}$$

If the Roe speed is positive the flux is computed using the down-wind cell $(i+1/2)$ otherwise the up-wind cell is used $(i+3/2)$.

For incompressible flow all the above fluxes are equivalent. For reasons related to the simplicity of programming we choose the Roe flux to compute f.

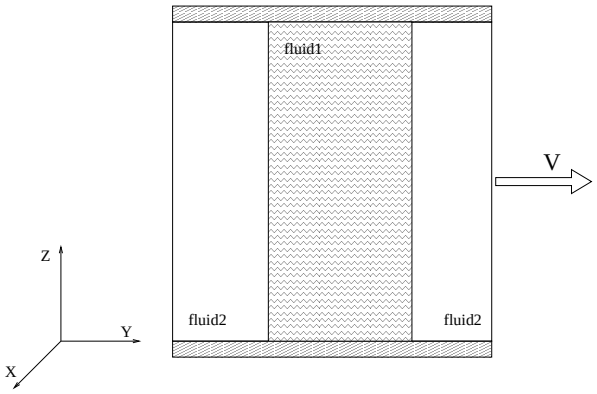

Fig. A.2: Test problem geometry

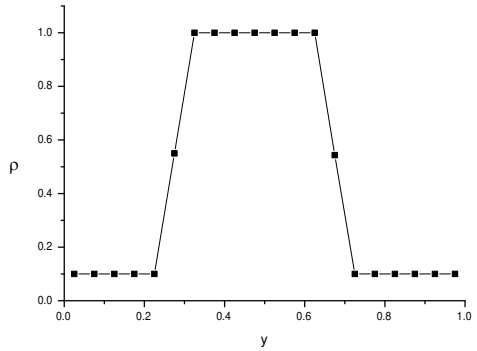

Fig. A.3: Density profile in y-direction at time $t = 0$

A.2 Advection of a discontinuous density field

Let us consider two immiscible fluids having a density ratio $\Gamma_\rho = \rho_1/\rho_2 = 10$ separated by two interfaces. Both fluids are moving with a constant speed ($v = 1$) in y -direction (see Fig. A.2). The computational domain is a cube $1 \times 1 \times 1$ bordered by two solid walls ($z = 0$ and $z = 1$). In the other two directions periodic boundary conditions are used. This domain is discretized in $20 \times 20 \times 20$ computational cells. For our tests we set the viscosity to zero ($\nu_1 = \nu_2 = 0$). The initial density profile in the middle of the channel is presented in Fig. (A.3)

In order to see how well the modified WENO scheme behaves we look at the velocity and momentum profile in y-direction after one advection time step, i.e. after a complete Runge-Kutta time integration. We use for comparison the results obtained using a second order central difference scheme to approximate the convective terms.

In Fig. A.4 we present the momentum (Fig. A.4(a)) and the velocity (Fig. A.4(b)) profiles in the middle of the channel ($z = 0.5$) for an integration time step $\Delta t = 0.1 \cdot \Delta t_{CFL}$. For the momentum the results are similar for all three methods. The WENO methods, however, give a smaller value for the fluid 1 momentum at the backside interface ($y = 0.35$) and a higher value for the fluid 2 momentum at the front-side interface ($y = 0.75$) than central differences (CD) scheme. This results in a smaller, respectively a higher value of the velocity in this two regions. Looking at the velocity profiles we could say that the WENO method behaves in the same way as the central differences scheme but has a smaller numerical viscosity.

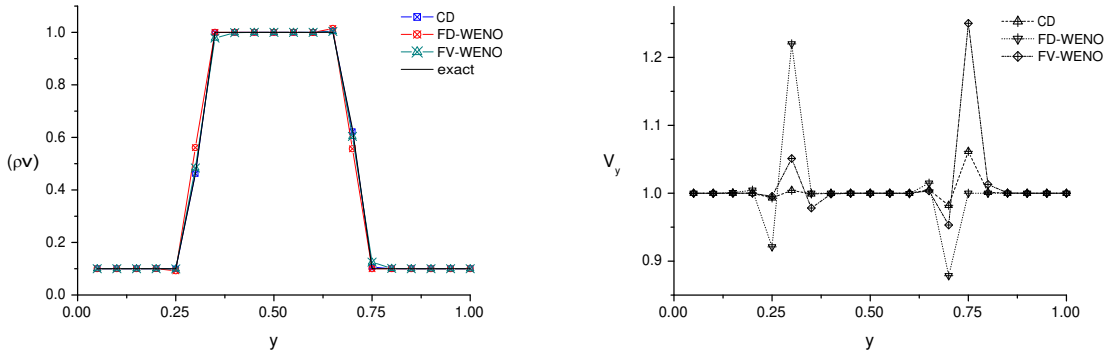

(a) Momentum profile

(b) Velocity profile

Fig. A.4: Momentum and velocity profiles in y direction for a time step $\Delta t = 10^{-3} (= 0.1 \Delta t_{CFL})$. The "exact" profile was computed as ρv, where ρ is the advected density profile.

A.3 Bubble rising in a quiescent liquid

In the previous test the viscous terms have been neglected in order to analyze the influence of convective terms approximation on the velocity field. To see how the two algorithms, CD and FV-WENO, behave in case of a two-phase flow we simulate the rise of a bubble in a quiescent liquid. The computational domain is bordered in z-direction by two walls while the flow is periodic in other two directions. The periodicity conditions imply that rows of bubbles are simulated. To minimize the interaction between two consecutive bubbles the domain is two times longer, in stream-wise direction, than wide $(1 \times 2 \times 1)$. An uniform grid $(64 \times 128 \times 64)$ is used to discretize the domain. In both cases the bubble starts from rest. Initially, it is spherical with a diameter 1/4 from the channel width and its center is at $\vec{\mathtt{x}} = (0.5, 0.5, 0.5)$.

For this test we consider the case when final bubble shape is a dimple ellipsoidal cap. The bubble Reynolds number is $\mathtt{Re} = 20$ and the Etvös number is $\mathtt{Eo} = 2000$. The liquid density and viscosity are 80 times larger than those for the gas. In Figure A.5 the bubble shapes and positions after $t = 0.5$ are compared. For the central differences method the left half of the bubble (in blue) is shown while for the FV-WENO scheme the right half is presented on the same picture. Since the interface reconstruction depends on the size of the mesh cell (represented in Fig. A.5(b) by a small square) one can conclude that both numerical algorithms, CD and FV-WENO, give the same result.

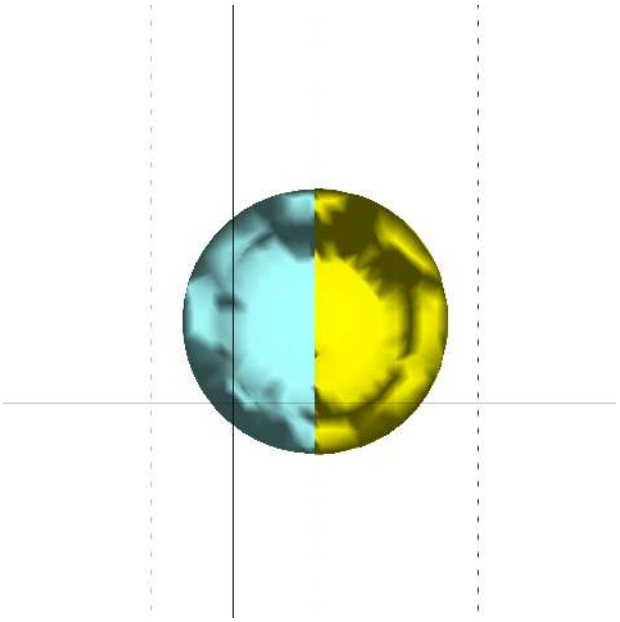

(a)

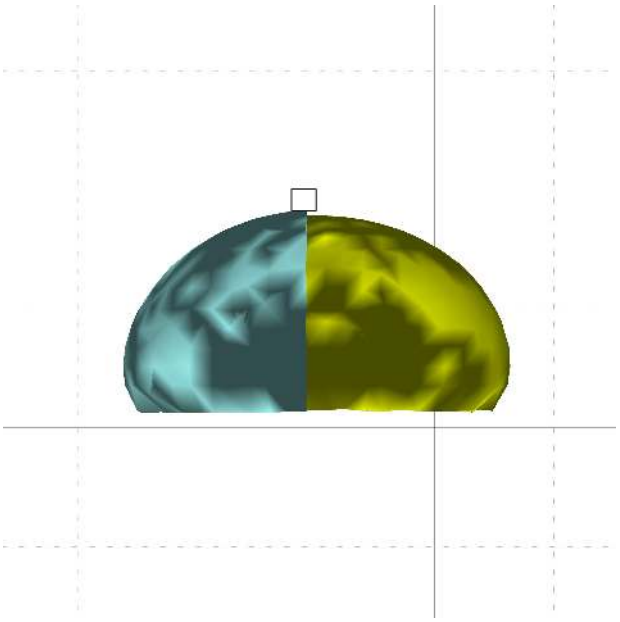

(b)

Fig. A.5: Bubble shape and position comparison between central differences (left half; blue) and FV-WENO (right half; yellow) schemes: (a) bottom view; (b) side view (the size of the mesh cell is indicated by the small square);.

B. CONVECTIVE TERMS APPROXIMATION FOR A TWO-PHASE SYSTEM

When volume fractions are used to approximate the density in the convective terms oscillations of the solution appear near the interface. To illustrate this phenomena and to identify its source, let us consider the simple case of a two-phase system ($\rho_1/\rho_2 = 2$) moving with a constant velocity ($U = 1$) in direction perpendicular to the interface. Assuming that there are no heat sources when the thermal equilibrium is achieved the temperature is constant and has the same value in both fluids ($T = 1$). The advection equation for the enthalpy is then:

$$\frac{\partial}{\partial t}\langle \rho C_p T \rangle + \frac{\partial}{\partial x}\langle \rho C_p T U \rangle = 0 \tag{B.1}$$

For simplicity one can take the liquid density $\rho_1 = 1$ and the same specific heat for both gas and liquid $C_{p,1} = C_{p,2} = 1$. The initial configuration is considered so that all the computational cells up to $x_{i-\frac{1}{2}}$ (see Fig. B.1) are filled with liquid (ρ_1) and the rest of them are filled with gas (ρ_2). After $\Delta t = 0.25$ the interface has moved in the stream-wise direction but the temperature field remains unchanged, i.e. $T = 1$.

The numerical approximation of (B.1) using the centered difference scheme(3.10) for

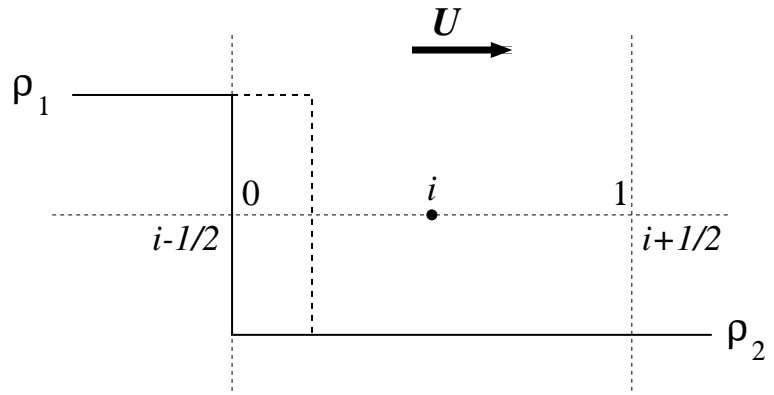

Fig. B.1: Initial configuration (thick solid line) and after $\Delta t = 0.25$ (thick dashed line)

the convective term and an Euler time evolution scheme is

$$[f_i^{(n+1)}\rho_1 C_{p,1} + (1-f_i^{(n+1)})\rho_2 C_{p,2}]T_i^{(n+1)} = [f_i^{(n)}\rho_1 C_{p,1} + (1-f_i^{(n)})\rho_2 C_{p,2}]T_i^{(n)} - \frac{\Delta t}{\Delta x}\left[(f_{i+\frac{1}{2}}^{(n)}\rho_1 C_{p,1} + (1-f_{i+\frac{1}{2}}^{(n)})\rho_2 C_{p,2})\frac{T_i^{(n)}+T_{i+1}^{(n)}}{2} - (f_{i-\frac{1}{2}}^{(n)}\rho_1 C_{p,1} + (1-f_{i-\frac{1}{2}}^{(n)})\rho_2 C_{p,2})\frac{T_i^{(n)}+T_{i-1}^{(n)}}{2}\right] \quad \text{(B.2)}$$

where, f_i is the liquid volume fraction corresponding to the centered cell and $f_{i\pm\frac{1}{2}}$ are the staggered liquid fractions at the faces of the cell. If the volume fractions of the staggered cells $(i \pm \frac{1}{2})$ are used to approximate $f_{i\pm\frac{1}{2}}$, which means that $f_{i-\frac{1}{2}}^{(n+1)} = 0.75$ and $f_{i+\frac{1}{2}}^{(n+1)} = 0$, the computed temperature of the cell (i) at the new time step is

$$\begin{aligned} T_i^{(n+1)} &= \frac{(0+1\times 0.5)\times 1 - 0.25\times(0.5\times 1 - (0.75+0.25\times 0.5)\times 1)}{0.25+0.75\times 0.5} \\ &= 0.95 \end{aligned}$$

If a Runge-Kuta time integration scheme is used, a better approximation of $T_i^{(n+1)}$ is obtained but the value still differs from the exact solution. On the other hand, using the upwind procedure (3.13) described in section 3.1.1 to select the staggered surface fractions ($f_{i-\frac{1}{2}} = 1$, $f_{i+\frac{1}{2}} = 0$) the computed temperature for the new time step is

$$T_i^{(n+1)} = 1$$

Similar results are obtained if the velocity sign is changed or the initial position of the interface is modified.

This simple one-dimensional example shows that, for the convective term, when discontinuities are present an upwind procedure should be used at least for the surface fractions at the cell faces if an centered difference approximation is required for the temperature.